

**Characterization of the Performance of PEM Water Electrolysis
Cells operating with and without Flow Channels, based on
Experimentally Validated Semi-empirical Coupled-Physics
Models**

Von der Fakultät für Maschinenbau, Elektro- und Energiesysteme der Brandenburgischen
Technischen Universität Cottbus – Senftenberg zur Erlangung des akademischen Grades
eines Doktors der Ingenieurwissenschaften (Dr.-Ing.)

genehmigte Dissertation

Vorgelegt von

M.Sc. Emile Tabu Ojong

geboren am 06.12.1976 in Kumba - Kamerun

Vorsitzender: Prof. Dr.-Ing. Georg Möhlenkamp

Gutachter: Prof. Dr.-Ing. Hans Joachim Krautz

Gutachter: Prof. Dr.-Ing. Heinz Peter Berg

Tag der mündlichen Prüfung: 25.10.2018

Declaration

I, Emile Tabu Ojong hereby declare, that I am the sole author and composer of this Thesis and that it is herein presented in its original form. No other sources or learning aid other than those cited have been used. I also declare that, this Thesis has not been prepared or submitted for any other examination or assignment, either in whole or in parts.

Place, date

Signature

Acknowledgements

This work is dedicated to my beloved wife, B.Sc.-Eng. Susan Ojong and to my wonderful kids; MaAyuk Ojong and MaEtuk Ojong. You all are my “joie de vivre” and inspiration!

My utmost gratitude goes first and foremost to my parents for their continuous and steadfast support in all my undertakings. Big thanks goes also to all my family, especially to the most loving elder sister in the world that I have been blessed to have.

This work would not have been successful without the constant and unreserved support from my colleagues at the Department of Chemical Energy Storage at the Fraunhofer Institute of Solar Energy Systems in Freiburg. I doff my hat and say thank you to you all. Most especially, thanks to Dr. Christopher Hebling and Dr. Tom Smolinka for giving me the chance to achieve this milestone. Tom, I can never be thankful enough for the wonderful guidance and support (both professionally and personally) that I was privileged to have over the years working with you. You counted on me against all odds, and, this is for you – THANK YOU TOM!!

Finally, I want to say thank you to Professor Krautz for not only being the academic supervisor of this Thesis, but also for taking time away from his busy schedule on several occasions to discuss about my work. Thank you also, Dr. Ulrich Fischer for the academic supervision and for proof reading this Thesis.

Preview

PEM water electrolysis is a clean and efficient conversion technology for hydrogen production and energy storage, especially when coupled with renewable energy sources. In spite of its many advantages, the high component and cell manufacturing costs of the conventional PEM electrolysis cell makes the PEM water electrolysis technology commercially less competitive vis-à-vis its peers. An alternative and cost effective cell design has been proposed which has up to a 25 % costs advantage over the conventional cell. In this alternative cell design, the flow channel plate which bears the most material costs in the conventional cell design has been replaced with a 3-D Porous Transport Layer (PTL) structure. While both designs perform comparably the same at low to mid current density ($0 - 2 \text{ A/cm}^2$), it has been observed that the conventional cell by far out performs the low cost cell at high current density operations, due to increased mass transport limitation in the cell without flow channels. Since industrial and commercial hydrogen production efforts are focused towards high current density operation ($> 3 \text{ A/cm}^2$), it thus becomes obvious that, in order for the cost effective alternative cell design to establish itself over the conventional cell design, the mass transport issues at high current densities have to be well understood and described.

This research work seeks to understand the source of, and to eliminate the mass transport losses in the cost effective alternative cell design in order to get it performing at least as good as the conventional cell design at current densities up to 5 A/cm^2 . To meet this objective, 2-D non-isothermal semi-empirical fully-coupled models of both cell designs have been developed and experimentally validated. The developed validated models were then used as tools to simulate and predict the best operating conditions, design parameters and micro-structural properties of

the PTL at which the mass transport issues in the design without flow channels will be at its minimum, so that both cells can exhibit comparable performance even at high current densities.

The models developed in this work are based on a multi-physics approach in which thermodynamic, electrochemical, thermal and mass transport sub-models are coupled and solved numerically, to predict the cell polarization and individual overpotentials, as well as address heat and water management issues. The most unique aspect of this work however, is the development of own semi-empirical equations for predicting the mass transport overpotential imposed by the gas phase (bubbles) at high current densities. Also, for the very first time, calculated PEM water electrolysis polarization curves up to 5 A/cm² have been validated by own experimental data.

The results show that, the operating temperature and pressure, inlet water flowrate and thickness of the PTL are the critical parameters for mitigating mass transport limitation at high current densities. In fact, it was found that, for the size of the cells studied (25 cm² active area each), when both cells are operating at the same temperature of 60 °C, the low cost cell design will have a comparable performance to the conventional designed cell even at 5 A/cm² current density when; the operating pressure is ≥ 5 bar, the feed water flowrate is $\geq 0.024 \text{ l/min} \cdot \text{cm}^2$, PTL porosity is 50 %, PTL pore size is $\geq 11 \text{ }\mu\text{m}$ and PTL thickness is 0.5 mm. At these operating, design and micro-structural conditions, the predicted difference between the polarizations of both cells will be only ~ 10 mV at 5 A/cm² operating current density.

Keywords: PEM Electrolysis; Porous Transport Layer; Mass Transport; Modelling; Experimental Validation.

Zusammenfassung

Die PEM Wasser Elektrolyse gilt als effiziente Technologie zur Herstellung von sauberem Wasserstoff zur Energiespeicherung, besonders bei Kopplung mit erneuerbaren Energien. Trotz der vielen Vorteile führen hohe Kosten für die Produktion konventioneller Komponenten und Stacks zu einer nicht konkurrenzfähigen Technologie. Ein alternatives und kostengünstiges Zelldesign wurde vorgestellt, das, verglichen mit einem konventionellen Design, einen Kostenvorteil von bis zu 25 % hervorbringt. Bei diesem alternativen Zelldesign wird die Platte mit Strömungskanälen, die den größten Kostenanteil birgt, durch eine 3-D poröse Struktur (engl. Porous transport layer, PTL) ersetzt. Während beide Designs vergleichbare Leistungsdaten im niederen und mittleren Stromdichtebereich zeigen (0 – 2 A/cm²), wurde ein signifikanter Unterschied im hohen Stromdichtebereich beobachtet. Hierbei zeigt ein Design ohne Strömungskanäle niedrigere Leistungsdaten, was durch eine gesteigerte Limitierung des Massentransportes erklärt werden kann. Da sich die industrielle und kommerzielle Wasserstoffproduktion in Richtung hoher Stromdichten (> 3 A/cm²) entwickelt, scheint das erforderliche Verständnis von Massentransporteffekten offensichtlich um das kosteneffiziente Design gegenüber des konventionellen Designs voran zu treiben. Diese Forschungsarbeit versucht den Ursprung von Massentransportlimitierung des kostengünstigen Zelldesigns zu verstehen und eliminieren, um zumindest entsprechende Leistungsdaten des konventionellen Designs bis 5 A/cm² zu erreichen. Um diese Zielvorgabe zu erreichen, wurden 2-D nicht-isotherme, semi-empirische, vollständig gekoppelte Modelle beider Zelldesigns entwickelt und experimentell validiert. Die entwickelten und validierten Modelle wurden als Werkzeug zur Simulation und Vorhersage der geeignetsten Betriebs- und Designparameter, sowie Eigenschaften der Mikrostruktur der PTL verwendet. Dabei sind die Verluste durch Massentransport, im Design ohne Strömungskanäle, minimal, sodass beide Designs

vergleichbare Leistungsdaten bei hohen Stromdichten zeigen. Die hierin entwickelten Modelle basieren auf einem multiphysikalischen Ansatz, worin thermodynamische, elektrische und thermische Effekte sowie Massentransportuntermodelle gekoppelt und gelöst wurden, um sowohl die Zellpolarisation und individuelle Überpotentiale vorherzusagen, als auch Wärme- und Wassermanagement zu adressieren. Das Alleinstellungsmerkmal dieser Arbeit ist jedoch die Entwicklung von semi-empirischen Gleichungen, um die Überpotentiale der Massentransporthemmung, ausgehend von Gasblasen, vorhersagen zu können. Ebenso wurden zum ersten Mal berechnete PEM Wasser Elektrolyse Polarisationskurven bis zu einer Stromdichte von 5 A/cm^2 mit eigenen Daten validiert. Die Ergebnisse zeigen, dass Betriebstemperatur und Druck, sowie Wasserflußrate am Zelleingang und Dicke der PTL die kritischen Parameter sind, um Massentransportlimitierung bei hohen Stromdichten zu vermeiden. Es wurde sogar gezeigt, dass bei der verwendeten Zellgröße (aktive Fläche = 25 cm^2) vergleichbare Leistungsdaten bei 60 °C und 5 A/cm^2 erreicht werden können, sofern der Betriebsdruck 5 bar übersteigt, die Flussrate des Eduktwassers größer als 0.024 l/min ist, die Porosität der PTL 50% übersteigt, die Porendurchmesser größer als $11 \text{ }\mu\text{m}$ sind und die PTL Dicke bei 0.5 mm liegt. Bei diesen Betriebsbedingungen, diesen Design- und Mikrostrukturparametern wurden Unterschiede zwischen den beiden Zelldesigns von etwa 10 mV bei 5 A/cm^2 vorhergesagt.

Stichwörter: PEM-Elektrolyse; Poröse Transportschicht; Massentransport; Modellierung; Experimentelle Validierung.

Publications

Reviewed Articles

1. **Development of an Experimentally Validated Semi-empirical Fully-Coupled Performance Model of a PEM Electrolysis Cell with a 3-D-structured Porous Transport Layer**

International Journal of Hydrogen Energy vol. 42, Issue 41 (2017) pp. 25831 – 25847.

DOI: 10.1016/j.ijhydene.2017.08.183

E. T. Ojong, J. H. T. Kwan, A. K. Nouri, A. Bonakdarpour, D. P. Wilkinson, T. Smolinka

2. **Model of Oxygen Bubbles and Performance Impact in the Porous Transport Layer of PEM Water Electrolysis Cells**

International Journal of Hydrogen Energy vol. 42, Issue 48 (2017) pp. 28653–29066.

DOI: 10.1016/j.ijhydene.2017.09.167

A. K. Nouri, E. T. Ojong, T. Smolinka, D. P. Wilkinson

3. **Fundamentals of PEM Water Electrolysis**

In: D. Bessarabov, H. Wang, H. Li, N. Zhao (Eds.), *PEM Electrolysis for Hydrogen Production. Principles and Applications*, Taylor & Francis Group, Boca Raton, USA, 2016, pp. 11 – 35

T. Smolinka, E. T. Ojong, T. Lickert

4. **Hydrogen Production from Renewable Energies – Electrolyzer Technology**

In: P. T. Moseley, J. Garche (Eds.), *Electrochemical Energy Storage for Renewable Sources and Grid Balancing*. Elsevier 2015, pp. 103 – 128

T. Smolinka, E. T. Ojong, J. Garche

Conference oral presentations

1. **Design, Construction and Performance of PEM Electrolysis Stack Operating at High Pressures**

In, *5th International conference on “Fundamentals and Development of Fuel Cells”*.

April 16. – 18. 2013, Karlsruhe, Germany

E. T. Ojong, E. Mayousse, N. Guillet, D. Vannucci, F. Beille, T. Smolinka

2. **Model Assisted Design and Performance of Polymer Electrolyte Membrane Electrolyser Operating at High Pressures**

In, *Hydrogen + Fuel Cells 2013*. June 16 – 19 2013, Vancouver, Canada

E. T. Ojong, E. Mayousse, N. Guillet, D. Vannucci, F. Beille, T. Smolinka

3. **Advanced Bipolar Plates without Flow Channels for PEM Electrolysers Operating at High Pressures**

In, *Technoport RERC Research*. April 16. – 18. 2012, Trondheim, Norway

E. T. Ojong, E. Mayousse, N. Guillet, D. Vannucci, F. Beille, T. Smolinka

Abbreviations

AEL	Alkaline electrolysis
APS	Average pore size
ASR	Area specific resistance
ASTM	American Society for Testing and Materials
BIP	Bipolar plate
BoP	Balance of plant
BP	Bubble point
DC	Direct current
FCEV	Fuel cell electrical vehicles
FEA	Finite element analysis
GEC	General Electric Company
GES	Giner Electrochemical Systems
HER	Hydrogen evolution reaction
HHV	Higher heating value
ICR	Interfacial contact resistance
LHV	Lower heating value
MEA	Membrane electrode assembly
NASA	U.S National Aeronautics and Space Administration
OCV	Open cell voltage
OER	Oxygen evolution reaction
PBR	Pore-to-bubble ratio
PEM	Polymer Electrolyte Membrane
PES	Proton Energy Systems
PFSA	Perflourosulfonic acid
PTL	Porous transport layer
RDE	Rotating disc electrode
RES	Renewable energy sources
RPM	Rotations per minute
SHE	Standard hydrogen electrode
SOEC	Solid oxide electrolysis cell
SP	Smallest pore

SPE	Solid polymer electrolyte
US DOE	United States Department of Energy
YSZ	Yttria stabilised zirconia

Symbols

Character	Units	Description
E_a	kJ mol^{-1}	Activation energy
D_B	$\text{Pa m}^2 \text{s}^{-1}$	Binary diffusion coefficient
d_{bubble}	M	Bubble diameter
T	K, °C	Cell temperature
V_{cell}	V	Cell voltage
j	A cm^{-2}	Current density
D	$\text{m}^2 \text{s}^{-1}$	Diffusion coefficient
\bar{u}	M	Displacement (deformation)
J	A	Electrical current
S_{eff}	-	Electrochemical specific surface
j_o	A cm^{-2}	Exchange current density
\dot{Q}_{el}	W m^{-2}	Exothermal heat production
F	C mol^{-1}	Faraday constant
K_{Henry}	atm mol^{-1}	Henry's solubility constant
F_I	N	Inertia forces
L	M	Length of cell
j_{lim}	A cm^{-2}	Limiting current density
D_{stiff}	N m^{-1}	Material stiffness
d_{mem}	M	Membrane thickness
ΔS	$\text{kJ K}^{-1} \text{mol}^{-1}$	Molar change in entropy
ΔG	kJ mol^{-1}	Molar change in Gibbs free energy
C	mol m^{-3}	Molar concentration
v	$\text{s mol}^{-1} \text{m}^{-3}$	Molar diffusion volume
ΔH	kJ mol^{-1}	Molar enthalpy change
\dot{N}	mol s^{-1}	Molar flowrate

M	g mol^{-1}	Molecular mass
n	-	Number of electrons involved in the electrochemical reaction
R_{ohm}	Ω	Ohmic resistance
p_0	Bar	Operating pressure
T_0	K, °C	Operating temperature
U	$\text{m}^3 \text{s}^{-1}$	Operating water flowrate
$w_{active\ area}$	M	Out of plane width of the active area
r	-	Poisson ratio
d_{pore}	M	Pore diameter
r_{pb}	-	Pore to bubble ratio
p	Bar	Pressure
d_{PTL}	M	PTL thickness
k	$\text{L mol}^{-1} \text{s}^{-1}$	Reaction rate constant
\dot{R}_i	$\text{mol m}^{-3} \text{s}^{-1}$	Reaction term
E_{rev}	V	Reversible cell voltage
C_p	$\text{J kg}^{-1} \text{K}^{-1}$	Specific heat capacity
A	m^2	Surface area
K	$\text{W m}^{-1} \text{K}^{-1}$	Thermal conductivity
E_{th}	V	Thermo-neutral voltage
R	$\text{kJ mol}^{-1} \text{K}^{-1}$	Universal gas constant
u_{FC}	m s^{-1}	Velocity of water in the flow channel
u	m s^{-1}	Velocity of water in the porous media
\dot{V}	$\text{m}^3 \text{s}^{-1}$	Volumetric flowrate
\dot{Q}_{h2o}	$\text{kg m}^{-2} \text{s}^{-1}$	Water source term
Y	kg m s^{-2}	Young's modulus

Greek Symbols

Character	Unit	Description
θ	-	Bubbles coverage
ρ	kg m ⁻³	Density
σ	S m ⁻¹	Electrical conductivity of
α	-	Electrochemical charge transfer coefficient
δ	-	Electro-osmotic drag coefficient
λ	-	Membrane humidification
φ	V	Membrane potential
Ω	-	Model boundary
η	V	Overpotential
ε	-	Porosity
σ_{mem}	S m ⁻¹	Proton conductivity of PEM
γ	Pa m	Surface tension
ζ	-	Water starvation ratio
β	(°)	Wetting angle

Subscripts and superscripts

<i>act</i>	Activation
<i>an</i>	Anode
<i>aq</i>	Aqueous
Cap	Capillary
<i>cat</i>	Cathode
<i>diff</i>	Diffusion
<i>eff</i>	Effective
<i>elect</i>	Electrical
<i>FC</i>	Flow channel
1, 2	Forward and backward reactions, respectively
<i>g</i>	Gas phase
0	Initial condition (as subscript)

<i>in</i>	Inlet
<i>l</i>	Liquid phase
<i>mass trans</i>	Mass transport
<i>mem</i>	Membrane
<i>ohm</i>	Ohmic
<i>pdt</i>	Products
<i>rct</i>	Reactants
<i>R</i>	Reaction
<i>ref</i>	Reference state
<i>rev</i>	Reversible
Sat	Saturation
<i>i</i>	Species type
0	Standard conditions (as superscript)
<i>th</i>	Thermo-neutral
<i>Ti</i>	Titanium

Constants and materials properties

Symbol	Value	Unit	Description
$E_{a,an}$	15	kJ mol^{-1}	Activation energy, anode
$E_{a,cat}$	18	kJ mol^{-1}	Activation energy, cathode
α_{an}	0.5	-	Anode charge transfer coefficient
D_B	$3.16 \cdot 10^{-8}$	$\text{Pa m}^2 \text{ s}^{-1}$	Binary diffusion coefficient
α_{cat}	0.5	-	Cathode charge transfer coefficient
ρ_{h2}	0.08988	g L^{-1}	Density of hydrogen
ρ_{o2}	1.429	g L^{-1}	Density of oxygen
ρ_{h2o}	971.6	kg m^{-3}	Density of water
μ_{h2}	$1.09 \cdot 10^{-5}$	Pa s	Dynamic viscosity of hydrogen
μ_{o2}	$2.47 \cdot 10^{-5}$	Pa s	Dynamic viscosity of oxygen
μ_{h2o}	$2.822 \cdot 10^{-2}$	Pa s	Dynamic viscosity of water
σ_{Ti}	18000	S cm^{-1}	Electrical conductivity of titanium
$S_{eff,an}$	100	-	Electrochemical specific surface area, anode

$S_{eff,cat}$	40	-	Electrochemical specific surface area, cathode
F	96485.34	C mol ⁻¹	Faraday constant
$Sol_{h_2;h_2o}$	0.00167	mol mol ⁻¹	Hydrogen solubility in water
L_{FC}	5	cm	Length of flow channels
d_{man}	6	mm	Manifold diameter
ρ_{mem}	2000	kg m ⁻³	Membrane density
λ	24	-	Membrane humidification
K_{mem}	0.85	W m ⁻¹ K ⁻¹	Membrane thermal conductivity
d_{mem}	180	μ m	Membrane thickness
v_{h_2}	$7.07 \cdot 10^{-6}$	s mol ⁻¹ m ³	Molar diffusion volume of hydrogen
v_{o_2}	$16.6 \cdot 10^{-6}$	s mol ⁻¹ m ³	Molar diffusion volume of oxygen
v_{h_2o}	$12.7 \cdot 10^{-6}$	s mol ⁻¹ m ³	Molar diffusion volume of water
M_{h_2}	1.00794	g mol ⁻¹	Molecular mass of hydrogen
M_{o_2}	16	g mol ⁻¹	Molecular mass of oxygen
M_{h_2o}	18.08	g mol ⁻¹	Molecular mass of water
n_{an}	2	-	Number of electrons in reaction, anode
n_{cat}	-2	-	Number of electrons in reaction, cathode
$Sol_{o_2;h_2o}$	0.00185	mol mol ⁻¹	Oxygen solubility in water
ε_{PTL}	0.4	-	PTL porosity
$j_{0,ref,an}$	$5.35 \cdot 10^{-4}$	mA cm ⁻²	Reference exchange current density, anode
$j_{0,ref,cat}$	1	mA cm ⁻²	Reference exchange current density, cathode
$C_{p;h_2}$	14.3	J g ⁻¹ K ⁻¹	Specific heat capacity of hydrogen
$C_{p;mem}$	508	J kg ⁻¹ K ⁻¹	Specific heat capacity of membrane
$C_{p;o_2}$	0.918	J g ⁻¹ K ⁻¹	Specific heat capacity of oxygen
$C_{p;h_2o}$	4.1813	J g ⁻¹ K ⁻¹	Specific heat capacity of water
γ_{h_2o}	0.05884	Pa m	Surface tension of water
d_{ecl}	40	μ m	Thickness of electro-catalyst layer
ρ_{Ti}	4.51	g cm ⁻³	Titanium density
ρ_{Ti}	540	J kg ⁻¹ K ⁻¹	Titanium specific heat capacity
K_{Ti}	16.4	W m ⁻¹ K ⁻¹	Titanium thermal conductivity
R	8.314472	kJ mol ⁻¹ K ⁻¹	Universal gas constant

Contents

Acknowledgements	II
Preview	IV
Zusammenfassung.....	VI
Publications	IX
List of Figures	XXI
List of Tables	XXIV
General Introduction	1
1.1 Renewable energy sources and the hydrogen economy.....	1
1.2 Hydrogen production by water electrolysis	3
1.2.1 Thermodynamics of water electrolysis	5
1.2.2 Reaction kinetics	9
1.2.3 Performance characteristics	16
1.3 Alkaline water electrolysis.....	18
1.4 High temperature water electrolysis.....	18
1.5 PEM water electrolysis	19
1.5.1 Design and components of a conventional PEM electrolysis cell	21
1.5.2 Challenges and trends in PEM water electrolysis	27
Motivation, Objectives and Methods	31
2.1 Main issues and objectives.....	31
2.2 Methodology	36
Literature Review	39
3.1 PEM electrolysis cell and stack development.....	39
3.2 Porous Transport Layers (PTLs).....	40
3.3 In Situ characterization techniques for PEM electrolysis cells	42
3.4 PEM electrolysis modelling.....	45
Model Development	49
4.1 Reversible Cell Voltage and Irreversible Losses	50
4.1.1 Thermodynamic consideration.....	50
4.1.2 Kinetics losses.....	52
4.1.3 Ohmic losses	53
4.1.4 Mass transport losses	55
4.1.5 Polarisation curves generation	59
4.2 Governing equations	60

4.2.1	Current conservation sub-model	60
4.2.2	Momentum transport sub-model	61
4.2.3	Mass transport sub-model	63
4.2.4	Heat transfer sub-model	64
4.3	Numerical methods	65
4.4	Model Assumptions and Limitations	69
Experimental Methods		73
5.1	Ex Situ measurement of material and electro-kinetic properties	73
5.1.1	Determination of the microstructure properties of the PTL	74
5.1.2	Determination of the electro-kinetic parameters of the OER catalyst.....	76
5.2	In Situ measurement of performance curves.....	77
5.2.1	Test cell design and construction	78
5.2.2	Test system and polarization curves measurement	81
5.2.3	Interfacial contact resistance correction.....	83
Results and Discussion.....		86
6.1	Capillary flow porometry measurements.....	86
6.2	Measured polarization curves	88
6.3	Interfacial contact resistance correction.....	89
6.4	Validation of models.....	91
6.5	Effects of the operating parameters.....	98
6.5.1	Cell operating temperature.....	98
6.5.2	Feed water flowrate.....	100
6.5.3	Cell operating pressure.....	104
6.6	Effects of the PTL microstructure.....	107
6.6.1	Porosity of the PTL	107
6.6.2	Mean pore size of the PTL	109
6.7	Effects of design parameters	110
6.7.1	Thickness of the PTL	110
6.7.2	Channel dimensions	113
6.8	Comparison of the performances of both cell designs	117
6.9	Summary of all the reversible and irreversible losses.....	119
6.10	Recommendation for low cost design and high performance cell	122
Summary, conclusion and outlook		126
References.....		132
Appendices.....		143

List of Figures

Figure 1: Basic principle of a water electrolysis cell.....	5
Figure 2: Total energy requirements for water electrolysis as a function of temperature at standard pressure	8
Figure 3: The reversible cell voltage as a function of temperature and pressure	9
Figure 4: Activation energy vs. reaction progress	10
Figure 5: Butler-Volmer dependence of the current density and overpotential.....	13
Figure 6: Schematic of the mass transport mechanisms	15
Figure 7: The regions of a typical polarization curve of a PEM water electrolyser operating at high current densities, including an estimation of the contribution of the main sources of overpotentials and the reversible cell voltage to the cell polarization	17
Figure 8: Basic design principle of a conventional PEM water electrolysis cell.....	22
Figure 9: A conventional bipolar plate with machined flow channels	23
Figure 10: Pressure plates serve as supporting structure for single cell components.....	25
Figure 11: PTL materials commonly employed in PEM water electrolysis.....	27
Figure 12: Design concept of a conventional PEM electrolyser, with machined channels on bipolar plates.....	32
Figure 13: Specific costs breakdown of materials and production costs per stack for both designs.....	32
Figure 14: Design concept of a PEM electrolyser without flow channels on the bipolar plates	33

Figure 15: Experimentally measured polarisation curves comparing the performance of the cell concept with flow channels and that without flow channels.....	35
Figure 16: Research methodology	37
Figure 17: Number of publications as a percentage of total publications directly related to PEM water electrolysis over the years, including those related specifically to PEM electrolysis modelling.	46
Figure 18: Linearized dependency of the entropy component on temperature	51
Figure 19: Bubble distribution and surface shielding in the anode half cell of the design with flow channels	57
Figure 20: Equivalent electrical circuit of PEM water electrolysis cell. Cell voltage as a sum of the reversible cell voltage and all the overpotentials treated as resistors in series	59
Figure 21: Momentum and mass transport inside the cell	61
Figure 22: Model application modes and coupling strategy	65
Figure 23: Model geometry and boundary conditions	67
Figure 24: Mesh distribution on the model geometry, for the design without flow channels ..	69
Figure 25: Schematic of capillary flow porometry characteristics.	75
Figure 26: Cross section of the 3-D construction and assembling of the experimental test cell (Conventional design concept)	78
Figure 27: Cross section of the 3-D construction and assembling of the experimental test cell (design concept without flow channels)	79
Figure 28: A) Surface plot showing maximum deformation of the pressure plate structure design clamping load, for a 20 mm thick plate, B) Surface plot showing maximum von Mises stress distribution	80
Figure 29: Test cell design.....	81

Figure 30: Layout of the test system with anode single feed and balanced pressure on the anode and cathode sides.....	82
Figure 31: Test cell connected to the test rig	83
Figure 32: Porometry results.....	87
Figure 33: Temperature dependent polarization curves as measured with high interfacial contact resistance	89
Figure 34: IR correction of temperature curves for design without channels.....	90
Figure 35: As measured and ICR corrected polarisation curves compared.....	90
Figure 36: Comparison of the measured and predicted polarisation curves	92
Figure 37: Cell temperature distribution in the conventional design.....	93
Figure 38: Cell temperature distribution in the design without flow channels.....	94
Figure 39: Pourbaix diagram of titanium in water at 25 °C.....	95
Figure 40: Comparison of measured and predicted polarisation curves for different water flowrates at 60 °C and 1 bar.....	96
Figure 41: Comparison of measured and predicted polarisation curves for different operating pressured at 60 °C and 0.6 l/min water flowrate for	97
Figure 42: Comparison of the calculated temperature dependent polarisation curves for the conventional and advanced cell design concepts.....	99
Figure 43: Effect of operating temperatures on the bubble coverage and mass transport.....	100
Figure 44: Effects of water flowrate	101
Figure 45: Effects of water flowrate on mass transport losses	102
Figure 46: Effects of water flowrate on the water-to-gas ratio at the active surface and the pore-to-bubble ratio.	103
Figure 47: Effects of operating pressure.....	105
Figure 48: Effects of the operating temperature and pressure on the cell performance	106

Figure 49: Predicted effect of porosity shown for the design without flow channels	108
Figure 50: Effects of the PTL mean pore size	109
Figure 51: The calculated effect of PTL thickness	111
Figure 52: Concentration distribution of dissolved gasses in the PTL in the design without flow channels	111
Figure 53: Calculated distribution of the dissolved gasses inside the cell.....	112
Figure 54: A 3-D cross section of cell showing the channel dimensions	114
Figure 55: Effect of channel width on the performance of cell operating at 60 °C and 1 bar	114
Figure 56: Effect of channel height on the performance of cell operating at 60 °C and 1 bar	116
Figure 57: Summary of the predicted contribution of all irreversible losses to the cell polarization.	120
Figure 58: Comparison of the performance of the conventional cell design and the design without flow channels.	124

List of Tables

Table 1: Thermodynamic quantities of the reaction species	6
Table 2: Exchange current density for commonly used electrocatalysts for the OER of PEM water electrolysis	11
Table 3: Exchange current densities of typical electrode materials for the HER of PEM water electrolysis	12
Table 4: Comparison of the water electrolysis technologies for hydrogen production	21

Table 5: DOE 2020 targets for Distributed Water Electrolysis	28
Table 6: Summary of some major players in stack development	40
Table 7: Properties of a typical sintered titanium PTL	42
Table 8: Summarized boundary conditions for the model of the design with flow channels..	67
Table 9: Summarized boundary conditions for the model without flow channels	68
Table 10: Values of the electro-kinetics parameter used.....	77
Table 11: Measured HF impedance of the test cells and baseline cell and the resulting IR correction term.....	84
Table 12: Summary of the effects of current density, operating temperature and cell design on the voltage drop due to the interfacial contact resistance	91
Table 13: Qualitative comparison of the performance of both cell designs based on the operating conditions, PTL microstructure and design parameters.....	118
Table 14: Summary of all reversible and irreversible losses as a percentage of the total cell voltage, at different current densities. Simulated at 80 °C, 1 bar and 0.6 l/min water flow rate, with the baseline PTL properties. For the conventional cell design.....	121
Table 15: Summary of all reversible and irreversible losses as a percentage of the total cell voltage, at different current densities. Simulated at 80 °C, 1 bar and 0.6 l/min water flow rate, with the baseline PTL properties. For the design without flow channels.....	122
Table 16: Recommendations for a 25 cm ² active area low cost cell design without flow channels to achieve comparable performance with a conventional cell design (25 cm ²) operating at current densities of up to 5 A/cm ²	124

Chapter 1

General Introduction

This chapter starts with an explanation of the role of water electrolysis technologies in the hydrogen and renewable energy economy. After that, a general overview of the water electrolysis concept, including the thermodynamics, reaction kinetics, performance losses and performance characterisation will be presented. This will be followed by a brief introduction in to some of the different water electrolysis technologies and how they compare with each other. Special emphasis will then be placed on the polymer electrolyte membrane (PEM) water electrolysis technology, which is the subject of this thesis. The concept of the PEM water electrolysis technology and the materials and design of a typical PEM electrolysis cell will be discussed.

The chapter will end with a discussion on some of the major challenges that are facing the PEM water electrolysis technology in terms of its commercialization, vis-à-vis other known water electrolysis technologies. The challenges discussed here will form the basis for establishing the motivation and objectives of this thesis in the next chapter.

1.1 Renewable energy sources and the hydrogen economy

The demand and use of energy has always been central to the world's economic and social development. Throughout history, humans have developed several ways of converting and using energy in order to sustain and/or improve livelihood. Early humans depended solely on natural energy flows, such as, wind, solar and water. However, with the dawn of the industrial revolution in the 1800's and the invention of the steam engine, the increased demand for energy

inspired the unlocking of the vast deposit of energy sources such as coal, oil and gas (also known as conventional energy sources) buried under the surface of the earth. Since then, the increased availability of the conventional energy has continuously led to improvement in economic growth and living conditions, but also, to an irreversible impact on the environment.

The scramble for the vast, but not unlimited conventional energy deposits is causing social strife and wars, while, its use is causing pollution, global warming and accelerates environmental damage. It has become clear that, if humans have to fully enjoy the benefits of energy in a sustainable way without jeopardizing the environment, it is imperative to reconsider the kind of energy that is produced and the ways that they are used. It is therefore, not surprising that humankind has made a full cycle and the return to natural energy sources such as solar, wind and water are being developed as the sustainable and renewable energy sources for the future.

For all its advantages and inexhaustible abundance, several challenges have to be overcome in order to adequately replace the conventional energy sources with renewable ones. For one, the supply must be reliable and continuous; meaning that the energy must be supplied in the time and volume needed and at an affordable price. The intermittency in the natural supply of the major renewable sources such as solar and wind presents a major bottleneck in their replacement of conventional energy sources. For example, how can the energy demand be met at night or during long winter days when the sun doesn't shine, if the energy supply is based solely on solar? How can the energy supply be guaranteed at times of very low wind speed or when there is no wind at all, if it is completely dependent on wind turbines?

The possibility to store the excess energy from renewable sources during peak production for use in times or places of low or no production can be a practical means to curb the problem of intermittency, increase load balance maintenance, ensure stable and reliable energy supply and to bridge the gap between conventional and renewable energy supply. Several energy storage

technologies are already in existence, depending on the renewable energy source and the end use application.

The electrochemical technology uses storage units such as lead-acid batteries, lithium ion batteries and redox flow batteries to store excess of renewable energy for use in power applications. Thermal storage technologies stores renewable energy sources (RES) for cooling and heating of buildings and for use in high-temperature systems for power plants. The materials based technology converts and store the RES in the form of high energy carrier substances such as methanol and hydrogen.

The production of hydrogen is one of the most efficient storage means of RES especially when needed for off-site applications [1–3]. Hydrogen is not only a means of electrochemical energy storage but, it is also an energy carrier which can be used as fuel in fuel cells to generate electricity and to run FCEVs as an alternative to petrol run combustion engine engines [4]. The expression “hydrogen economy” is a concept that was proposed by Bockris in 1970 [5] as an efficient system of delivering energy using hydrogen. Because hydrogen in its elemental or molecular form does not exist in nature, in order to realize the goals of the hydrogen economy, hydrogen has to be produced somehow. Water is the most abundant known source of hydrogen and the splitting of water using electrical energy into its constituent components (water electrolysis) is currently considered the most efficient and sustainable process for hydrogen generation, especially when coupled with renewable energy sources [6].

1.2 Hydrogen production by water electrolysis

The electrolysis of water is the decomposition of water into protons, electrons and oxygen gas by the passing of electric current through it. The concept of water electrolysis has been known since 1800 when Volta invented the voltaic pile [7]. But it was not used for industrial hydrogen production because steam reforming was by far the cheaper and more established technology

[8,9]. With the onset of the oil crisis in the early 1970's greater interest in alternative energy sources resulted to increased research and development endeavours in water electrolysis, involving improved materials and cell designs [10–12]. With the development and use of polymer electrolyte membrane (PEM) electrolyzers in submarines, aircrafts and space vehicles in the US military as oxygen generator, the water electrolysis technology further gained wider recognition and attention [13–16].

The principle of water electrolysis is depicted in Figure 1 and Eq. 1. When a potential difference is imposed across the electrolyte (water), the positive ions (including hydronium ions) move through to the negative electrode (cathode), while the negative ions migrate over to the positive electrode (anode). If the potential difference is sufficiently high, this may lead to the formation of oxygen gas at the anode and hydrogen gas at the cathode.

The water electrolysis process is endothermic and, the overall reaction for the production of one mole of hydrogen is:



If the anions and cations are allowed to mix, they may neutralize each other or may accumulate to form an explosive oxyhydrogen mixture. Hence, the electrode compartments are usually separated by a suitable selectively porous membrane to facilitate the accumulation and evacuation of the produced gasses. The type of membrane used usually determines the type of water electrolysis technology.

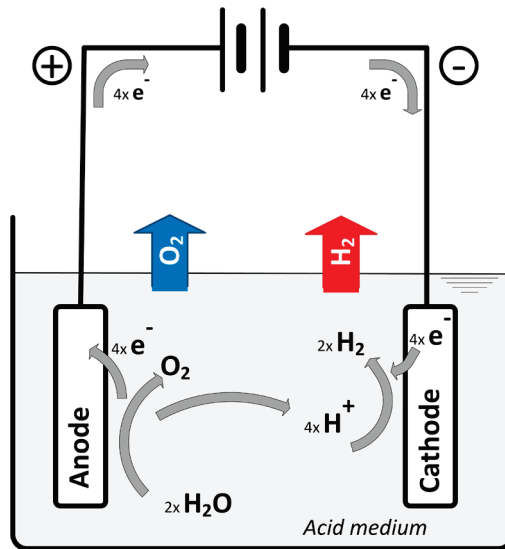


Figure 1: Basic principle of a water electrolysis cell [17]

When coupled with RES, water electrolysis is potentially the most environmentally friendly and cost effective method of producing hydrogen as a fuel. State-of-the-art water electrolysis systems are however, commercially not very viable, compared with other hydrogen production technologies, due to the high capital and operating costs involved, especially the costs of the electricity used [18–20].

1.2.1 Thermodynamics of water electrolysis

The water electrolysis process is endothermic, so, exergy equalling to the sum of the change in Gibbs free energy ΔG and thermal energy $T\Delta S$ is required to shift the reaction from the thermodynamic equilibrium. The change in Gibbs free energy is the component that has to be applied as work (e.g. by electrical energy) and it is known from the second law of thermodynamics, while the thermal energy term is related to the change in entropy of the reaction. The sum of the free energy and entropy terms is the total enthalpy for the water splitting reaction, Eq. 2.

$$\Delta H_R = \Delta G_R + T\Delta S_R \quad \text{Eq. 2}$$

Basically, the change in enthalpy of reaction ΔH_R can be estimated from the sum of the stoichiometric enthalpies of formation of the reactants minus the sum of stoichiometric

enthalpies of formation of the products. Similarly, the change in entropy is the sum of the stoichiometric entropy of the reactants minus the stoichiometric entropy of the products. The ideal gas enthalpy and entropy of formation for the species involved in Eq. 1 are summarized in Table 1.

Table 1: Thermodynamic quantities of the reaction species [21]

	Enthalpy of formation (H_f) [kJ mol ⁻¹]	Entropy (S) [kJ mol ⁻¹ K ⁻¹]
O ₂	0	0.205
H ₂	0	0.130
H ₂ O(l)	285.80	0.069
H ₂ O(g)	241.80	0.189

The enthalpy of reaction corresponds to the heat of formation of water which is equal to 285.8 kJ mol⁻¹ and 241.8 kJ mol⁻¹ for water in the liquid and gas phase respectively, at standard conditions of 25 °C and 1 atm. The enthalpy of formation of water in the liquid phase is known as the higher heating value (HHV) of water, while the enthalpy of water in the gas phase is known as the lower heating value (LHV).

The change in the enthalpy and entropy of reaction can therefore, be calculated as follows:

$$\Delta H_{R,l}^0 = H_{H_2}^0 + \frac{1}{2}H_{O_2}^0 - H_{H_2O}^0 = 285.8 \text{ kJ mol}^{-1} \quad \text{Eq. 3}$$

$$\Delta S_{R,l}^0 = S_{H_2}^0 + \frac{1}{2}S_{O_2}^0 - S_{H_2O}^0 = 0.163 \text{ kJ mol}^{-1}K^{-1} \quad \text{Eq. 4}$$

Putting Eq. 2 to Eq. 4 together, the amount of the Gibbs free energy needed for the reaction can be calculated.

$$\Delta G_{R,l}^0 = \Delta H_R^0 - T\Delta S_R^0 = (285.8 - 0.163 * T) \text{ kJ mol}^{-1} \quad \text{Eq. 5}$$

The minimum thermodynamic voltage necessary to activate the water splitting process is called the reversible cell potential, which is directly related to the change in Gibbs free energy as in Eq. 6.

$$E_{rev} = \frac{\Delta G_R}{nF} \quad \text{Eq. 6}$$

Where F is the Faraday's constant and n is the number of electrons transferred per mole of hydrogen produced in the water splitting reaction, which is equals to 2. At standard conditions, 25 °C, putting Eq. 5 and Eq. 6 together, the reversible cell potential is 1.229 V.

As can be seen, an additional thermal source (the entropy term) must be available to attain the reversible cell voltage. When there is no heat source to account for the entropy term, all the energy required for the electrolysis process must be supplied by electricity. In this case, the minimum thermodynamic voltage for the process to take place adiabatically is higher than the reversible cell voltage and is called the thermo-neutral voltage E_{th} and it corresponds to the HHV of water.

$$E_{th}^0 = \frac{\Delta H_R^0}{nF} = 1.481 \text{ V at } 25 \text{ }^\circ\text{C} \quad \text{Eq. 7}$$

The reversible and thermo-neutral cell voltages as described thus far are for standard conditions of temperature and pressure. However, these can be affected by changes in temperature and pressure.

Figure 2 shows the effect of temperature on the total energy demand of water electrolysis. At high temperatures, a significant contribution to the total energy demand can be provided as heat. The joule heat which is produced by the passage of electrical current through the cell can also be utilized at high temperatures. As a result, the overall electrical energy demand can be reduced with increasing temperature.

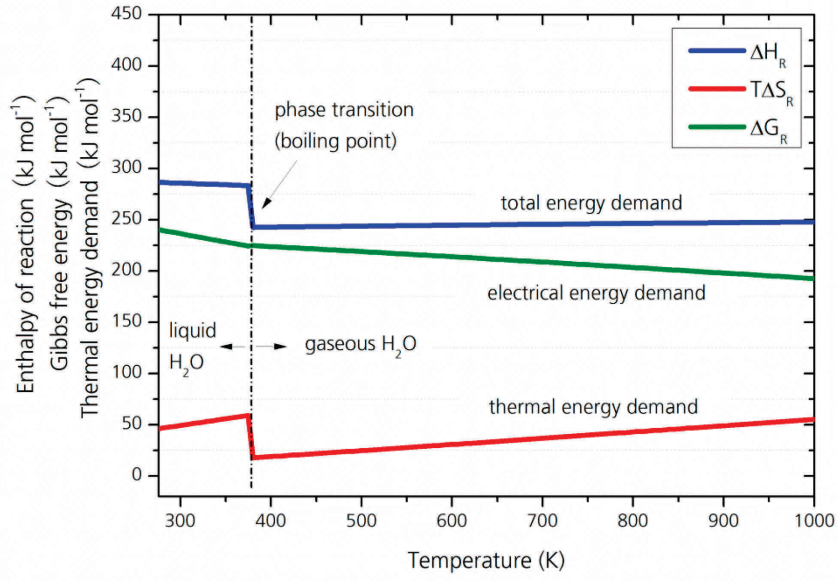


Figure 2: Total energy requirements for water electrolysis as a function of temperature at standard pressure [17]

The temperature and pressure dependency of the reversible cell voltage is described by the Nernst equation:

$$E_{rev} = E_{rev}^0 - \frac{RT}{nF} \ln \left(\frac{p_{H_2O}}{p_{H_2} p_{O_2}^{1/2}} \right) \quad \text{Eq. 8}$$

In the case where the overall pressure is the same at the anode and cathode, the change in the reversible voltage with change in temperature then becomes:

$$\Delta E_{rev} = (E_{rev} - E_{rev}^0) = -\frac{RT}{nF} \ln \left(\frac{1}{p_{H_2O}^{1/2}} \right) \quad \text{Eq. 9}$$

As is summarized in Figure 3, an increase in temperature leads to a decrease in the reversible cell voltage Eq. 8. While, an increase in pressure yields an increase in the reversible cell voltage Eq. 9.

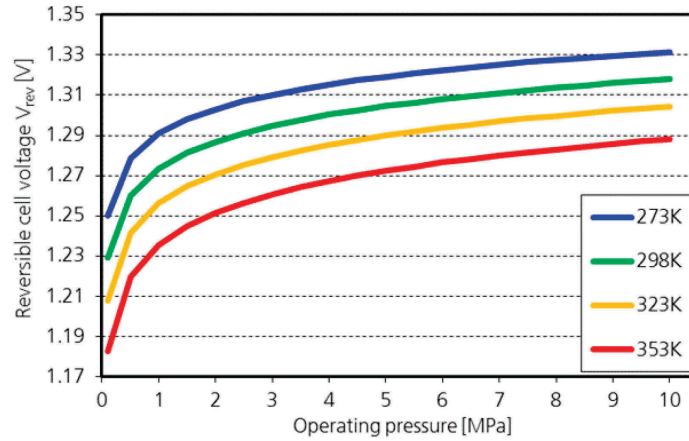


Figure 3: The reversible cell voltage as a function of temperature and pressure [17]

1.2.2 Reaction kinetics

Once electric current is passed through the water electrolysis cell, there is a shift from the thermodynamic equilibrium and the actual cell voltage becomes much higher than the reversible cell voltage, due to the onset of irreversible kinetics losses. The major mechanisms that lead to these kinetics losses are mainly three fold: 1) activation losses from the electrode reaction kinetics; 2) ohmic losses from the resistance to the flow of protons through the electrolyte; and 3) mass transport losses. These irreversible losses are called overpotentials and the loss mechanisms can be faradaic or non-faradaic in nature.

The faradaic losses occur when there is a direct exchange of one or more electrons between the redox species. The activation loss mechanism is faradaic because it involves the direct transfer of electrons at the interface between the electrode and the electrolyte of the OER and the HER. The activation overpotentials therefore depend on the rate of transfer of electrons or in other words, the rate of the electrochemical reaction at the electrodes. The rate of transfer of the electrons is the electrical current. Since electrochemical reactions typically occur only at interfaces, the current is therefore expressed more fundamentally in terms of the surface area of the interface, Eq. 10, and, is called the current density.

$$j = \frac{J}{A}$$

Eq. 10

In order for the water splitting reaction to occur, an activation energy must be supplied and, the probability to overcome this barrier determines the rate of the reaction and this can be facilitated by the use of appropriate catalysts, Figure 4.

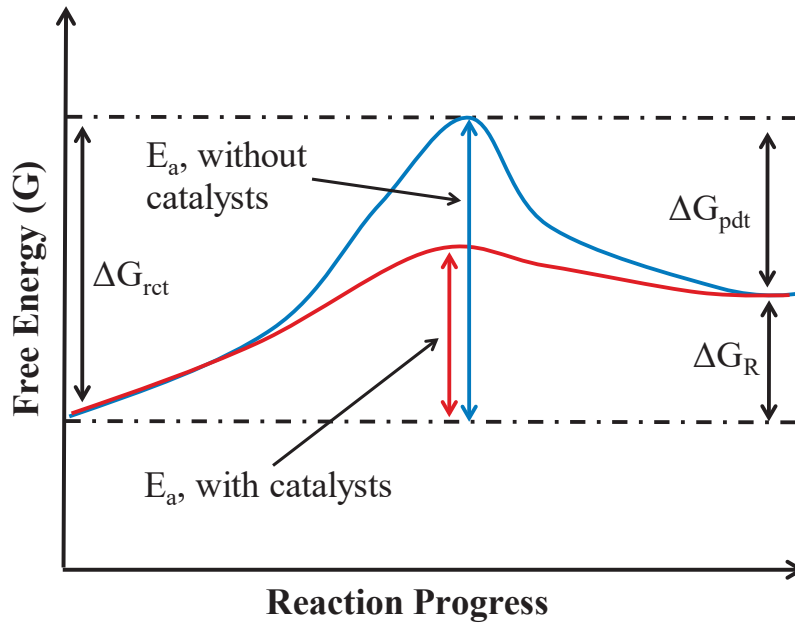


Figure 4: Activation energy vs. reaction progress. ΔG_{rct} , ΔG_{pdt} and ΔG_R are the changes in the Gibbs free energy of the reactants, the products and the reaction respectively

At thermodynamic equilibrium, the activation energy and the reaction rates are directly related by the Arrhenius equation.

$$\frac{j}{nFA} = e^{\frac{-E_a}{RT}}$$

Eq. 11

The net electrochemical reaction rate is the forward reaction rate minus the reverse reaction rate. The net reaction rate can therefore be expressed as:

$$j = nFAk \left\{ e^{\frac{-\Delta G_{rct}}{RT}} - e^{-\left(\frac{\Delta G_{rct} - \Delta G_R}{RT}\right)} \right\}$$

Eq. 12

Where ΔG_{rct} and ΔG_R are the change in Gibbs free energy for the reactants and the overall reaction respectively. At the thermodynamic equilibrium, there is no net current density and

the forward and backward reactions are characterized by the so called exchange current density. The magnitude of the exchange current density determines the rate at which the electrochemical reaction progresses and depends greatly on the electrode material, surface properties and the temperature and pressure. The net reaction rate can then be expressed in terms of the exchange current density as in Eq. 13:

$$j = j_o \left\{ e^{\frac{-\Delta G_{rct}}{RT}} - e^{-\left(\frac{\Delta G_{rct} - \Delta G_R}{RT}\right)} \right\} \quad \text{Eq. 13}$$

Where j_o is the exchange current density. The current density is the property of the catalyst that determines the rate of the electrochemical reaction at thermodynamic equilibrium. Exchange current densities for typical electrocatalyst materials used in PEM electrolysis are shown in Table 2 (for the OER) and Table 3 (for the HER).

Table 2: Exchange current density for commonly used electrocatalysts for the OER of PEM water electrolysis [22]

Electrode material	Exchange current density [A/cm²]
Ru-Oxide	1.2 x 10 ⁻⁸
Ir / Ru-Oxide	3.2 x 10 ⁻⁹
Ir-Oxide	5 x 10 ⁻¹²
Ir	9.4 x 10 ⁻¹⁰
Rh-Oxide	7.5x10 ⁻⁹
Rh	5.1 x 10 ⁻⁹
Pt	1.7 x 10 ⁻¹¹

Table 3: Exchange current densities of typical electrode materials for the HER of PEM water electrolysis [23]

Electrode material	Exchange current density [A/cm ²]
Pt on carbon support	2×10^{-1}
Ir on carbon support	5×10^{-2}
Pd on carbon support	5×10^{-3}

The applied voltage is the driving force for the electrochemical reaction so, changes in the voltage leads to changes in the free energy available for the reaction. Applying a finite potential difference across the electrode lowers the activation energy barrier by a fixed amount α , called the symmetry factor or the electron transfer coefficient $0 < \alpha < 1$, which determines how the electrical energy input affects the redox process. The activation barrier of the forward reaction is therefore decreased by a factor of $n \cdot \alpha \cdot F \cdot \eta$ and that of the reverse reaction is increased by $n \cdot (1 - \alpha) \cdot F \cdot \eta$. Where η is the activation overpotential and it is the difference between the applied potential and the reversible potential for the charge transfer reaction. In terms of the overpotential and the exchange current density, the net reaction rate becomes the so called Butler-Volmer equation for charge transfer kinetics, Eq. 14.

$$j = j_o \left\{ \exp\left(\frac{n \cdot \alpha \cdot F \cdot \eta}{RT}\right) - \exp\left(-\frac{n \cdot (1 - \alpha) \cdot F \cdot \eta}{RT}\right) \right\} \quad \text{Eq. 14}$$

The Butler-Volmer relationship indicates that the current density produced (or consumed) by an electrochemical reaction increases exponentially with the overpotential as shown in Figure 5.

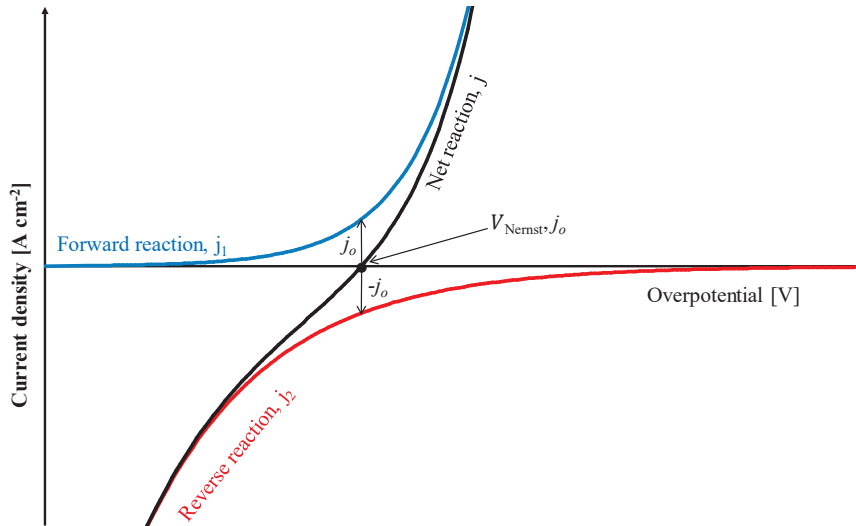


Figure 5: Butler-Volmer dependence of the current density and overpotential. With current density j and exchange current density j_o

Increasing the exchange current density hugely increases the electrode kinetics of the water splitting reaction. The exchange current density can be increased by decreasing the activation barrier and this can be achieved by increasing the temperature. The activity of the electrode can be further enhanced by increasing the number of active reaction sites through increasing the surface roughness of the electrode.

Ohmic and mass transport loss mechanisms do not result from the direct transfer of electrons in the electrodes and are therefore, non-faradaic in nature. Ohmic overpotentials result from the resistance of the flow of electrical currents through the cell components and the flow of protons through the polymer electrolyte membrane. The total ohmic losses (ohmic overpotential) are determined by the application of the Ohm's law:

$$\eta_{ohm} = j \cdot ASR = \frac{j}{A} \cdot \sum R_{ohm,i} \quad \text{Eq. 15}$$

Where ASR is the overall area-specific resistance of the cell, which is the sum of all electrical and ionic (ohmic) resistances $R_{ohm,i}$ of the cell components connected electrically in series.

The electron transfer mechanism assumes that the supply of reactant to and removal of product species from the reaction interface is not limited, and thus, the reaction kinetics is strictly

faradaic in nature. The rate of transport of the reactant species to and the removal of products from the reaction sites can, however, affect or may even dominate the kinetics when the reaction shifts from thermodynamic equilibrium. Different forms of transport phenomena that influence the reaction rate and leads to mass transport losses are migration, diffusion, and convection as shown in Figure 6. Migration refers to the movement of charged particles under an electric field and its effect dominates in the faradaic (activation or electrode kinetics) region where the water splitting reaction is controlled by the transfer of electrons and protons.

When the electrode kinetics is infinitely fast, there is zero accumulation of reactants on the electrode surface as it is being quickly used up, and the reaction becomes concurrently controlled by the diffusion and convection mass transport mechanisms. The diffusion transport mechanism is driven by a concentration gradient as dissolved species move from regions of high concentration to low concentration. When the dissolved gasses are produced faster than they can diffuse from reaction surface, this may lead to mass transport overpotential due to diffusion. The extreme form of mass transport overpotential occurs when the reactant water is prevented from reaching the reaction surface by convection. This is usually due to the formation of gas bubbles at the reaction interface.

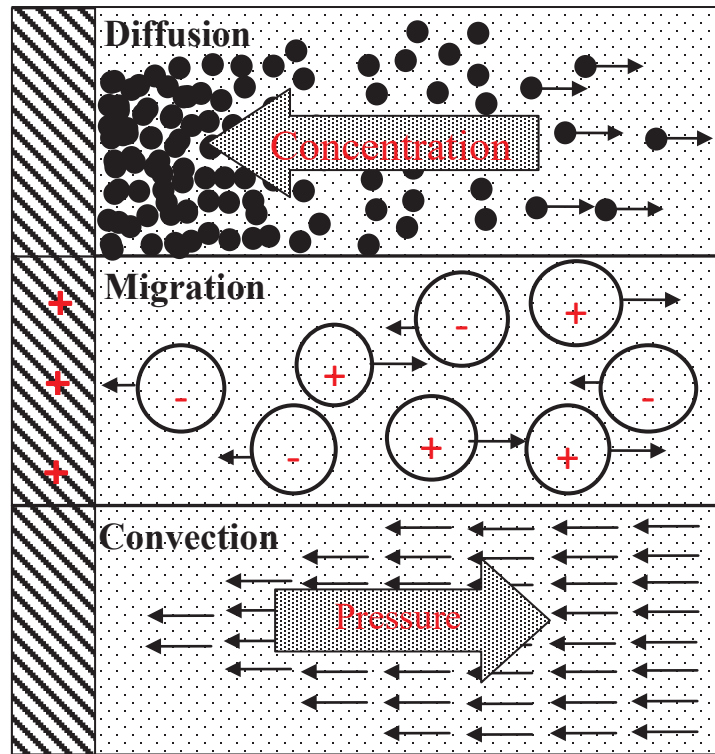


Figure 6: Schematic of the mass transport mechanisms

For the water splitting reaction to be sustained, feed water needs to be supplied to the reaction interface at an appropriate rate. The rate of reaction will then be determined by the rate of supply of the reactants. Since the half-cell reaction occurs on porous electrode surfaces and since there are no more than two component mixtures for the anode (water and oxygen) and cathode (water and hydrogen) reactions, Fick's diffusion is assumed to be the dominant mass transport mechanism.

The Nernst equation for determining the non-equilibrium electric potential of the electrochemical reaction is given by [24]:

$$V = E_{rev} + \frac{RT}{nF} \ln(k) \quad \text{Eq. 16}$$

The overpotential due to mass transport is then the difference between the cell voltage and the equilibrium reversible cell voltage. In Eq. 16, k is the reaction rate constant at equilibrium and it is given by the ratio of products concentration at the electrode interface to that at a reference

position. Eq. 16 therefore shows that, the overpotential due to diffusion increases with increasing product concentration at the reaction interface.

Diffusion however, dominates mass transport losses only at low current densities (typically below 1 A/cm²). PEM electrolysis cells can be operated at very high current densities, sometimes well above 3 A/cm². At such high current densities, the production of the gas phase in the form of bubbles shields the active area, distorts the contact between the electrode and the electrolyte, and reduces the catalyst utilization. This results in an increase in the local current density and the so-called bubbles' overpotential, which increases exponentially with increasing current densities [25] as is shown in Figure 7.

1.2.3 Performance characteristics

The performance and behaviour of an electrolysis cell can be characterized by the so called polarization curve, which is a plot of the current density against the cell voltage. The electrolysis polarization curve has three distinct sections depicting the behaviours of the activation, ohmic and mass transport mechanisms, as shown in Figure 7. The activation mechanism is dominant at low current densities while the ohmic loss mechanism is dominant at mid current density region and mass transport and bubbles losses at high current densities.

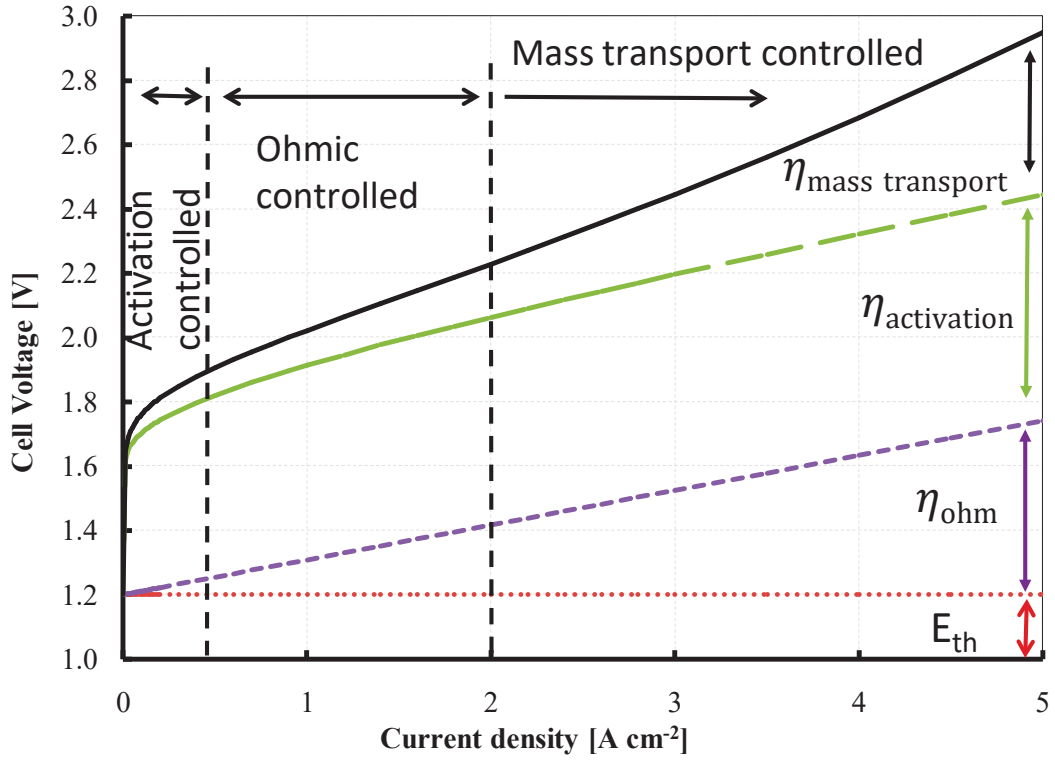


Figure 7: The regions of a typical polarization curve of a PEM water electrolysis cell including an estimation of the contribution of the main sources of overpotentials and the reversible cell voltage to the cell polarization

Since the cell components are typically arranged electrically in series, all voltage losses from the anode and the cathode sides can be summed up to give the total cell polarization. The cell voltage V_{cell} which is a measure of the total amount of electrical energy demand for water decomposition, then results from the sum of the reversible cell voltage E_{rev} and all irreversible losses within the cell.

$$V_{cell} = E_{rev} + |\eta_{act,anode}| + |\eta_{act,cath}| + \sum |\eta_{ohm}| + \sum |\eta_{mass\ transport}| \quad \text{Eq. 17}$$

The theoretical background of the major water electrolysis technologies and their underlying issues will next be discussed, with extended focus on the PEM water electrolysis technology which is the focus of this thesis.

1.3 Alkaline water electrolysis

The alkaline water electrolysis is the most matured water electrolysis technology [26,27]. As its name implies, it uses an aqueous alkaline solution as electrolyte, usually KOH and NaOH in which the electrodes are immersed. The electrodes are separated by a diaphragm which separates the product gasses. It is commonly known as a low pressure and temperature process because it operates generally at atmospheric pressure and at temperatures between 50 and 80 °C. The typical operating current densities are between 0.2 to 0.45 A/cm² with corresponding cell voltages between 1.8 to 2.4 V and typical cell voltage efficiency of 52 – 69 % [28,29].

The electrolyte of the alkaline electrolyser has high thermal mass and as a result the energy and time needed to warm up the cell to the required temperature is very high. This increase in response time makes the alkaline water electrolysis technology not very feasible for dynamic operations and for the incorporation with RES [30].

1.4 High temperature water electrolysis

The high temperature water electrolysis technology such as solid oxide electrolysis cell (SOEC) makes use of the higher kinetics at high temperatures and also by reducing the electrical energy contribution to the theoretical cell voltage, by making up for it with the temperature (entropy) term. It can indeed, operate exclusively without external heat input especially when coupled with waste heat from nuclear, geothermal or solar sources.

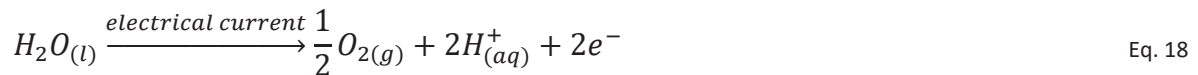
It is also called solid oxide electrolysis because it uses a solid oxide electrolyte, commonly; Yttria stabilized Zirconia (YSZ) which selectively permits the transport of oxide ions from the cathode to the anode electrode. Typical operating temperature is about 750 – 1000 °C and at current densities between 0.2 and 0.8 A/cm², with corresponding cell voltages well below the thermo-neutral cell voltage [31,32].

Just like with AEL, high temperature water electrolyzers exhibit long start up times, which leads to poor dynamic response. Additionally, the high operating temperature poses a problem with material stability and durability and reduces possible material candidates for its operation.

1.5 PEM water electrolysis

The polymer electrolyte membrane, also known as proton exchange membrane or solid polymer electrolyte (SPE) membrane electrolysis traditionally makes use of a perfluorosulfonic acid polymer which selectively allows the conduction of protons through it, while separating the produced gasses and electrically insulating the electrodes.

The net reaction for the PEM water electrolysis process is the same as in Eq. 1. The reactant liquid water is fed to the anode catalyst with an applied voltage over the cell. The supplied water is oxidized to oxygen, protons and electrons. This anode half reaction is called the oxygen evolution reaction (OER). The anode half reaction for the production of one mole of hydrogen is shown in Eq. 18.



The protons are transported through the proton exchange membrane to the cathode side, while the electrons are transported through the external circuit to the cathode, see Figure 8, where they recombine with the protons to produce gaseous hydrogen. This cathode half reaction is called the hydrogen evolution reaction (HER), Eq. 19.



The PEM electrolysis process is a low temperature technology as it operates best at temperature between 20 °C and below the boiling point of water, typically at 80 °C. The kinetics of the electrode reaction is enhanced by increasing the temperature, but at temperatures close to the boiling point of water, the components of the PEM electrolysis cell become unstable. Nafion®

which is commonly used as the polymer electrolyte for example starts to lose its mechanical stability at such temperatures and the metal components become susceptible to electrochemical corrosion. State-of-the-art PEM electrolysis cells operate typically at current densities of 0.5 to 2.5 A cm⁻², achieving corresponding cell voltage of 1.7 to 2.1 V [33]. Typical operating pressures range from atmospheric up to 5 MPa, with dry hydrogen production efficiency of up to 99.99 % [34]. Higher pressure operating systems up to 20 MPa are however, being considered in order to reduce the balance of plant cost, especially in applications where the hydrogen is stored under pressure [35].

Although the alkaline water electrolysis is the more established technology, PEM water electrolysis has some distinct advantages over its older counterpart, such as:

- PEM electrolysis cells can operate at much higher current densities, thereby, reducing the hydrogen production costs.
- The cell design is much simpler and compact, since only pure water is fed into the cell.
- Because of its low thermal mass, PEM electrolysis cells can respond much quickly to power in-put, which makes it more suitable for use with a wide range of power sources.
- The thin polymer electrolyte membrane allows for shorter pathway for proton transport, thus lowering the ohmic losses.
- Gas purity from the PEM electrolysis is much higher because of low gas crossover and no mixture of gasses with liquid electrolyte, as is with the alkaline cell.
- The compactness of the PEM cell makes it suitable for high pressure operations, thereby, reducing system and hydrogen production costs.

In spite of these advantages, there are as well certain drawbacks facing PEM water electrolysis, compared with other water electrolysis technologies. Table 4 compares the water electrolysis technologies for hydrogen production.

Table 4: Comparison of the water electrolysis technologies for hydrogen production

Technology	Temperature (°C)	Charge carrier	Disadvantages
PEM	20 – 100	H^+	Not well established
			High cost of components
			Acidic environment and corrosion
			Lower durability than AEL
			Commercialization challenge
Alkaline	40 – 90	OH^-	Low current density
			Low gas purity
			Poor with dynamic operation
			Low partial load
			Lower operational pressure, up to 50 bar
			Liquid and corrosive electrolyte
High temperature	750 – 1000	O^{2-}	Limited thermal cycling
			Low durability
			Bulky system design

1.5.1 Design and components of a conventional PEM electrolysis cell

Figure 8 depicts the typical (conventional) set-up of a PEM water electrolysis cell. The membrane electrode assembly (MEA) consisting of the membrane and electrodes is at the centre of the cell, symmetrically separating it into two equal compartments; the anode (oxygen production) and the cathode (hydrogen production) compartments. The major cell components and their functions will be discussed next.

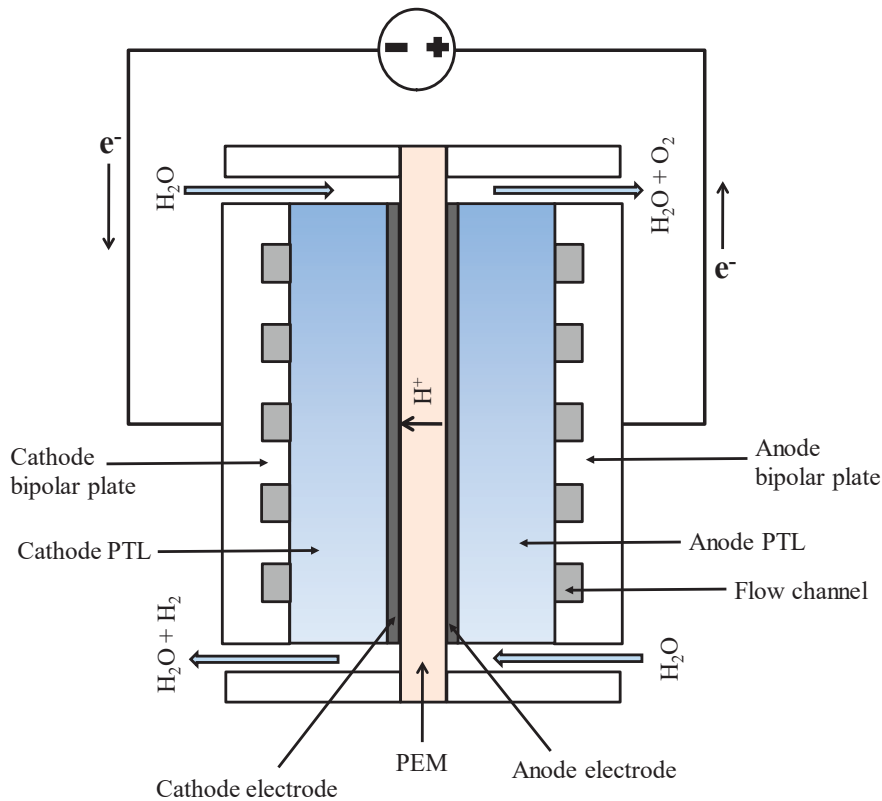


Figure 8: Basic design principle of a conventional PEM water electrolysis cell

Membrane Electrode Assembly (MEA)

The MEA is made up of the proton conducting membrane, PEM, sandwiched between the anode and the cathode electrodes. The membrane is only proton conducting while the electrodes are electron conducting. The MEA has three major functions; 1) to enable the transfer of protons from the anode to the cathode side, 2) to prevent the crossover of produced gasses from one compartment to the other, hence ensuring the production of high purity gasses and 3) provides electrical isolation. Typically, Perfluorosulfonic acid (PFSA) such as Nafion® from DuPont is the proton conducting membrane used in PEM water electrolysis. A good membrane therefore, must have high proton conductivity and low gas permeability.

The electrodes consist of a mixture of porous catalysts and ionomer of the membrane and it is where the electrochemical reactions occur. Precious metals are typically used as catalysts, thus giving the electrodes the ability to conduct both electrons and protons. Material properties of

commonly used electro-catalysts are shown in Table 2 and Table 3 above. In state-of-the-art MEAs, the electrodes are directly coated on the membrane and they have catalyst loading of 1 – 2 mg/cm² on the anode and ~1 mg/cm² on the cathode [36].

Bipolar Plates (BiP)

In a PEM water electrolysis cell or stack, the bipolar plate is an electrically conducting sheet that physically separates adjacent cells while at the same time electrically connecting them. It is aptly called a “bipolar” plate because it serves as the anode in the one cell and as the cathode of the adjacent cell. Consequently, the use of the term “bipolar plate” becomes ambiguous in a single cell, since its bipolar function becomes redundant.

Traditionally, grooves are milled on the bipolar plates Figure 9, which serve the additional function of adequately distributing feed water for electrolysis through the cell and for the evacuation of produced gases out of the cell to ensure an efficient mass transport regime.



Figure 9: A conventional bipolar plate with machined flow channels [28]

In a single cell where the plate serves only the function of water distribution and gas removal, it is usually referred to as the end plate (not to be confused with the component, end plate described below which in this case is traditionally called the pressure plate). In order to reliably serve the functions for which it is designed, the bipolar plates have to demonstrate high electrical conductivity, high mechanical and electrochemical stability and impermeability to

gasses. For this reason, the use of stable metals such as titanium is common in PEM water electrolysis.

End plates

The end plate is one of the main components of a PEM electrolyser. Conventionally, stack (cell) components are assembled between two end plates, which serve as a supporting structure for the unit cells, see Figure 10. Consequently, the end plate bears the entire mechanical load applied on the stack (cell) through clamping bolts and, provides passage for reactant water and product gasses in and out of the stack (cell) respectively. The major role of the end plate though, is to provide a uniform and optimal pressure distribution between various components of the stack (cell). Through the distribution of pressure between sealing rings and relevant stack (cell) components (external stack), water and gas tightness of the stack is achieved. While, by the distribution of contact pressure between the bipolar plates and current collectors, as well as between the current collectors and the MEA (internal stack), contact resistance between them can be reduced, and consequently improved performance and efficiency of the electrolyser stack (cell).

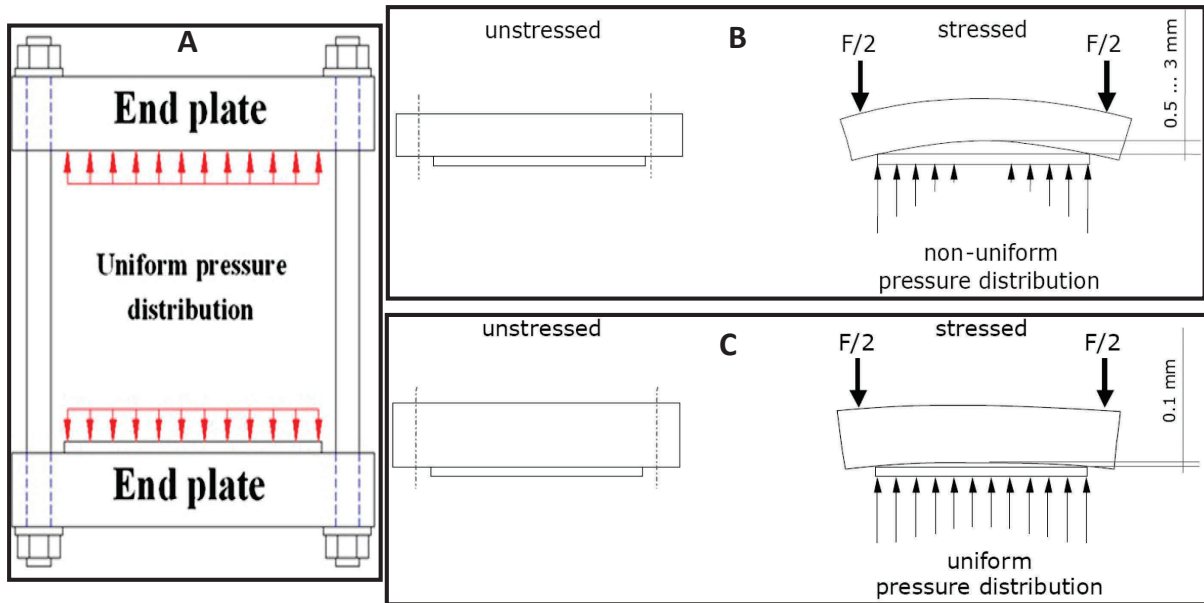


Figure 10: A) Pressure plates serve as supporting structure for single cell components and provide uniform contact pressure distribution, B) High deformation and non-uniform pressure distribution using non-optimised pressure plate, C) Minimal deformation and uniform pressure distribution using an optimized pressure plate [37]

Non-uniformly distributed contact pressure in the internal stack (cell) may result in a non-uniform current density and heat distribution which may cause hot spots formation and ultimately lead to the failure of the MEA. Therefore, the end plate design also has a direct effect on the life time of an electrolysis stack (cell). While large mechanical pressure through the end plates is necessary for tightness and contact resistance minimisation of the stack, over-compressing of the stack may result in the damage of stack components. Excess compression affects the porosity and permeability of the porous transport layer (PTL), and consequently, mass transport in the PTL and the catalyst layer. Excess compression may also lead to failure of the sealing rings or fracture of other stack components if their design tolerances were not tightly chosen. As a result, the clamping pressure applied on the end plates and the design of the end plate must be optimised Figure 10b,c in order to achieve the requirement for low contact resistance while avoiding mass transport limitation and failure or fracture of some major components.

Porous Transport Layer (PTL)

The porous transport layer is also sometimes referred to as current collector. In the PEM electrolysis cell, it is placed between the bipolar (end) plate and the MEA in both the anode and the cathode half cells. The function of the porous transport layer is two-fold; 1) To transport electrical current from the bipolar (end) plate and uniformly distribute it to the active layer (electrode surface) where the water splitting reaction occurs, and 2) Transport of produced gasses from the electrodes to the flow channels of the bipolar (end plates) to be evacuated from the cell at the manifolds.

It is therefore, primordial that the PTL has a high electrical conductivity and gas permeability, high mechanical and electrochemical stability (corrosion), good surface smoothness, as well as optimal porosity and microstructure to be able to perform its functions. Although large pores will facilitate the transport of water to and removal of gases away from the active area, this will also lead to an increase in the resistance of electrical current transport through the PTL and compromise the interfacial contact between the PTL and the electrode and the PTL and the bipolar plate. An optimization of the surface property, porosity and microstructure of the PTL is therefore critical. Typical state-of-the-art porous transport layers for PEM water electrolysis are summarized in Figure 11.

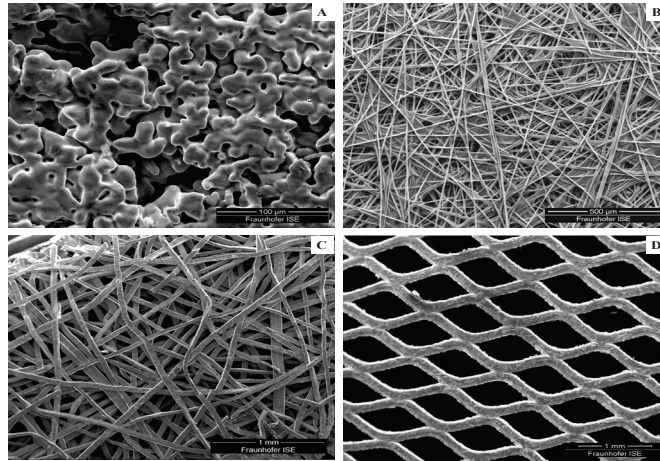


Figure 11: PTL materials commonly employed in PEM water electrolysis. A) Sintered titanium powder B) Carbon paper, non woven C) Sintered metal felt (usually titanium) D) Expanded metal mesh (usually titanium) [28]

1.5.2 Challenges and trends in PEM water electrolysis

In spite of the many advantages that the PEM water electrolysis technology enjoys over other water electrolysis technologies, it still has to overcome certain challenges in order for the technology to be commercially viable. The current trend in research and development efforts in PEM water electrolysis is geared towards attaining targets that are set to address these challenges. The US DOE targets for some of these challenges for distributed water electrolysis are summarized in Table 5.

Lifetime issues

The lifetime issues of a PEM water electrolyser can be categorised under durability and reliability concerns. Durability issues may lead to; 1) Reduction in cell performance, which can be caused by many factors such as, increase in ohmic resistance when cations released from a corroded metal component blocks the electrochemical active area and 2) Low purity of produced gasses which can be a result of gas crossover due to membrane thinning. These two effects reduce the energetic and faradaic efficiency of PEM water electrolysis. While these durability issues may not immediately cause the shut-down of the electrolyser, continuous degradation may eventually lead to reliability concerns

Table 5: DOE 2020 targets for Distributed Water Electrolysis [38]

Challenge	Units	2020 Target
Hydrogen production cost	\$/kg	2.3
System capital costs	\$/kg	0.5
	\$/kW	300
System energy efficiency	% (LHV)	75
	kWh/kg	44
Stack energy efficiency	% (LHV)	77
	kWh/kg	43
Life time	Hours	Comparable to FCEVs (~ 60 000)

Unlike durability issues, reliability issues of a PEM electrolyser are those that will lead to the immediate shut down of the plant, such as safety and component failure. Safety issues typically arise when the gas-cross permeation is so high that the hydrogen content in the anode half cell surpasses the tolerable 5 % threshold to form explosive hydrogen – oxygen gas mixture [39]. Component failures are mostly mechanical and the cell component most vulnerable to failure is the thin MEA [40], as it can easily get punctured. The metal components such as the bipolar plate and the PTLs (current collectors) are also susceptible to mechanical failure due to embrittlement when exposed to hydrogen for long periods and at high pressures [41–43].

Voltage efficiency

The voltage efficiency is the ratio of the thermo-neutral voltage to the actual cell polarization at given operating conditions. Consequently, the efficiency is compromised as a result of the build up of irreversible degradation effects within the cell, viz; activation and ohmic overvoltages, as well as overpotentials due to mass transport. Therefore, in order to improve the voltage efficiency, research trend is focused on; 1) Highly reactive electrocatalysts with

high exchange current densities, 2) Thinner membranes with high proton conductivities, 3) Metallic bipolar plates and PTLs with low resistivity (sometimes, coated with inert metals), 4) Mitigating the mass transport overpotential by optimizing the PTL.

Costs reduction

Two aspects of costs reductions are being considered; 1) stack / cell capital costs or hydrogen production costs and 2) balance of plant (BoP) or system costs. The reduction of hydrogen production (stack) costs can be achieved by:

- Developing new low cost materials and fabrication methods for cell components. As a start, it could be important to reduce the number of parts. Also, expensive metal components could be replaced with cheaper alternatives and the development of fabrication methods suitable for large scale production.
- Increasing the operating current density to reduce the active cell area while maintaining high efficiency.

The motivation for this research work was born out of the necessity to address some of the above challenges facing the establishment of the PEM water electrolysis technology, especially the challenges of hydrogen production costs reduction. In the next chapter, the motivation of this research work will be established and the methods employed to meet its objectives shall be discussed.

Chapter 2

Motivation, Objectives and Methods

In this chapter, the *raison d'être* for this work will be presented. The scientific and analytical tools as well as the materials and methods used to achieve the objectives of the research will be described. By the end of this chapter, the expected contribution of this research work to the broader field of hydrogen production by means of PEM water electrolysis will be established.

2.1 Main issues and objectives

State-of-the-art major commercial electrolysers are based on the alkaline and polymer electrolyte membrane (PEM) technologies. While alkaline electrolysis is the more established and cost effective technology, the inherent ability of operating at very high current densities and the production of high purity gas ($\geq 99.9\%$ hydrogen) gives the PEM technology a clear advantage for a wide range of applications [44–46]. However, cost reduction in the cell components and balance of plant (BoP), is required for wider commercialization of the technology [47].

In the conventional PEM electrolysis cell design, the membrane electrode assembly (MEA) and the porous transport layer (PTL) are pressed between two bipolar plates with machined flow channels to facilitate the transport of water into and gases (hydrogen and oxygen) out of the porous catalyst layers where the water splitting reaction occurs, Figure 12.

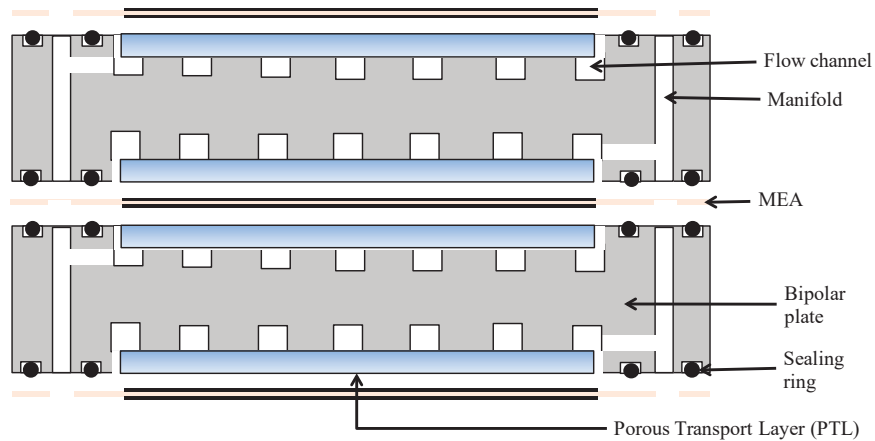


Figure 12: Design concept of a conventional PEM electrolysis stack, with machined channels on bipolar plates

While this concept is well established and has proven to provide adequate flow regimes for heat and water management [48,49], the manufacturing of bipolar plates with machined flow channels, which typically are made from titanium is very expensive.

In fact, a cost analysis for PEM water electrolysis stacks, which accounts for material costs of components and all production stages [50], has revealed that most of the costs (about 50 %) at the component level are borne by the manufacturing cost of the machined bipolar plates, Figure 13.

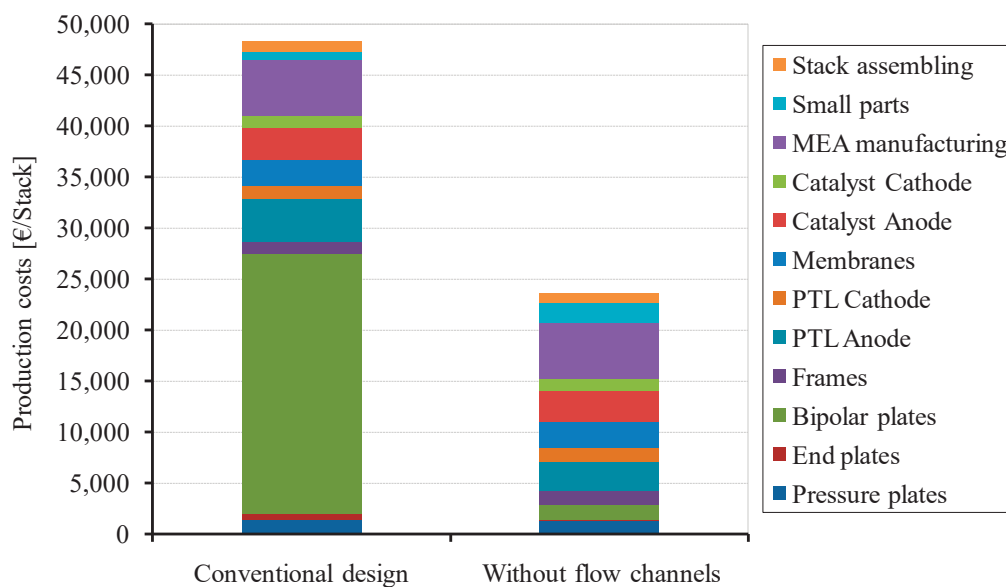


Figure 13: Specific costs breakdown of materials and production costs per stack for both designs. Costs analysis is based on the production of 100 stacks with 300 cm² active cell area, operating at 1 A/cm².

A US DOE report [51] suggested that in order for PEM water electrolysis technology to be cost competitive, the overall state-of-the-art stack capital costs must be reduced by up to 25 %.

An alternative cell design concept has been reported [52,53]. In this simplified concept, the machined bipolar plates with flow channels are replaced with flat sheets of a highly conductive metal such as titanium, thus operating without flow channels. This is accompanied by a 3-D porous transport layer (PTL) which also acts as current collector, Figure 14. This approach provides some advantages over the more established conventional design, such as: a) more compact assembly, b) more uniform internal compression, c) facile assembly of large stacks, and d) amenable to high volume production. The cost analysis of the stack designed without machined flow channels on the bipolar plates showed a cost reduction of close to 50 % on the conventional design concept.

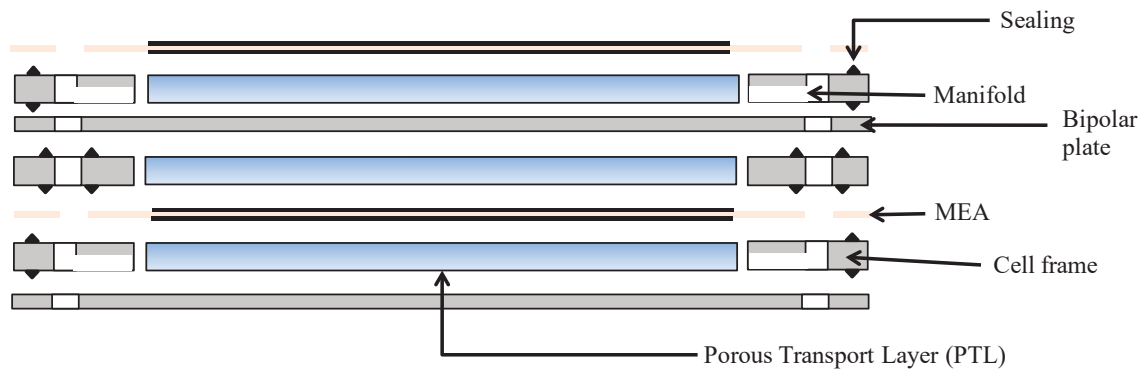


Figure 14: Design concept of a PEM electrolyser without flow channels on the bipolar plates, herein after, referred to as the "Advanced design"

In an attempt to evaluate the two design concepts, two separate cells, one with the conventional and the other with the alternative design concept without flow channels were constructed and tested. In both test cells, (non commercial) expanded titanium mesh as shown in Figure 11D where used as the porous transport layer. The MEA used were the commercial product E300E acquired from Greenerity®, formerly known as SolviCore from Hanau, Germany. The test station on which the test were performed was operated in a dual (anode and cathode) feed mode

at balanced pressures. However, the station was designed for a maximum operating current density of 3 A/cm². Also, the test station was designed for a fixed operating water flowrate of 0.3 l/min. It was therefore, not possible to study the effects of varying water flowrates and high current densities up to 5 A/cm². Polarisation curves measured In Situ in both cells Figure 15 revealed some interesting comparisons between the performances of both design concepts:

- Both cells performed comparatively the same in the activation region at low current densities, $0 < j < 0.2$ where the electro-catalyst activity has the most dominant effect on the PEM electrolysis cell's performance.
- In the mid current density region $0.2 < j < 1.2$ where ohmic resistance is the dominant contribution to the cell's polarization, the cell design without flow channels performed significantly better than the conventional cell design. The better performance of the design without flow channels is attributed to the compact nature of the cell design, which facilitates more effective and homogeneous distribution of the compression pressure across the active area.
- At high current densities however, for $1.2 < j < 1.6$ a steady increase in the voltage loss is observed for the cell design without channels until at $j = 1.6$ when both cell perform the same again. As current density increases, the overpotential in the cell without flow channels continued to increase and from $1.6 < j < 2$, the cell without flow channels performed significantly worse.

It is known that at high current densities, the performance of a water electrolysis cell is mass transport controlled. This observation therefore suggested that, mass transport overpotential is stronger in the design without flow channels than in the conventional cell design. However, since the polarization curves were not measured under controlled

conditions of feed water flowrate and PTL microstructure, observations could not be completely conclusive.

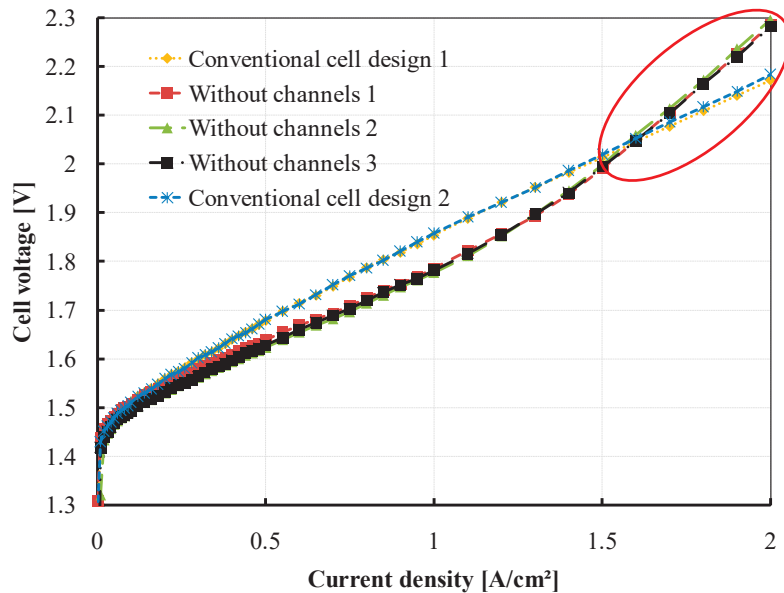


Figure 15: Experimentally measured polarisation curves comparing the performance of the cell concept with flow channels and that without flow channels, both with 25 cm² active cell area and the same MEA and operating at 80 °C and 1 bar

Nevertheless, one could tell that, in spite of the advantages that the design without flow channels has over the conventional design (facile and compact assembling and cost reduction), the mass transport regime and its effect on the performance especially at high current density (up to 5 A/cm²) using state-of-the-art cell components have not been fully understood [54]. Whereas in the conventional design, the machined grooves serve to facilitate the supply of water and removal of gases from the cell by a Navier-Stokes free flow mechanism, in the design without flow channels, these functions are performed by the 3-D PTL alone. It therefore, becomes imperative to optimize the PTL as well as the operating conditions and cell design, especially for operations at high current densities where mass transport becomes the limiting factor in the cell performance.

Thus, the main objectives of this work are:

1. To understand the mass transport regime in the cell design without flow channels and its effect on the cell performance.

2. To understand the evolution and the mitigation of mass transport overpotentials.
3. To understand the effects of operating conditions (temperature, pressure, feed water flowrate), design parameters (PTL thickness, channel geometry) and microstructure properties of the PTL (porosity, mean pore size) on the performance of each cell design concept.
4. And finally, to determine the best operating condition and design and PTL microstructure parameters for which the cell design without flow channels will operate at least as good as the conventional cell design.

Meeting these objectives will make it possible to harness the cost reduction advantages that are presented by the design concept without flow channels without having to make a trade-off with performance losses at high current densities. The scientific methods used to attain these objectives are described next.

2.2 Methodology

The methods that have been used to meet the objectives of this work is summarised in Figure 16. Both modelling and experimental techniques have been developed and implemented.

In the first part, two semi-empirical non-isothermal 2-D coupled momentum, heat and mass transport models for predicting the performance of a proton exchange membrane electrolysis cells 1) operating with flow channels in a conventional design and 2) operating without flow channels will be developed. In the model building, a new approach to predict the cell performance at high current density will be developed by a set of semi-empirical equations that will capture the volume of the gas phase and the effects of micro-bubbles coverage of the electrochemical surface area (ECSA).

In the experimental part, a single 25 cm² active area hybrid test cell which can operate either in a conventional design with flow channels or without flow channels will be designed and constructed. The cell will be used to measure in-situ polarisation curves up to 5 A/cm² in each of the cell set-up at different operating conditions of temperature, pressure and feed water flowrate. The polarisation curves will be measured in an in-house constructed semi-automatic 1 kW test station. The microstructure properties of the PTLs used in the test cell will be experimentally determined ex-situ using the capillary flow porometry technique.

The model will be validated by comparing the measured polarization curves with those predicted by the model. The validated model will then be used as a tool to analyse and compare the performance of each cell design in terms of operating conditions (temperature, pressure, water flowrate), design conditions (PTL thickness, channel width and height) and PTL microstructure (pore mean diameter, porosity), especially at high current densities where mass transport is critical to cell performance. Ultimately, a recommendation will be made for the best operating condition and design and PTL parameters for which the cell design without flow channels will perform at least as good as the conventional design with flow channels.

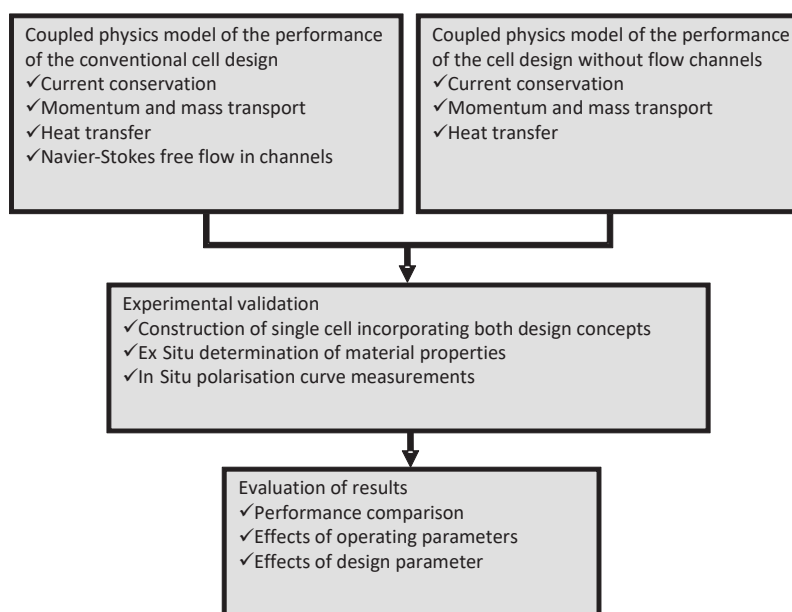


Figure 16: Research methodology

Chapter 3

Literature Review

In this chapter, the state of the scientific knowledge in PEM water electrolysis concerning the topics which are central to this research (cell and stack design, PTLs, characterization tools and modelling approach) will be discussed. The goal is to briefly summarize the research work that has been done relevant to the subject and to identify existing challenges.

3.1 PEM electrolysis cell and stack development

The challenge of cell and stack development is in the adaptation of low cost designs and materials to high voltage efficiency and current density operation. The requirements and targets for cost effective cell design, components and performance balance for commercial applications is being continually reviewed [55]. Strategies for cell/stack costs reduction includes; part count reduction, improved large scale manufacturing techniques, development of cheaper materials, and the simplification of cell structures and the number of cells. There is very little data available in the literature about cell/stack design and components for commercial electrolyzers, since most companies have developed proprietary designs and components for their products. Table 6 summarizes some of the major players in the development of PEM electrolysis stacks over the years.

Table 6: Summary of some major players in stack development

	General Electric 1980	Hydrogenics 2005	Giner Electrochemical Systems 2008	Proton OnSite 2010	ArevaH2Gen 2010
Active area	2323 cm ²	90 cm ²	160 cm ²	550 cm ²	250 cm ²
Pressure	1 – 35 bar	1 – 7 bar	1 – 82 bar	1 – 30 bar	1 – 50 bar
Temperature	up to 80 °C	up to 80 °C	up to 80 °C	up to 50 °C	up to 85 °C
Number of cells	60	15	28	65	12
H ₂ Production	60 m ³ /h	1 Nm ³ /h	0.25 kg/h	55 kg/d	1 Nm ³ /h
Purpose	Prototype	Commercial	Commercial	Commercial	R&D
Source	[56,57]	[36]	[58]	[59,60]	[61]

3.2 Porous Transport Layers (PTLs)

In order to properly perform the functions for which it is intended, current collectors (PTL) must have to exhibit very good mechanical, electrical, mass transport and surface qualities. Research methods for analyzing the surface and mass transport concerns in PTLs such as the spatially resolved contact resistance approach [62] and the fractal geometry approach [63] that have been developed for PEM fuel cells can also be used for PEM electrolyzers.

Generally, attempts at using carbon based materials as used in PEM fuel cells for the electrolysis application has not been encouraging, especially on the anode side. Due to low pH < 2 and high voltage, usually > 2, carbon based materials will become susceptible to electrochemical corrosion when used on the anode side of PEM water electrolyzers. The dissolved ions from corrosion may decrease the proton conductivity of the membrane and may

lead to permanent degradation [64]. For this reason, state-of-the-art PTLs for PEM water electrolysis are usually made from highly electrochemically stable metals. The use of metals comes as well with some concerns, especially on the cathode side. It is well known that, when metals are exposed to hydrogen for a long time, especially at elevated pressures, the metal begins to lose its structural properties and becomes more brittle. This issue, known as hydrogen embrittlement may compromise the stability, durability and reliability of the PTL and thus the cell. However, it has been proven [65] that titanium has a strong resistance against hydrogen embrittlement and some authors also suggested tantalum, niobium and zirconium, in descending order of preference as other metals that can be used as PTL on the cathode half cell. Other authors [66] have demonstrated that the issue of embrittlement can be completely resolved by gold coating, although this solution is not practically favourable due to high costs. Titanium has therefore established itself as the state-of-the-art base material for PTLs used in PEM water electrolysis [67].

There are basically two major types of titanium based PTLs that are in use today. The use of a low cost expanded titanium mesh type has successfully been demonstrated with acceptable cell performance [68]. In spite of the advantages of this cheap option, the large fibre diameter of such mesh $> 100 \mu\text{m}$ may pose a threat to the mechanical structure and stability of the MEA. And the large pore size, usually $> 150 \mu\text{m}$ may increase ohmic loss due to flow of electrons through the PTL and reduce the electro-kinetics due to poor contact between the PTL and the MEA. The sintered titanium powder is a well established option that is being widely used in PEM electrolyzers. It is made by the thermal sintering of titanium powder while controlling the temperature, pressure and the powder grain size; to adjust the rigidity, porosity and pore size of the PTL [69] and [70]. The only disadvantage of this solution is its high cost.

Table 7: Properties of a typical sintered titanium PTL [71]

Thickness	0.8 – 2 mm
Porosity	20 – 50 %
Pore size	5 – 30 μm
Powder size	25 – 250 μm
Gas permeability	$1 \times 10^{-13} - 1 \times 10^{-12} \text{ m}^2$
Specific area resistance	5 – 10 $\text{m}\Omega\text{cm}$

Using a sintered titanium PTL, [71] determined that the microstructure of the PTL can have a significant role on the cell performance and concluded that, an un-optimized PTL microstructure can increase the cell voltage by up to 100 mV at 2 A/cm². However, the authors could not determine the source of the losses, whether it was due to activation, ohmic or mass transport losses. Also, the effect of different microstructural properties could not be successfully isolated from that work. Table 7 summarizes the properties of a typical sintered titanium PTL.

Other authors [72] have reported on an interfacial contact resistance between the bipolar plate and the PTL as a major source of performance losses and suggested the application of micro-porous layers between adjacent cell components to improve on the contact and to mitigate the interfacial contact losses.

3.3 In Situ characterization techniques for PEM electrolysis cells

In Situ characterization techniques are the tools and methods that can be used to qualify and quantify the main physical and phenomenological properties of the cell and/or individual cell components inside the compact cell environment.

The relationship between the cell voltage and current density across the cell represents the main and most widely used characteristic tool of a PEM electrolysis cell and it is the so-called polarization curve or I-V curve, best measured at constant operating conditions of temperature, pressure and feed water flowrate. The polarization curve performs a ramping up of the reversible cell voltage and all the irreversible overpotentials against operating current density, and it is most reliable when isothermal and stationary conditions are met. Testing protocols for polarization curve generation are normally advised by the MEA manufacturer, although this can be adapted to specific needs of the investigation. While the polarization curve is the summation of all the losses, it is also very important to be able to isolate and quantify the individual loss mechanisms within the cell and, there are a few electrochemical techniques designed to do that.

The internal reference electrode method can be used to separate and quantify the individual contributions of the OER and the HER electro-catalyst kinetics (anode and cathode overpotentials respectively) to the overall activation overpotential imposed on the cell. This technique has been widely used as a development and testing tool for electro-catalysts in fuel cell [73–77] and has also been adapted and extensively used in PEM water electrolysis applications [78–80]. Millet [81] employed this method in PEM water electrolysis to determine the electric potential distribution inside a Nafion membrane. Gerteisen [82] has reported a means of realising this method in a PEM fuel cell by laser ablating the MEA and, this can also be applied to the PEM water electrolysis cell as well.

The roughness factors of the anode and cathode electrodes as well as the catalyst loadings are important parameters that affect the rate of the electrochemical reaction in PEM water electrolysis and cyclic voltammetry is a tool that can be used to quantify them [83]. This technique was used by Savinell [84] to determine the roughness factor of unsupported IrO₂ catalyst to be in the range of 700 – 800, depending on the morphology, loading and layer

thickness. Marshall [85] also used cyclic voltammetry to separate the effects of specific electrolytic activity and the active surface in a PEM electrolysis cell, while Rozain [86] recently used the tool to study the influence of IrO₂ loading on the anode of a PEM electrolysis cell.

The electrochemical impedance spectroscopy is a tool that goes further, to isolate and quantify the three major overpotential mechanisms, activation, ohmic and mass transport overpotentials. Rasten [87] has used this method to study electro-catalyst performances in PEM water electrolysis. Rozain [88] used it to reveal that micro-sized titanium particles added to the anode catalyst layer can indeed lead to a reduction in the ohmic resistance of the OER electrode. Meanwhile, Dedigama [89] used the electrochemical impedance spectroscopy to study the effect of mass transport in a PEM water electrolysis cell and determined that, the major source of mass transport limitation (overpotential) is related to the slug flow pattern of bubbles in the flow channels.

While the electrochemical impedance spectroscopy method is vital for the quantification of mass transport losses, it cannot be used to physically observe and study flow patterns, bubbles nucleation and the evolution of the two-phase flow mechanism in the cell and its contribution to cell performance. These can be realized by the flow visualization technique, which uses optically transparent cell hardware and a series of high speed cameras to study the flow pattern and bubble dynamics inside the cell. This technique is quite established in PEM fuel cells, [90–92,92–94]; although it has not been extensively exploited in PEM water electrolysis. Tanaka [95] has used this method to study the 2-phase flow in a PEM electrolysis cell with electrolyte concentrations, and concluded that, the number of bubbles and the degree of bubbles coalescence increases with increasing current density. However, the effect on the mass transport overpotential was not quantified. Dedigama [96] used this method coupled with thermal imaging and electrochemical impedance spectroscopy to characterize the effects of flow on mass transport limitation. Selamet [97] also used the visualization method to study the

2-phase transport in a PEM water electrolysis cell. They identified two different patterns of gas bubble evolution and departure on the PTL|catalyst layer interface. They also found that, the operating temperature affects the water content in the cell and that, increasing the temperature increases the gas volume and decreases the water content in the anode chamber. However, a co-relation between these findings and mass transport overpotentials and cell polarization could not be made.

In spite of all the characterization techniques available, modelling appears to be the most cost and time effective. It is a robust and an all inclusive tool that can serve the purpose of performance characterization, performance engineering, aid in the design and up-scaling efforts and give deeper meaning and understanding to the physical mechanisms, especially when it is validated with its own experimental data.

3.4 PEM electrolysis modelling

Many aspects of PEM electrolysis modelling are adapted from PEM fuel cell modelling, which is a more advanced and explored field [92,98–105]. Modelling in PEM water electrolysis is still in its budding phase. While activities in PEM fuel cell modelling dates as far back as the late 1980's, some of the pioneering PEM water electrolysis models were only reported as late as in the early 2000's, notably [106] and [107]. The scarcity of comprehensive PEM electrolysis modelling works in the literature is therefore, not surprising Figure 17.

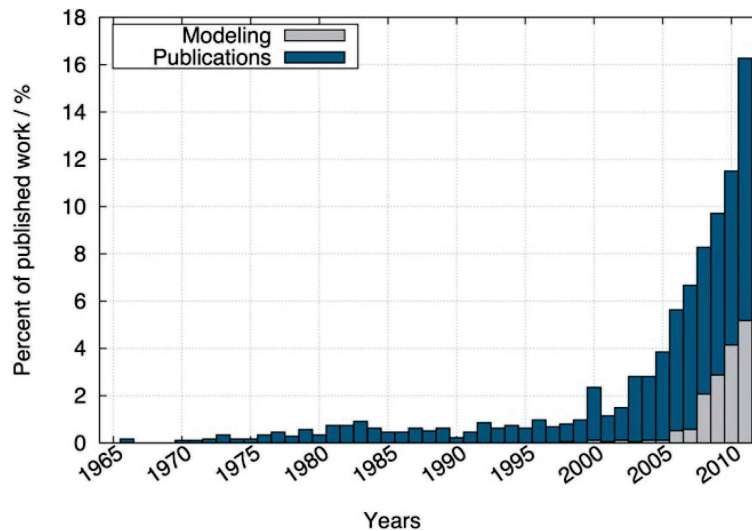


Figure 17: Number of publications as a percentage of total publications directly related to PEM water electrolysis over the years, including those related specifically to PEM electrolysis modelling [33].

The early modelling approaches of PEM water electrolysis were mostly 0 to 1 dimensional steady state isothermal approximation of polarization curves. These generally only accounted for the Butler-Volmer electrode kinetics and the ohmic resistance in the PEM, while neglecting the mass transport mechanisms and their effects. This explains why model accuracies were reported only for current densities up to 1 A/cm² at most, before the dominance of mass transport limitation could set in [107–111].

Later generation of PEM water electrolysis modelling was pioneered by Marangio [112], who included the effect of mass transport in his 2-D model which predicted cell polarization curves up to 2 A/cm² operating current density. However, the consideration of mass transport effect was based fully on the theoretical Nernstian approach, which assumes that mass transport limitation is purely diffusion driven. In this diffusion driven approach, the gas phase is not taken into account and mass transport limitation is assumed to arise only from the dissolved species. While this approach is computationally efficient, it can only be valid in the low to mid current density range, 0 – 2 A/cm². At higher current densities, this diffusion driven approach will be found wanting as the increasing evolution of the gas phase will tend to pose further challenges to the kinetics of the water splitting reaction.

It is only until recently that the model of Fritz [25] took the effect of the gas phase into consideration. However, in his 1-D isothermal model, the spatial distribution of the dissolved gasses was not considered and the total volume of the gas phase, the bubble size and bubble coverage was not taken into account. Also, the important topic of heat and water management was not addressed, which makes the model not very suitable as a tool for initial design and up-scaling purposes. Furthermore, the model was limited to operations up to 3 A/cm², which falls way short of the need for industrial hydrogen production by PEM water electrolysis in the near future.

The 2-D non-isothermal models presented in this work stand out in the development of semi-empirical equations to predict the gas phase volume and bubble size, which is then used to quantify the bubble coverage and overpotentials imposed by the gas phase for current densities up to 5 A/cm². Furthermore, the fully-coupled physics approach incorporating thermodynamic, electrochemical, thermal and fluidic sub-models makes them possible to be able to address heat and water management issues, thus suitable as design and up-scaling tool. Also importantly, this work is the first in which the two different cell design concepts have been compared and more so, by using a model based approach, to address the trade-off bottleneck of cell cost versus performance in PEM water electrolysis.

Chapter 4

Model Development

This chapter presents the development of 2 different (one for the conventional cell design concept with flow channels and the other for the cell design concept without flow channels) semi-empirical fully coupled 2-D non-isothermal models for predicting the cell polarisation curves.

In the first part, an equation for modelling the reversible cell voltage based on the well known Nernst equation will be derived. This will be followed by the development of semi-empirical equations for modelling all the sources of overpotentials (activation, membrane and ohmic, diffusion and bubble overpotentials) that have been considered in this work. Based on these, the model equation for the cell polarisation will be defined.

In the second part, the governing equations for describing all the physical phenomena within the cell (current conservation, heat transfer and momentum and mass transport) will be developed. Based on the partial differential equations, solving of the spatial distribution of their defining quantities (temperature, flow velocity and species concentration) will be made possible.

All the governing and semi-empirical equations are valid for both models, except the Navier-Stokes equation which is used only for modelling the free flow momentum transport in the channels of the conventional cell design and then inter-coupled with the mass transport in the PTL.

In the final section of this chapter the interaction (coupling methodology) between all the physical phenomena (sub-models) and also with the derived semi-empirical equations for modelling the overpotentials will be shown, as well as their implementation in COMSOL Multiphysics® v.4.2 and the numerical solution strategy. The assumptions made on the development of the models and their implications on the strengths and weaknesses of the models as well as performance predictions will conclude this chapter.

4.1 Reversible Cell Voltage and Irreversible Losses

In this section, the methods and equations which have been used for describing the reversible cell potential and the individual irreversible losses; activation, ohmic, diffusion and mass transport overpotentials will be presented.

4.1.1 Thermodynamic consideration

The voltage of the electrolysis cell operating at reversible conditions, also known as the reversible cell voltage can be expressed similar to Eq. 6 as:

$$E_{rev}(T, p) = -\frac{\Delta G(T, p)}{nF} \quad \text{Eq. 20}$$

Expressing the change in Gibbs free energy ΔG in terms of enthalpy and entropy changes, Eq. 20 can be written as:

$$E_{rev}(T, p) = \frac{\Delta H(T, p)}{nF} - \frac{T\Delta S(T, p)}{nF} \quad \text{Eq. 21}$$

For low temperature applications like PEM water electrolysis, in the absence of an external heat source, all the required energy is supplied by electrical work and the term $\frac{\Delta H}{nF}$ is called the thermo-neutral voltage E_{th} , which at standard conditions (25 °C and 1 atm) is 1.481 V vs. SHE using a ΔH value of 285.8 kJ/mol. The cell potential based on the enthalpy alone (i.e., 1.481 V) is the potential in the absence of entropic losses, which are irreversible in nature. To account

for the unavoidable losses, the entropic term ($\frac{T\Delta S(T,p)}{nF}$) in Eq. 21 is considered for temperature and pressure variations, in order to obtain E_{rev} . To account for the temperature variations of the thermo-neutral potential, the empirical relationship from [113,114] was adopted, which is valid for temperatures up to 100 °C [115]:

$$E_{th}(T) = 1.481 - 0.9 \times 10^{-3} \cdot (T - 298) \quad \text{Eq. 22}$$

To evaluate the temperature dependence of the thermal fraction of the $\Delta G, T\Delta S(T,p)$, equilibrium data reported by [116] have been linearized, Figure 18, to obtain:

$$\frac{T\Delta S(T)}{nF} = 9.9683 + 0.13111 \cdot T \quad \text{Eq. 23}$$

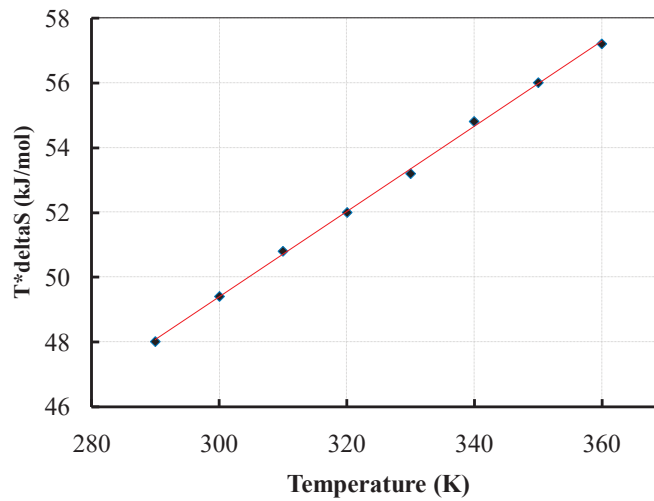


Figure 18: Linearized dependency of the entropy component on temperature [116]

The pressure dependency of the entropy term is then expressed as derived in Eq. 9 and in the same way it is used in [117] for balanced pressure on the anode and cathode side:

$$\frac{T\Delta S(p)}{nF} = \frac{-RT}{nF} \cdot \ln\left(\frac{1}{p^{0.5}}\right) \quad \text{Eq. 24}$$

Putting Eq. 20 through to Eq. 24 together, an expression for the temperature and pressure dependency of the reversible cell potential is derived:

$$E_{rev}(T, p) = 1.481 - 0.9 \cdot 10^{-3} \cdot (T - 298) - \frac{9.9683 - 0.1311 \cdot T}{nF} + \frac{RT}{nF} \cdot \ln\left(\frac{1}{p^{0.5}}\right) \quad \text{Eq. 25}$$

When an electrode is disturbed from its thermodynamic equilibrium (reversible cell voltage), the induced irreversible losses leads to a decrease (galvanic cell) or an increase (electrolytic cell) in the cell potential. With the equation for calculating the reversible cell voltage known, next will be to derive semi-empirical equations to model the contribution of all the irreversible losses to the cell polarisation.

4.1.2 Kinetics losses

The kinetic losses which dominate at low current densities are dependent on the electrode material properties and represent the energy required to overcome the activation barrier of the electrochemical reaction which occurs on the electrode-electrolyte interface. The kinetic losses are therefore also referred to as the activation overpotential.

At very low current densities (usually $\ll 0.1$ A/cm²), where ohmic and transport limitations are negligible, the current density and potential relationship at the electrodes can be described by the well-known Butler-Volmer charge transfer reaction equation [109], which is analogous to Eq. 14:

$$j = j_o \left[\exp\left(\frac{\alpha_1 n F \eta_{act}}{RT}\right) - \exp\left(\frac{-\alpha_2 n F \eta_{act}}{RT}\right) \right] \quad \text{Eq. 26}$$

Assuming that the charge transfer coefficients α_1 and α_2 for the forward and reverse reactions are the same [118,119], Eq. 26 can then be expressed in terms of the activation overpotential:

$$\eta_{act} = \frac{RT}{\alpha F} \sinh^{-1}\left(\frac{j}{n j_o}\right) \quad \text{Eq. 27}$$

Eq. 27 can then be separately applied to the anode and cathode half reactions:

$$\eta_{act,an} = \frac{RT}{\alpha_{an} F} \sinh^{-1}\left(\frac{j}{n_{an} j_{o,an}}\right) \quad \text{Eq. 28}$$

$$\eta_{act,cat} = \frac{RT}{\alpha_{cat}F} \sinh^{-1} \left(\frac{j}{n_{cat}j_{o,cat}} \right) \quad \text{Eq. 29}$$

The exchange current density, j_o , is an intrinsic property of the electrocatalyst and determines the rate of the electrochemical reaction at equilibrium. It depends on the atomic structure of the surface layers (e.g., composition, arrangement and size of the catalyst grains) and could vary for the type and source of the catalyst used. It is often best to be experimentally determined at a reference temperature, $j_{o,ref,an;cat}$. Using the Arrhenius relationship and the activation energy of the reaction, E_a , one can express the exchange current density at any other temperature by:

$$j_{o,an;cat} = j_{o,ref,an;cat} \cdot S_{eff} \cdot \exp \left(\frac{E_{a,an;cat}}{R} \cdot \left(\frac{1}{T} - \frac{1}{T_{ref,an;cat}} \right) \right) \quad \text{Eq. 30}$$

Where, S_{eff} is the product of the electrode catalyst loading and the catalyst specific surface area. Table 10 summarizes the electrokinetic parameters for the Pt-based cathode and the Ir/IrO₂-based anode electrodes used in this work.

4.1.3 Ohmic losses

The ohmic losses originate from three separate sources: 1) the electrical resistance of the cell components, where electrons flow, 2) the ionic resistances of the membrane and ionomer, where protons flow and 3) interfacial contact resistance due to the resistance to the flow of electrons between adjacent cell components. The electrical contact resistances at different cell components interfaces are not considered in this work.

At steady-state operation, the divergence of protonic current through the membrane is zero, and the protonic current is proportional to the gradient of the potential field which is given by:

$$\frac{dj}{dz} = 0 \text{ and } j = -\sigma_{mem} \frac{d\phi}{dz} \quad \text{Eq. 31}$$

Where, φ is the membrane potential, σ_{mem} is the proton conductivity of the membrane and z is in the direction of the thickness of the membrane, see Figure 23.

Integrating Eq. 31 over the membrane thickness, d_{mem} , leads to the following expression for the overpotential due to the protonic transport through the membrane:

$$\eta_{mem} = \frac{d_{mem}}{\sigma_{mem}} j \quad \text{Eq. 32}$$

The proton conductivity of the membrane is directly related to the degree of membrane hydration and the operating temperature. The proton conductivity of the Nafion® membrane has been extensively studied for PEM fuel cells and it can be empirically expressed in terms of the membrane hydration and temperature by [120]:

$$\sigma_{mem} = (0.005139\lambda - 0.00326) \exp\left(1268\left(\frac{1}{303} - \frac{1}{T}\right)\right) \quad \text{Eq. 33}$$

The membrane humidification, λ , which is a measure of water molecules per sulfonic groups, ranges from 14 to 25. Membrane humidification could be highly variable in low temperature PEM fuel cells; hence, becomes a critical parameter when determining the performance of a PEM fuel cell. However, in the case of PEM water electrolysis cell, where water is the main transport medium, the membrane is assumed to be always fully hydrated, i.e. $\lambda \approx 24$. For this reason, a hydration value of $\lambda = 24$ was used in this work. This choice of hydration led to the closest agreement of the model with the experimental data.

The ohmic overpotential due to electron transport through the PTL is expressed using Ohm's law:

$$\eta_{elect} = \frac{d_{PTL}}{\sigma_{PTL}} j \quad \text{Eq. 34}$$

Where, σ_{PTL} and d_{PTL} are respectively, the conductivity and thickness of the porous transport layer. The bipolar plates are flat and solid sheets of highly conductive titanium grade 2 and it is assumed that electron flow through it is infinitely fast. For this reason, ohmic resistance of

the bipolar plates was not considered. The effective electrical conductivity of the PTL was obtained from a Bruggeman-based formulation [121] which considers the void fraction of the PTL. The total potential loss due to ohmic losses then becomes the sum of the two ohmic overpotentials:

$$\eta_{ohm} = \eta_{mem} + \eta_{elect}$$

Eq. 35

4.1.4 Mass transport losses

When the water splitting reaction is mass transport controlled, the rate of reactant water supply and removal of produced gasses from the active sites of the catalyst layer interface determine the overall reaction rate. In most published works, the mass transport limitation has been treated purely as a diffusion controlled phenomenon, whereby, only the concentration and transport of gasses in dissolved phase are considered [122]. This can only be valid at very low current densities, in the mA/cm² range, because at higher current densities, when saturation of the electrolyte with the evolved gases is reached, the formation of the gas phase poses further limitations to the water splitting reaction rate. In particular, oxygen nano-bubbles evolved on the anode electrode at higher current densities ($\gtrsim 0.1 A/cm^2$) tend to shield the active sites of the catalyst layer, thereby, reducing the electrochemical surface area and catalyst utilization. The mass transport losses due to dissolved species and the surface shielding by the gas phase have been evaluated separately.

The slow removal of dissolved gasses from the PTL|catalyst layer interface is the source of a diffusion overpotential derived from the transport barrier, which is caused by the PTL structure. The approach of [25,108] is adopted to model this diffusion overpotential and the Nernst equation is applied for each half cell separately:

$$\eta_{diff,an} = \frac{RT}{n_{an}F} \ln \left(\frac{C_{O_2,mem}}{C_{O_2,ref}} \right) \quad \text{Eq. 36}$$

$$\eta_{diff,cat} = \frac{RT}{n_{cat}F} \ln \left(\frac{C_{H_2,mem}}{C_{H_2,ref}} \right) \quad \text{Eq. 37}$$

Where $C_{O_2,mem}$ and $C_{H_2,mem}$ are the concentration of dissolved oxygen and hydrogen at the anode and cathode MEA interfaces respectively; and $C_{O_2,ref}$ and $C_{H_2,ref}$ are the concentration of dissolved oxygen and hydrogen at a reference position in the cell, respectively. Here, the reference position is taken at the PTL|BiP interface, thereby, describing the diffusion overpotential as a function of the concentration gradient of the dissolved species across the PTL. The determination of the species molar concentrations is presented in Section 4.2.3

The diffusion overpotentials expressed by Eq. 36 and Eq. 37 can be directly applicable and solely dependable in PEM fuel cells to address the mass transport limitations. In PEM electrolysis cells, however, with water being the dominant flow medium, the effect of this diffusion overpotential becomes significant only at low current densities (\sim mA range), i.e., when the cell is operating at extreme conditions of very low water flowrates.

As the current density increases, the gas production increases according to Faraday's law. The electrolysis water eventually reaches supersaturation and the gas phase starts to form nano-bubbles. This leads to another form of mass transport limitation which hereafter is referred to as the bubble overpotential. The total mass transport related losses here, ($\eta_{mass\ trans}$), are expressed by a sum of the diffusion (Eq. 36 and Eq. 37) and bubble overpotentials.

An expression for the bubble overpotential can be derived from the Butler-Volmer equation, Eq. 26. Because the mass transport limitation is more significant on the anode side, where the water splitting reaction occurs, only the Butler-Volmer expression of the anode electrode for the bubble formation is considered:

$$j = j_{lim} \left[\exp\left(\frac{\alpha n_{an} F \eta_{an}}{RT}\right) - \exp\left(\frac{-\alpha n_{an} F \eta_{an}}{RT}\right) \right] \quad \text{Eq. 38}$$

Where j_{lim} is the limiting current density due to the combined effects of bubble coverage and water starvation at high current densities ($>3 \text{ A/cm}^2$). This expression of current density is mathematically analogous to the exchange current density in Eq. 26, where reaction is under kinetic control. At very high current densities, $>3 \text{ A/cm}^2$, the OER mechanism is negligible, so the second term of Eq. 38 can be dropped and the relationship between the current density and the bubble overpotential can be expressed as:

$$\eta_{bubble,an} = \frac{RT}{\alpha_{an} F n_{an}} \ln\left(\frac{j}{j_{lim}}\right) \quad \text{Eq. 39}$$

Wurthrich et al. [123] have proposed the following relationship for j_{lim} as a function of the bubbles coverage, θ :

$$j_{lim} = j(1 - \theta) \quad \text{Eq. 40}$$

Where, $0 \leq \theta \leq 1$. When $\theta = 0$, current passes through the cell; when $\theta = 1$, the PTL|catalyst layer interface is completely shielded by gas bubbles, Figure 19.

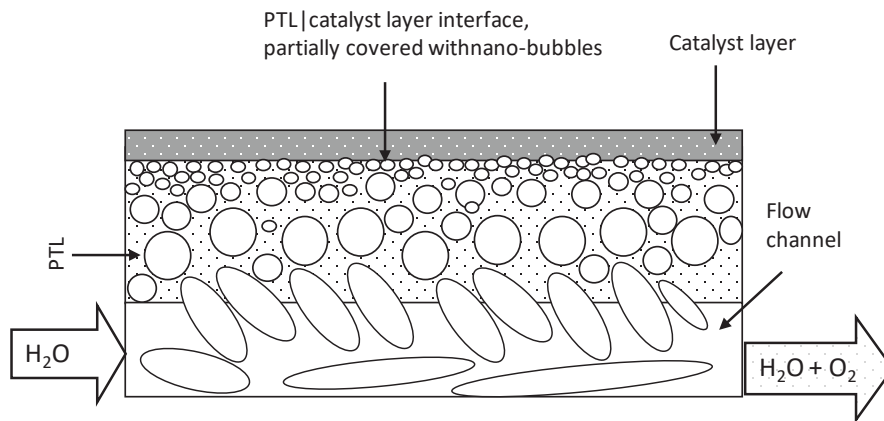


Figure 19: Bubble distribution and surface shielding in the anode half cell of the design with flow channels

Putting Eq. 39 and Eq. 40 together yields:

$$\eta_{bubble,an} = \frac{RT}{\alpha_{an} F n_{an}} \ln\left(\frac{1}{1 - \theta}\right) \quad \text{Eq. 41}$$

However, [17] has shown that the cell potential increases exponentially at the mass transport controlled region. Thus to capture this exponential behaviour, the bubbles' overpotential is expressed as:

$$\eta_{bubble,an} = \frac{RT}{\alpha_{an}Fn_{an}} \left(\frac{1}{1-\theta} \right)^2 \quad \text{Eq. 42}$$

Eq. 42 is an empirical modification of Eq. 41 which allows one to simulate the exponential behaviour of the mass transport region for water electrolysers. Here, θ is defined as the sum of the Pore-to-bubble-ratio (PBR) and the water starvation ratio ζ . It is assumed that the pores of the PTL are cylindrical and continuous. Furthermore, the oxygen nano-bubbles are considered spherical in shape and a simple relationship for the pore-to-bubble ratio, r_{pb} is derived:

$$r_{pb} = \frac{4 * d_{bubble}^2}{d_{pore}^2} \quad \text{Eq. 43}$$

Assuming that the oxygen molecules in the nano-bubbles behave as an ideal gas, the total volume of the gas phase at the PTL|catalyst layer interface can provide a good approximation of the critical bubble size (d_{bubble}):

$$d_{bubble} = \frac{1}{nucleation\ sites} * \left(\frac{\frac{6RT}{p_g} * \int_{0,water\ inlet}^L (C_{o2} - C_{sat}) dx}{\pi} \right)^{1/3} \quad \text{Eq. 44}$$

Where, C_{sat} is the saturation concentration of dissolved oxygen and can be calculated from Henry's law, Eq. 45, and L is the geometrical length of the cell from water inlet to outlet. In PEM water electrolysis, nucleates can form best at cracks, surface imperfections and pores. Since it was not possible to reliably determine the number of such sites, the number of nucleation sites was treated as a fitting parameter with the experimental data.

$$C_{i,sat} = \frac{p_i}{K_{Henry,i}} \quad \text{Eq. 45}$$

The water starvation is defined as the ratio of the water supply rate to the gas production rate at the PTL|catalyst layer interface:

$$\zeta = \frac{\dot{V}_{h_2o,PTL/catalyst\ layer}}{\dot{V}(T, P, j)_{o_2,PTL/catalyst\ layer}} \quad \text{Eq. 46}$$

The oxygen production rate $\dot{V}(T, P, j)_{o_2,PTL/catalyst\ layer}$ is proportional to the current density and is calculated by the Faraday's law. The amount of reactant water reaching the active area

$\dot{V}_{h_2o,PTL/catalyst\ layer}$ is solved by the Brinkman equations and is described in Section 4.2.2:

$$\dot{V}_{h_2o,PTL/catalyst\ layer} = w_{active\ area} * \int_{0,water\ inlet}^L u_z dz \quad \text{Eq. 47}$$

Where, u_z is the water flow velocity to the active area and z is the direction in the thickness of the electrode. $w_{active\ area}$ is the out of plane thickness of the catalyst layer, y-direction in Figure 23.

4.1.5 Polarisation curves generation

In a PEM water electrolysis cell, the reversible cell voltage and all the irreversibly losses can electrically be considered as a set of resistors connected in series. Figure 20 shows a schematic representation of the equivalent electrical circuit.

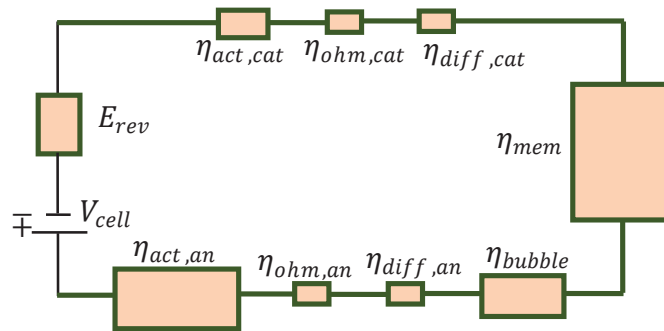


Figure 20: Equivalent electrical circuit of PEM water electrolysis cell. Cell voltage as a sum of the reversible cell voltage and all the overpotentials treated as resistors in series

With the reversible cell voltage and all the overpotentials within the cell evaluated, the cell potential can be expressed as the sum of the equilibrium potential and all the individual overpotentials associated with irreversible losses described in Section 4. The operating cell voltage, V_{cell} , or cell polarisation can then be calculated from:

$$V_{cell} = E_{rev} + \eta_{act,an} + \eta_{act,cat} + \eta_{ohm} + \eta_{diff,an} + \eta_{diff,cat} + \eta_{bubble,an} \quad \text{Eq. 48}$$

4.2 Governing equations

In this section, the governing equations for developing the multiphysics models and the methods employed to solve for the unknown variables (C_i, u_z, p_i, T) to be fed into the semi-empirical equations derived in Section 4 will be described. Figure 23 shows the model domains and boundaries, which spans a 2-D cross section of the electrolysis cell from the anode bipolar plate to the cathode bipolar plate in the z-axis direction and from the water inlet to water and gas outlet in the x-axis direction. The models developed consist of three finite element sub models which describe the physical phenomena 1) current conservation 2) momentum transport 3) mass transport and 4) heat transfer.

4.2.1 Current conservation sub-model

The BiP, PTL and electrodes are very thin and are made from highly conducting materials (such as Titanium grade 2, platinum and iridium) so transport of electrons is very fast and it is assumed that the current distribution is homogeneous in all directions. Therefore, the spatial distributions of electrical and ionic currents are not considered. The effective conductivity of the PTL was calculated by using the Bruggeman correction which considers the porosity of the PTL (ε_{PTL}) [121]:

$$\sigma_{eff,PTL} = \sigma_{Ti} * (1 - \varepsilon_{PTL})^{1.5} \quad \text{Eq. 49}$$

4.2.2 Momentum transport sub-model

In PEM water electrolysis, water is the main transport medium and momentum transport is based primarily on water flow. To model the velocity and pressure fields in the porous media (PTL and catalyst layer), the Brinkmann equation, which is an extension of Darcy's law of fluid flow through a porous medium and takes the viscous effects into consideration, has been used. While momentum transport in the flow channels (relevant only for the conventional design concept) was modelled according to the Navier-Stokes free fluid flow model.

Water flow through the PTL and the catalyst layer was modelled (Brinkmann model) by Eq. 50 and Eq. 51 which represents the momentum balance and continuity, respectively:

$$\frac{\partial \varepsilon_{PTL} \rho_{H_2O}}{\partial t} + \nabla \cdot (\rho_{H_2O} u) = 0 \quad \text{Eq. 50}$$

$$\rho_{H_2O} \nabla u = \dot{Q}_{H_2O} \quad \text{Eq. 51}$$

The source term, \dot{Q}_{H_2O} , is calculated from the water balance at the PTL|catalyst layer interface and considers the water splitting and electro-osmotic drag contributions. The water and species balance within the cell is shown in Figure 21.

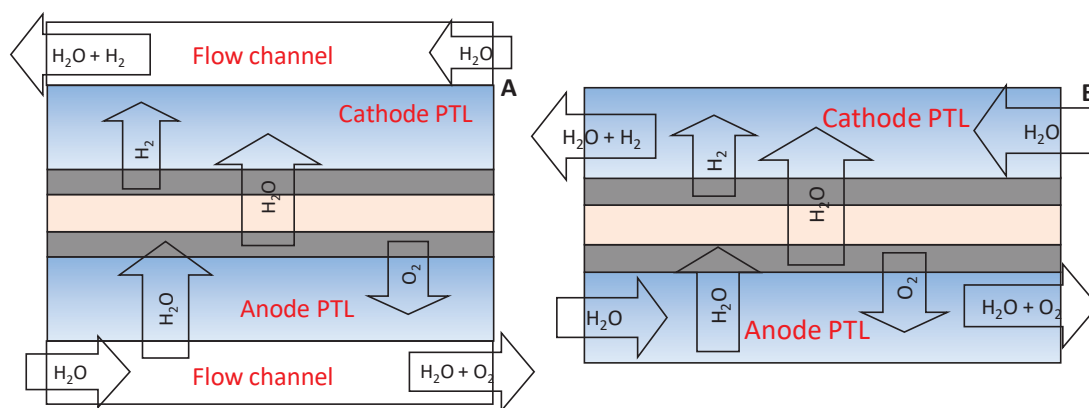


Figure 21: Momentum and mass transport inside the cell A) Conventional cell design concept, B) Cell design concept without flow channels "advanced design"

The water supply by electro-osmotic drag (at cathode) and water consumption by electrolysis and electro-osmotic drag (at anode) are calculated using Eq. 52 and Eq. 53 for the cathode and anode half cells, respectively:

$$\dot{Q}_{H_2O,cat} = \frac{j * M_{H_2O} * \delta}{n_{an}F} \quad \text{Eq. 52}$$

$$\dot{Q}_{H_2O,an} = -\frac{j * M_{H_2O}}{n_{an}F} (1 + \delta) \quad \text{Eq. 53}$$

Protons migrating across the membrane often pulls water molecules along with them. The number of moles of water pulled across the membrane by a mole of migrating proton is the electro-osmotic drag coefficient δ . Onda [106] has shown that the electro-osmotic drag coefficient is only temperature dependent and expressed the following empirical relationship which was adopted in this work:

$$\delta = 0.03 + 0.013T \quad \text{Eq. 54}$$

Momentum transport through the flow channels (in conventional design only) was modelled by applying the Navier-Stokes equations to solve for the pressure and velocity fields in the flow channels. The vector equation that represents the momentum conservation is given by:

$$\rho(u_{FC} \cdot \nabla u_{FC}) = -\nabla p + \nabla(u_{FC}(\nabla u_{FC} + (\nabla u_{FC})^T) + F_I \quad \text{Eq. 55}$$

Where, u_{FC} is the velocity of water in the flow channels. The left hand side of Eq. 55 represents the inertia forces; the first term on the right hand side represents the pressure forces; the second term on the right hand side stands for the viscous forces and F represents all externally applied forces on the fluid, in this case, $F_I = 0$.

The Navier-Stokes momentum conservation equation is always solved together with the continuity equation which is:

$$\nabla \cdot (\rho u_{FC}) = 0$$

Eq. 56

For incompressible fluids (which is a good approximation for water), the density is assumed to be constant, so, the continuity equation reduces to zero.

4.2.3 Mass transport sub-model

The mass transport mechanisms in the flow channels, PTL and catalyst layers are diffusion and convection controlled processes. Since there are only two species involved in each of the anode and cathode compartments, the diffusion of dissolved gasses can easily be described by Fick's law of diffusion, with the convection term being coupled from the momentum balance. The mass balance equation is modelled by:

$$\frac{\partial C_i}{\partial t} + u \cdot \nabla C_i = \nabla \cdot (D_i \nabla C_i) + \dot{R}_i$$

Eq. 57

The diffusion coefficients, D_i , of dissolved species, i , are calculated by the Maxwell-Stefan binary diffusivity for oxygen and water on the anode side and for hydrogen and water on the cathode half cell, Eq. 58 and Eq. 59 respectively.

$$D_{o_2, h_2o} = \frac{D_B^{1.75}}{p * \left(v_{o_2}^{\frac{1}{3}} + v_{h_2o}^{\frac{1}{3}} \right)^2 * \left(\frac{1}{M_{o_2}} + \frac{1}{M_{h_2o}} \right)^{0.5}}$$

Eq. 58

$$D_{h_2, h_2o} = \frac{D_B^{1.75}}{p * \left(v_{h_2}^{\frac{1}{3}} + v_{h_2o}^{\frac{1}{3}} \right)^2 * \left(\frac{1}{M_{o_2}} + \frac{1}{M_{h_2o}} \right)^{0.5}}$$

Eq. 59

Where, D_B is the binary diffusion coefficient and v_i is the species molar diffusion volume.

The reaction term \dot{R}_i ($\dot{R}_i = 0$ in the PTL) is calculated by Faraday's law for the cathode and anode reactions according to Eq. 60:

$$\dot{R}_i = \frac{j * A}{n_i F M_i} \quad \text{Eq. 60}$$

Where, M_i is the molecular mass of species (H_2 at the cathode and O_2 at the anode) and A is the active cell area.

4.2.4 Heat transfer sub-model

Because the PTL, BiP and catalysts are made from highly conductive materials it is assumed that the transport of electrons is infinitely fast and, the effect of joule heating is ignored. Also, based on the assumption of homogeneous current density distribution, the effects of hot spot formation on the active area are neglected. The thermal sub model solves the spatial temperature distribution in the cell by coupling momentum and mass transport equations with the heat transfer equation:

$$\rho_i C_{p,i} \frac{\partial T}{\partial t} + \rho_i C_{p,i} \mathbf{u} \cdot \nabla T = \nabla \cdot (K_i \nabla T) + \dot{Q}_{el} \quad \text{Eq. 61}$$

The heat capacity, density and thermal conductivities are defined for each species, i , and each sub domain, Ω . The source term, \dot{Q}_{el} , is defined as the heat produced from the electrolysis reaction:

$$\dot{Q}_{el} = j(V_{cell} - E_{th}) \quad \text{Eq. 62}$$

The sub-models are inter-coupled with the semi-empirical equations as shown in Figure 22 with boundary conditions imposed as in Table 8 and Table 9.

4.3 Numerical methods

Spatial 2-D fields of the dependent variables ($p, u, u_{FC}, T, C_{O_2}, C_{H_2}$) are calculated from the governing equations and they serve as input to the semi-empirical equations for the determination of the individual overpotentials. The overpotentials are added up into the cell polarisation and the cell voltage is fed back into the governing equations to form a strongly coupled physics model as shown in Figure 22.

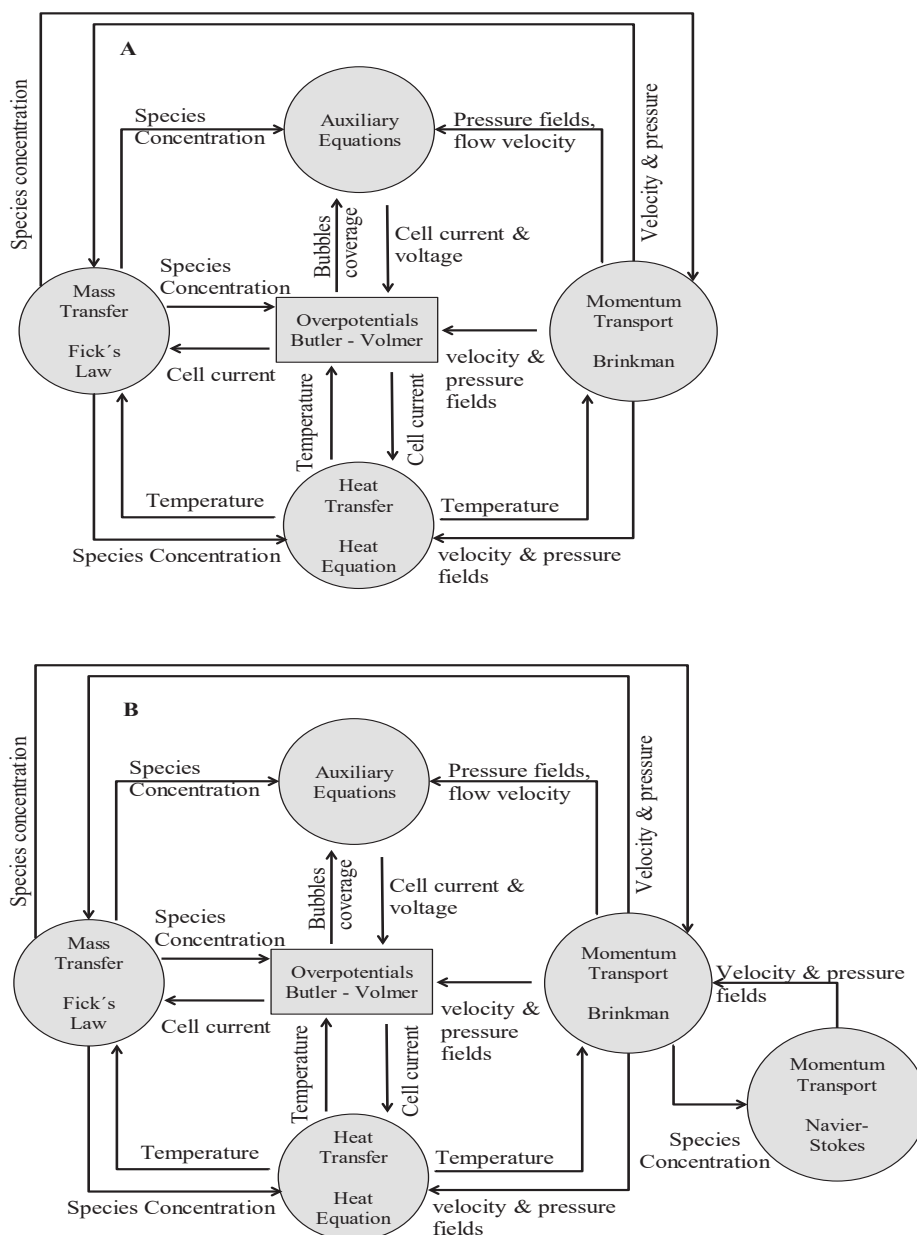


Figure 22: Model application modes and coupling strategy for, A) "Advanced" cell design without flow channels, B) Conventional cell design

In Figure 22, “Auxiliary equations” has been used to simplify the schematic and, it comprises the reversible cell voltage and all the semi-empirical equations for calculating the individual overpotential contributions, Eq. 20 to Eq. 47.

In order to solve the Dirichlet problem posed by the governing equations, appropriate initial and boundary conditions were imposed. All the model domains and boundaries are shown in Figure 23. The operating feed water flowrate was set as the boundary condition at the water inlets, while the operating pressure was defined at the cell water outlets to impose a gradient for momentum transport. The operating temperature was defined at all the feed water inlets, while the species concentrations (oxygen at the anode and hydrogen at the cathode) were set to zero. These boundary conditions were applied to both the conventional design model and the model for the design without flow channels.

Additionally, for the model of the conventional design, at the interface between the flow channel and the PTL where there is a transition from free flow in the channel to porous media flow in the PTL, the velocity u_{FC} is imposed at the boundary, thereby, introducing the feed water flow in the PTL for the conventional cell design. The no slip condition is applied at the bipolar plate walls indicating that the velocity is zero relative to the boundary. The boundary conditions are summarized in Table 8 and Table 9 for the conventional cell design and the design without flow channels, respectively.

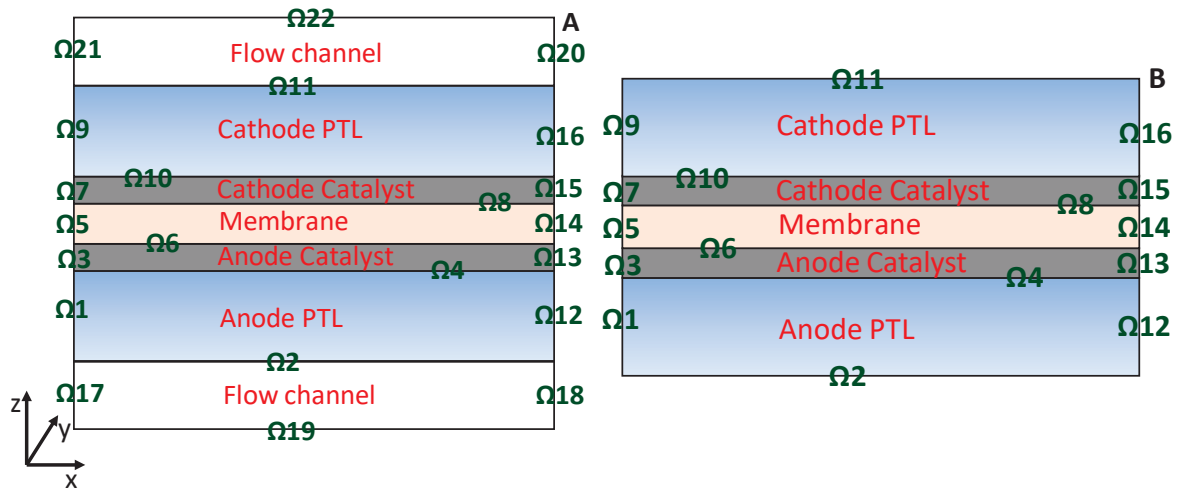


Figure 23: Model geometry and boundary conditions, A) for the conventional cell design, B) for the “advanced” cell design without flow channels

Table 8: Summarized boundary conditions for the model of the design with flow channels

Sub model	Boundary condition	Boundary (Ω)	Value
Momentum transport	Inlet fluid flow	17, 20	u_{in}
	Inlet Fluid flow	2, 11	u_{FC} (Navier-Stokes)
	Outlet fluid flow, Pressure	18, 21	p_0
	Wall, no slip	19, 6, 8, 22	$u = 0$
Mass transport	No flux	19, 6, 8, 22	
	Species concentration	1, 3, 17, 15, 16, 20	$C_i = 0$
	Out flow	18, 21	
Heat transfer	Temperature	17, 20	T_0
	Out flow	18, 21	
	Thermal insulation	19, 22	

Table 9: Summarized boundary conditions for the model without flow channels

Sub model	Boundary condition	Boundary (Ω)	Value
Momentum transport	Inlet fluid flow	1,3,15,16	u_{in}
	Outlet fluid flow, Pressure	12,13,7,9	p_0
	Wall, no slip	2,6,8,11	$u = 0$
Mass transport	No flux	2,6,8,11	
	Species concentration	1,3,15,16	$C_i = 0$
	Out flow	7,9,12,13	
Heat transfer	Temperature	2,5,11,14	T_0
	Out flow	7,9,12,13	
	Thermal insulation	2,5,11,14	

The coupled governing equations with the applied boundary conditions were solved numerically using the algorithm of the non-linear solver of COMSOL Multiphysics® v4.2 [124], based on the finite element technique.

Meshing of the 2-D modelled geometry was done prior to the start of the numerical solution. Dense quadrilateral mesh elements were used at regions where high gradients are expected, such as the PTL|catalyst layer interfaces and at the channel|PTL interfaces (for the conventional design only). Otherwise, fine triangular mesh elements were used in all other sub-domains and boundaries, giving a total of ~300,000 mesh elements, Figure 24.

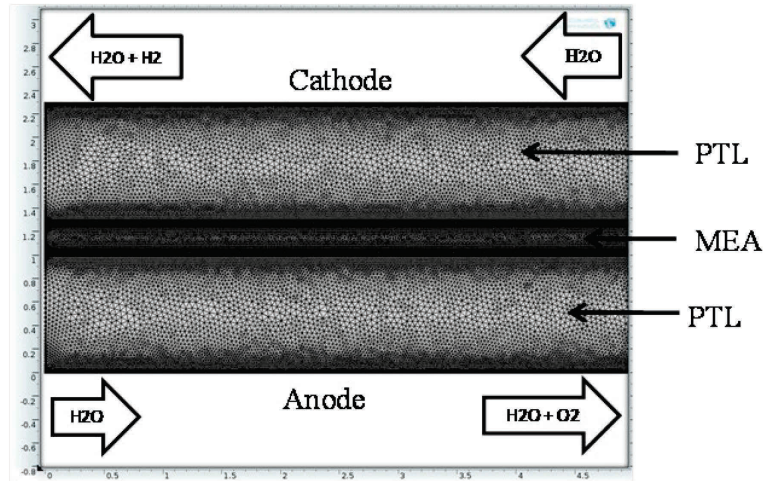


Figure 24: Mesh distribution on the model geometry, for the design without flow channels

To maximise computational resources due to the complexity of the models, and to improve the numerical convergence, the solution was carried out in three steps. In the first step, the momentum and mass transport sub-models were solve and the results were used in the second step as starting solution for the heat transfer sub-model. Finally, in the third step, the generated results were used as input to a parametric sweep algorithm, which calculated the polarisation curves according to Eq. 48 by ramping up the current density in steps from 0 – 5 A/cm².

4.4 Model Assumptions and Limitations

In order to reduce the complexity of the already very complex models developed, certain assumptions were made which could consequently affect the quality of the models and the results predicted by them. Those assumptions and their expected effect on the quality of the models are:

- Uniform and optimal compression pressure was assumed all over the active cell area, especially at the PTL|catalyst layer interface where the water splitting reaction takes place. This is not normally the case in actual PEM electrolysis cells. Because of the presence of fairly compressible cell components, the clamping pressure applied at the endplates do not homogenously spread across the active area, giving rise to interfacial

contact losses [125]. As a consequence of this assumption, the advantage in performance at the ohmic region of the polarisation curve that the design without flow channel has over the conventional design, see Figure 15, will not be reflected in the model results.

- Since the bipolar plate, PTL and electro-catalysts are thin and made from highly conductive materials, it was assumed that electron transport is infinitely fast and therefore the current density distribution on the active area is uniform. Consequently, hot spots and local temperature variations cannot be reflected in the model results.
- Interfacial contact resistance that occur between adjacent cell components due to the resistivity to the flow of electrical current was not considered in the models, similar to [126]. As a result, calculated polarisation curves will be under estimating the contribution of ohmic overpotentials to the cell voltage. Consequently, ohmic correction will have to be performed on the measured polarisation curves prior to model validation.
- Gas phase tracking and phase equilibria has not been considered in the models. Consequently the effects of local pressure variations will not be captured in the model results and hence, the calculated cell performance.
- The model assumes balanced pressure operation at the anode and cathode, therefore there is no gas crossover and related effects considered. This is especially not the case for a PEM electrolyser operating at elevated pressures at low current densities [127,128]. The crossover of gasses, especially hydrogen from cathode to anode side (under a pressure gradient) may lead to recombination reaction that could be a source of a parasitic current consumption and voltage degradation. This effect is clearly not reflected in the model predictions as a result of this assumption.

- It is assumed that the membrane is always fully hydrated and the membrane humidification is constant at $\lambda = 24$, Eq. 33. This assumption may not be true especially at extreme conditions of low operating water flowrate. In such a situation, the polarisation curve predicted by the model will under estimate the contribution of the membrane overpotential to the operating cell voltage.
- Also based on the assumption that the flow of electrical current through the bipolar plate, PTL and electro-catalyst layer is infinitely fast, the effect of joule heating within the cell has not been considered in the models. Consequently, the model may slightly underestimate the temperature gradients within the cell and its effect on the calculated polarisation curves.

Chapter 5

Experimental Methods

Some of the independent variables used in the models developed in Chapter 0 are important material properties (mean pore diameter, d_{pore} , of PTL and $j_{o,ref}$ and E_a of the OER catalysts) that could not be obtained from the manufacturers. Therefore, ex-situ experiments had to be performed to obtain the values of those parameters. Also, the developed models had to be experimentally validated in order to serve as a reasonable tool for predicting and characterising the PEM electrolysis cell performance.

This chapter describes the materials and methods that have been used to perform; 1) ex-situ experiments to determine important material parameters of the PTL and the OER electrodes and 2) in-situ experiments to measure real polarisation curves against which the model predicted performance curves will be validated.

5.1 Ex Situ measurement of material and electro-kinetic properties

Most manufacturers hold as confidential and do not disclose certain material properties of some of their products. When faced with such a situation, the unknown material properties have to be determined experimentally. Similarly, parameters describing the rate and progress of a chemical reaction which can be found in books and tables depend strongly on the conditions (temperature, pressure, mixture content etc.) under which they were experimentally determined. Thus, it is not always the best practice to directly use such values from books and tables in a scientific work.

This section will describe the ex-situ experiments that have been performed to determine the microstructure parameters (average pore size, pore distribution), which were not disclosed by the manufacturer, of the PTL samples used in this work; and the electro-kinetic parameters for the OER catalyst.

5.1.1 Determination of the microstructure properties of the PTL

All the PTL samples used in this work were 1 mm thick porous plates made from thermally sintered Titanium (grade 2) powder, acquired from MOTT Corp®, USA, all produced in the same batch. Each plate had a porosity of 40 % (parameter value disclosed by manufacturer).

The mean pore size (diameter) of the PTL which was not disclosed by the manufacturer is an important parameter that affects mass transport (the supply of reactant water to, and the evacuation of produced gases from the active site) within the cell. Indeed, as shown in Eq. 42, the pore diameter has a direct effect on the pore-to-bubble ratio and hence to the bubble overpotential (mass transport limitation) and thus the cell polarization. It therefore, becomes imperative that the PTL average pore size is determined experimentally prior to model validation.

Capillary flow porometry technique was used to determine the pore diameter and size distribution of the PTL in accordance with the ASTM standard [129]. The equipment used was the POROLUX 1000® purchased from manufacturer POROTEC GmbH, Hofheim am Taunus, Germany. The bubble point, maximum pore size, mean flow pore size, minimum pore size and the average pore size distribution were measured.

The capillary flow porometry technique uses the simple principle of gas pressure to force a wetting liquid out of the through-pores in a sample. The pressure at which the pores empty is inversely proportional to the pore size. Larger pores require a lower pressure than smaller ones.

The resulting volumetric flow of gas through emptied pores is then measured. The pore size is then calculated using Eq. 63, known as the Washburn equation.

$$d_{pore} = \frac{4\gamma \cos \beta}{p} \quad \text{Eq. 63}$$

The test sample was soaked with a wetting fluid to completely fill its pores. Dry gas at a pre-set flowrate was then used to force the wetting liquid out of the through pores. The largest pore to be emptied (at the lowest pressure at which flow is sensed) defines the so-called "bubble point". After all pores have been emptied (up to the highest pressure achievable) during the "wet" run, a second "dry" run is performed on the same sample Figure 25.

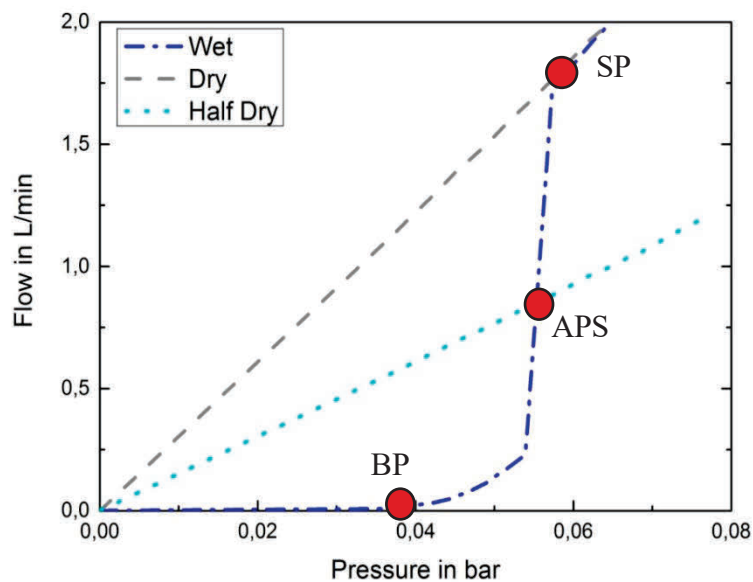


Figure 25: Schematic of capillary flow porometry characteristics. BP is the bubble point (largest pore), APS is the average pore size and SP is the smallest pore

The wet curve was obtained using the wetting fluid Porefil from POROTEC GmbH. The Porefil is an inert, non-toxic, fluorocarbon fluid which exhibits a zero contact angle for accurate results. Pore size analysis was subsequently performed on all samples of the PTL used in this work and the results are presented and discussed in Section 6.

5.1.2 Determination of the electro-kinetic parameters of the OER catalyst

The MEAs used in all in-situ experiments and simulated in the model were E300 from Greenerity® Hanau, Germany. All the MEAs were supplied from the same production batch and, it is known (from the manufacturer) that, the OER electrodes were made of Ir/IrO₂ catalysts. However, electro-kinetic parameters for the water splitting reaction on the Ir/IrO₂ is not known and had to be determined experimentally. The determination of the electro-kinetic parameters was done only on the anode electrodes because the OER is the overwhelmingly dominant source of activation overvoltage in PEM water electrolysis, and the parameters for the HER were taken from the literature, Table 10.

The ex-situ experiments to determine these parameters were performed in collaboration with the department of Chemical and Biological Engineering and the Clean Energy Research Center, University of British Columbia in Vancouver, Canada.

The electro-kinetic parameters like the exchange current density, $j_{o,ref}$, Tafel slope, b , and the activation energy, E_a , for the OER on iridium surface were obtained in a classical 3-electrode solution-based cell. Of these, the most important parameters of use were $j_{o,ref}$ and E_a which would serve as direct input in to Eq. 30, for the determination of the exchange current density j_o , at different operating temperatures.

These measurements were performed by a rotating disk electrode (RDE) setup (Pine Electrochemistry, USA) using a solid-state Ir disk (5mm, Alfa Aeser) working electrode, a Pt flag counter electrode and a Hg/Hg₂SO₄ reference electrode (Radiometer Analytical). Polarization curves were collected at a scan rate of 20 mV/s in the potential window of 1.23 to 2.00 V vs. SHE, while rotating at 1600 RPM to remove the oxygen bubbles evolved during the reaction [130]. Data were collected at 20, 40, 60 and 80 °C electrolyte temperature. The Tafel slope and exchange current density were determined using the Tafel relation:

$$\eta = b * \log\left(\frac{j}{j_{o,ref}}\right) \text{ or } \eta = b * \log(j) - \log(j_{o,ref}) \quad \text{Eq. 64}$$

When the fraction in the log term is expanded, a Tafel equation is obtained that is analogous to a standardized linear equation. Once the Tafel equation is obtained for each temperature, the $j_{o,ref}$ can then be calculated by letting η equal to 0 and solving for it algebraically.

For a fixed overpotential, the current density was read from a family of temperature curves. The activation energy (E_a) was then determined by making an Arrhenius plot and deduced from the slope of the graph $\log(j)$ vs $1/T$.

$$\log j = \frac{-E_a}{\ln(10RT)} + \text{constant} \quad \text{Eq. 65}$$

The electro-kinetic parameters used in all the simulations in this work are summarised in Table 10.

Table 10: Values of the electro-kinetics parameter used in this work

	$j_{o,ref} \left[\frac{mA}{cm^2} \right] @ 80^\circ C$		$S_{eff} [-]$		$E_a \left[\frac{kJ}{mol} \right]$	
	Value	Source	Value	Source	Value	Source
Anode	$5.35 * 10^{-4}$	[This work]	100	[131]	15.0	[This work]
Cathode	1	[107,132]	40	[131]	18	[107,132]

5.2 In Situ measurement of performance curves

In this section, the materials, methods and experimental set-up used in measuring real polarisation curves, against which those predicted by the models are validated, will be described.

5.2.1 Test cell design and construction

A laboratory test cell with an active area of 25 cm² that can be operated either as a conventional test set-up with flow channels or as a test cell without flow channels was designed and constructed as shown in Figure 26 and Figure 27. Flow channel plates were machined separately and pockets were cut in the half-cells to accommodate the channel plates, thus allowing the cell to operate in a conventional manner. The parallel flow channels were 1 mm wide and the ridges were 1 mm high and 1 mm wide, Figure 54. All cell components were made from uncoated titanium grade 2.

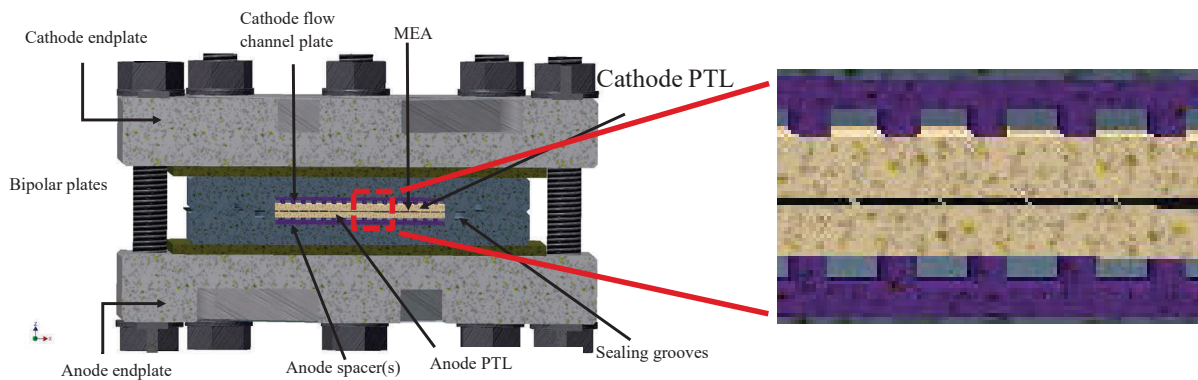


Figure 26: Cross section of the 3-D construction and assembling of the experimental test cell (Conventional design concept)

For the design concept without flow channels, the flow field plate was replaced in the pocket by a set of sheets of titanium spacers. The pockets in the half-cells were 4 mm deep thus allowing the user to vary the thickness of the PTL. The thickness and thus number of spacers used may vary for different test configurations and to accommodate for any possible gaps left from the manufacturing process.

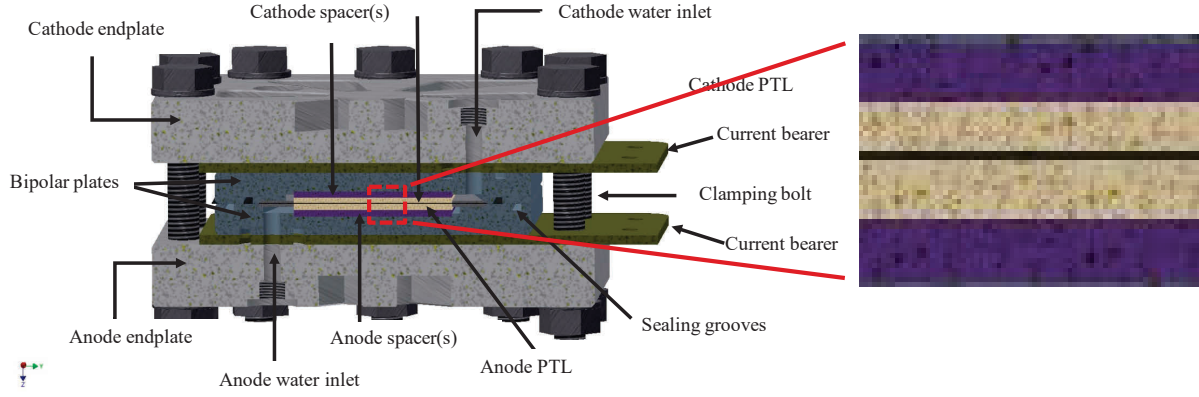


Figure 27: Cross section of the 3-D construction and assembling of the experimental test cell (design concept without flow channels)

As discussed in Section 1.5.1, the end plate is a very important component in a PEM water electrolysis cell as, amongst other functions, it ensures the optimal distribution of contact pressure across the active layer interface, thus enhancing cell performance. Therefore, the optimal design of the end plate is imperative to the design of a good performing cell.

The optimal thickness of the end plates was designed by a simple structural mechanics FEA model based on the optimal clamping load of the cell. The optimal clamping load of the cell was calculated by using the equivalent stiffness model approach of [133], see also Appendix A 1. The governing equation for solving the structural mechanics FEA problem was derived from the well known equation of motion with respect to the equilibrium condition, which is given by:

$$\nabla \cdot (D_{stiff} \nabla \bar{u}) = 0 \quad \text{Eq. 66}$$

Where, \bar{u} is the displacement (deformation) of the endplate material and D_{stiff} is the stiffness matrix of the isotropic end plate material, given by:

$$D_{stiff} = \frac{Y}{(1+r)(1-2r)} \begin{bmatrix} 1-r & r & r & 0 & 0 & 0 \\ v & 1-r & r & 0 & 0 & 0 \\ v & v & 1-r & 0 & 0 & 0 \\ 0 & 0 & 0 & \frac{1}{2}-r & 0 & 0 \\ 0 & 0 & 0 & 0 & \frac{1}{2}-r & 0 \\ 0 & 0 & 0 & 0 & 0 & \frac{1}{2}-r \end{bmatrix}$$

Where, Y and ν are respectively, the Young's modulus and the Poisson's ratio. Titanium grade 2 was the material of choice for the end plates and the model was solved for the plate deformation using COMSOL Multiphysics® v4.2. A plate thickness of 20 mm was chosen based on the low deformation of less than 0.001 mm under maximum clamping load and the low von Misses stress, Figure 28. Refer also to Appendix A 2.

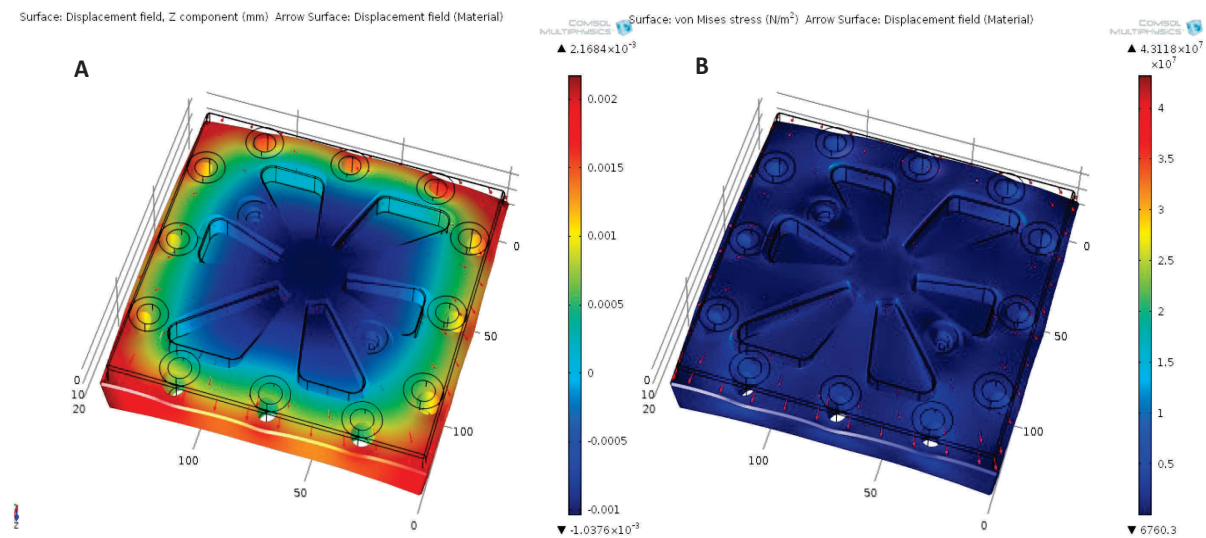


Figure 28: A) Surface plot showing maximum deformation of the pressure plate structure design clamping load, for a 20 mm thick plate, B) Surface plot showing maximum von Mises stress distribution on the pressure plate under the design clamping load, for a 20 mm thick plate

The cell components were assembled between the two end plates and clamped together by 12 bolts with sufficient torque to provide a contact pressure of 0.6 MPa on the active area. The end plates, current bearers and spacers were made from corrosion resistant titanium grade 2. Figure 29 shows the assembling of the two half cells. The PTL were also of titanium grade 2 and were acquired from MOTT Corp® (Farmington, USA). The MEAs used for all experimental investigations were the commercial product E300 from Greenerity® (Hanau/Germany) formerly known as SolviCore.

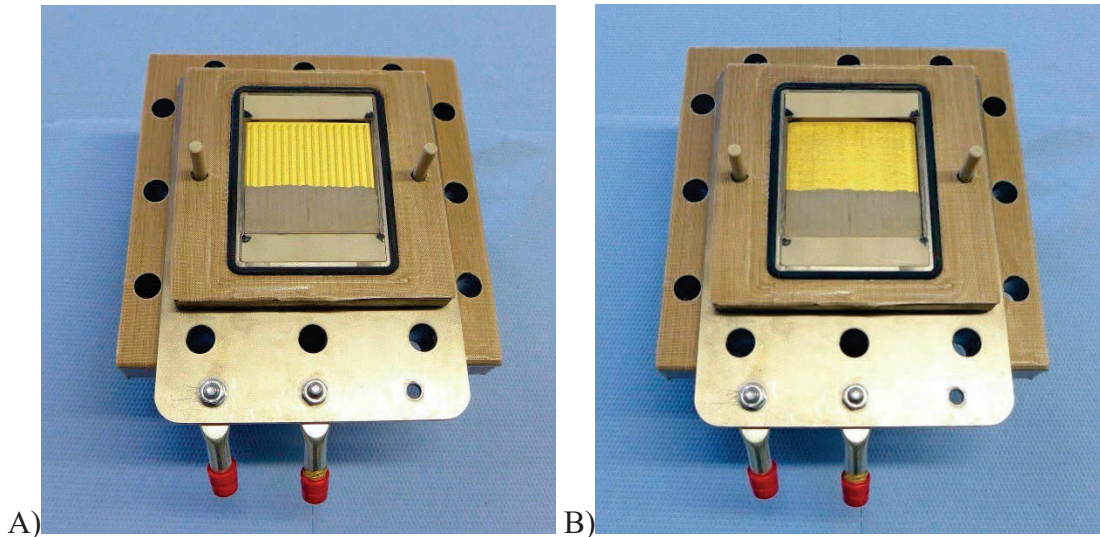


Figure 29: Test cell design. A) Conventional design with flow channels on the bipolar plate (partly covered by the PTL) and B) Alternative design without flow channels beneath the PTL. The active area of the test cell is 5 x 5 cm². Gold coated bipolar plates are shown here just to give a better contrast between the components. The bipolar plates used in all measurements were uncoated, see Appendix A 3.

5.2.2 Test system and polarization curves measurement

Polarization curves were measured in an in-house designed and constructed 1 kW semi-automated test station, capable of operating at pressures of up to 50 bar, Figure 30 and Figure 31. All measurements were performed at balanced pressure across the cell from the anode to the cathode. Feed water was supplied to both the anode and cathode compartments by the use of peristaltic pumps, thus, forming two separate circulation loops. The feed water was passed through ion exchangers to maintain the conductivity of the feed water at an acceptable level ($\leq 0.55 \mu\text{S}/\text{cm}$). In order to achieve the desired cell operating temperature, the deionized water in both compartments was re-circulated through a thermostat. Temperature, pressure and flow sensors were installed close to the inlet and outlet of each cell compartment. The cell operating conditions (temperature, pressure and water flow rate) were measured at the outlet and at the inlet. Monitoring these parameters made sure that 1) the temperature gradient between outlet and inlet was within $\pm 3 \text{ K}$, 2) the operating pressure was within $\pm 1 \text{ bar}$ and 3) the water flow rate fluctuation stayed $\leq 0.01 \text{ l}/\text{min}$.

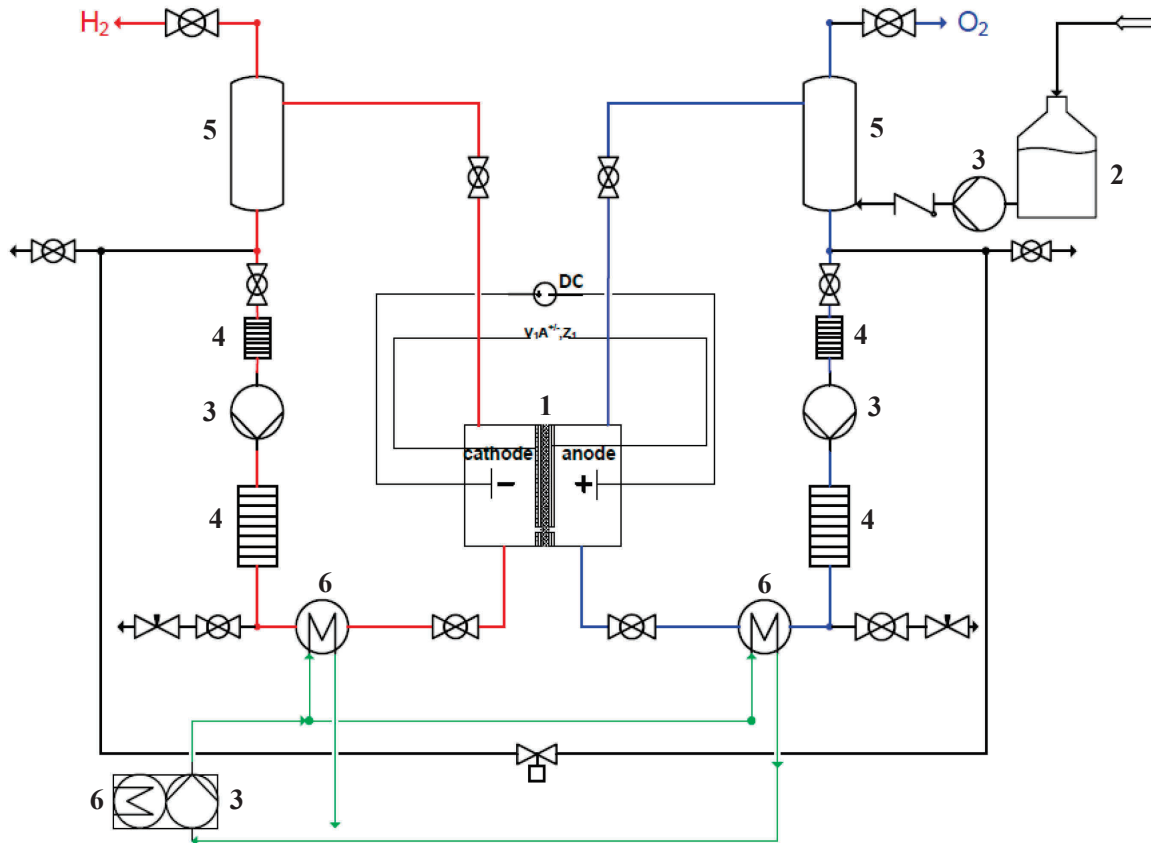


Figure 30: Simplified layout of the test system, not including all sensors but including the following important components: 1) PEM electrolysis cell; 2) Feed water tank; 3) pumps; 4) ion exchangers; 5) water – gas separators; 6) heat exchangers

Polarization curves were measured for different operating conditions (temperature, pressure and water flow rate) and cell configurations after conditioning of the MEA. The MEA conditioning was performed galvanostatically by cycling the cell current density between 1 A/cm² and 5 A/cm² for 12 hours at 80 °C and 1 bar. During each cycle, the current density was held alternately at 1 A/cm² for 30 minutes, followed by 5 A/cm², also for 30 minutes.

All polarization curves were measured by incrementing the current density from 0 A/cm² ≤ j ≤ 5 A/cm². The current density increments were chosen to obtain precise measures of the slope of each of the three regions of the polarization curve. For 0 A/cm² ≤ j ≤ 0.5 A/cm², where activation losses are dominant, current density increment of 0.05 A/cm² was used. At the ohmic (0.5 A/cm² ≤ j ≤ 3 A/cm²) and mass transport (3 A/cm² ≤ j ≤ 5 A/cm²) regions, increments of 0.25 A/cm² and 0.1 A/cm² were used, respectively. The equilibration time at each current

density step was 3 minutes and the cell potential was recorded every 5 seconds. The upper potential limit for the measurements was set at 4 V. A new MEA (and therefore, conditioning) was used for testing each set of operating parameters or whenever a new cell configuration was to be examined. Each measurement was repeated three times to confirm the reproducibility.

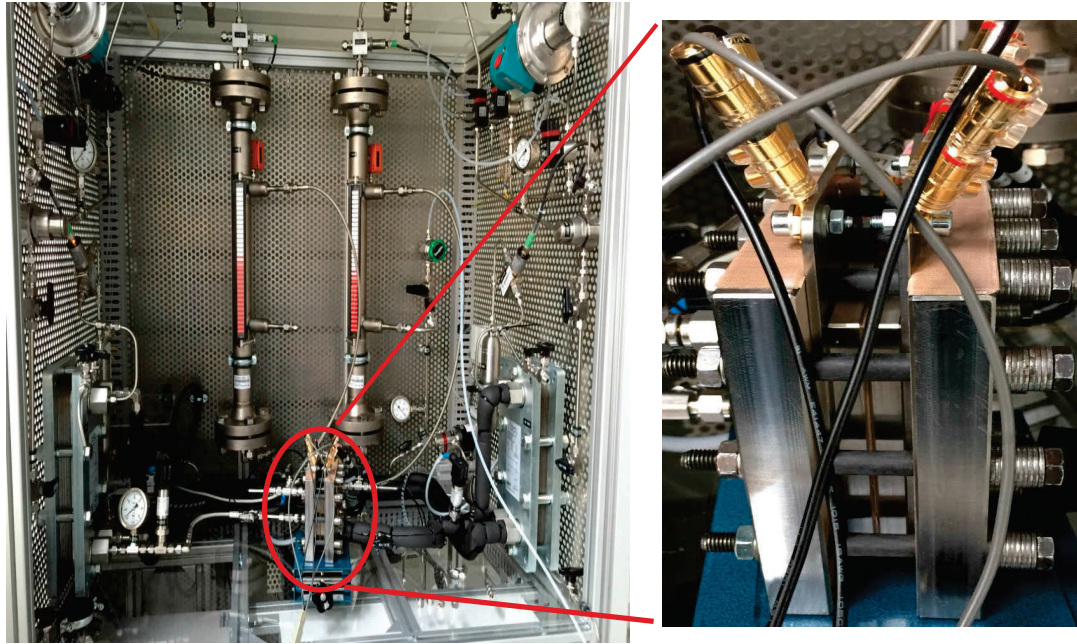


Figure 31: Test cell connected to the test rig

5.2.3 Interfacial contact resistance correction

As mentioned earlier, an interfacial contact resistance occurs between adjacent spacers and the half-cell components and also the PTLs which were not accounted for in the model development. These therefore, need to be considered and corrected prior to model validation and analysis of the results.

A high frequency impedance measurement approach as described by [134] and [135] was adopted to correct for the ICR related voltage losses. In order to appreciate the measured polarization curves, the performances of two test cells were compared; 1) a laboratory test cell with an active area of 25 cm² for benchmark measurements as used in [136] and 2) the test cell set-ups for the conventional design and for the design without flow channels as described

above. All test cells were assembled using the same PTL and MEA, and were assembled with the same clamping torque of 15 Nm. The same operating conditions were simulated in both cells while the impedance was measured at 1 kHz using a milliohmmeter from Agilent Technologies®. Table 11 shows the overall cell resistance for the two test cell set-ups and the baseline test cell and the ICR correction in dependence of the cell temperature. The additional contribution of the spacers to the cell resistance (interfacial contact resistance) was calculated according to Eq. 67:

$$Impedance_{spacers} = Impedance_{test\ cell} - Impedance_{baseline\ cell} \quad \text{Eq. 67}$$

Table 11: Measured HF impedance of the test cells and baseline cell and the resulting IR correction term.

Temperature (°C)	Test cell impedance (mΩ)		Baseline cell impedance (mΩ)
	With Flow Channels	Without Flow Channels	
40	14.50	13.48	8.70
60	12.20	12.00	7.61
80	10.50	10.30	6.52

Chapter 6

Results and Discussion

The results of this research work will be presented and discussed in this chapter. After validating the models, they will be used as tools to predict the performance of each cell design at different operating conditions, design parameters and PTL microstructure. Discussions will be based on the comparison of the cell with flow channels (conventional design) and the design without flow channels and the focus of the comparison will be on mass transport losses at high current densities ($> 3 \text{ A/cm}^2$). At the end of the chapter, operating conditions, design parameters and PTL parameters will be proposed for which the design without flow channels will perform as good as the conventional cell design.

6.1 Capillary flow porometry measurements

The pore sizes measured by capillary flow porometry are shown in Figure 32 for three different sintered titanium PTL samples. All the PTL samples were from the same manufacturer and from the same production batch.

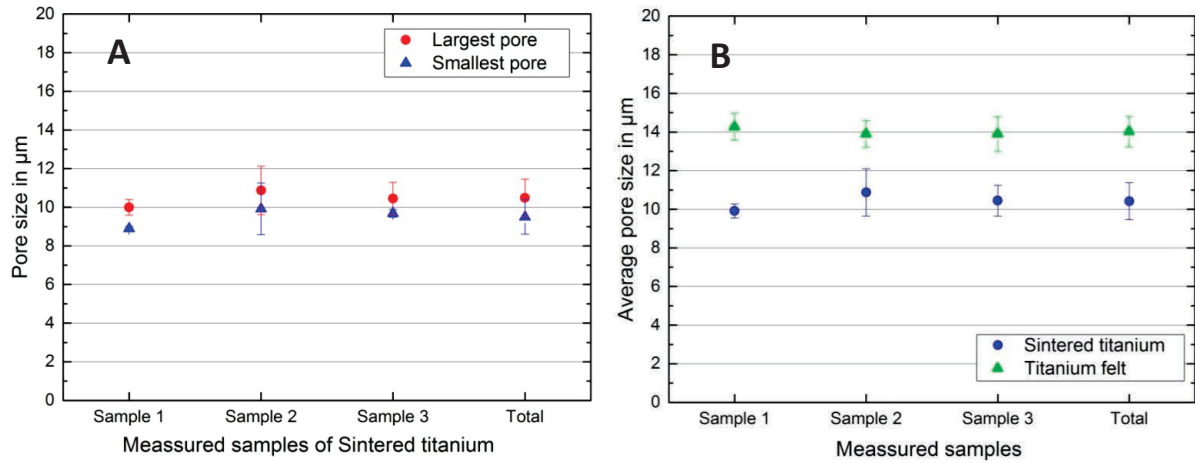


Figure 32: Porometry results, A) Measured average pore size of the baseline sintered titanium PTL, B) Comparison of measured pore size of the baseline sintered titanium and the measured pore size of titanium felt

Figure 32A shows the largest and smallest pore sizes of the measured sintered titanium samples, while Figure 32B shows the average pore size and compares them with measured pore sizes of titanium felt PTL samples (also from same manufacturer). The measured average pore size of the sintered titanium PTL samples was 11 μm and that of the titanium felt PTL sample was 14 μm , which is higher than that of sintered PTLs, as would be expected.

Ito [137] determined the mean pore diameter of titanium felt with fiber diameter of 20 μm and 50 % porosity to be about 12.7 μm . The pore size of the sintered titanium PTL depends on many factors, such as particle (powder) shape and size, sintering method and temperature and the PTL porosity. By adjusting the sintering conditions and powder size, Ito [67] could adjust the porosity of sintered PTL within the 30 – 40 % range while controlling the pore size within the 10 – 25 μm range. Using the capillary flow porometry technique on PTLs with varying powder size and porosities, Grigoriev et al. [71] determined the mean pore size of sintered PTLs to be in the range of 8 to 21 μm . The powder size of the PTLs used was between 40 – 100 μm and porosities between 35 – 40 %. Using powder size of 40 – 50 μm which is same as the powder size of the sintered PTLs used in this work, a mean pore size of 10.9 μm was reported with porosity of 37 %, meanwhile the porosity of the PTLs studied in this work was

40 %. The result of the measured mean pore size is therefore in agreement with results reported by [71].

The sintered PTLs measured were used for all the in-situ polarization curve measurements and its specifications (mean pore size and porosity) were used as input for all model validations requiring same.

6.2 Measured polarization curves

The polarization curves measured with the test cell incorporating both cell designs showed uncharacteristically high cell voltages compared to in house reference measurements in similar laboratory test cells with comparable cell components. Typical polarization curves with the chosen MEA was reported by Rau in [138] with cell potentials of 1.75 and 1.99 V measured at 1 and 2 A/cm² and a cell temperature of 80 °C. On the contrary, the test set-ups with flexible cell design resulted in 1.88 V and 2.13 V, respectively at similar current densities, for the design without channels and 1.83 V and 2.1 V for the conventional design, see Figure 33. The main reason for this comparably poor performance is attributed to the uncoated spacers that were used to fill in the pockets on the half-cells. An interfacial contact resistance occurs between adjacent spacers and the half-cell components and the PTL which contributes to ohmic drop due to the flow of electrons and thus accounts for an increase in the cell voltage. As the model presented does not account for any interfacial contact resistance, these ohmic losses observed on the polarisation measurements were corrected for ICR prior to model validation.

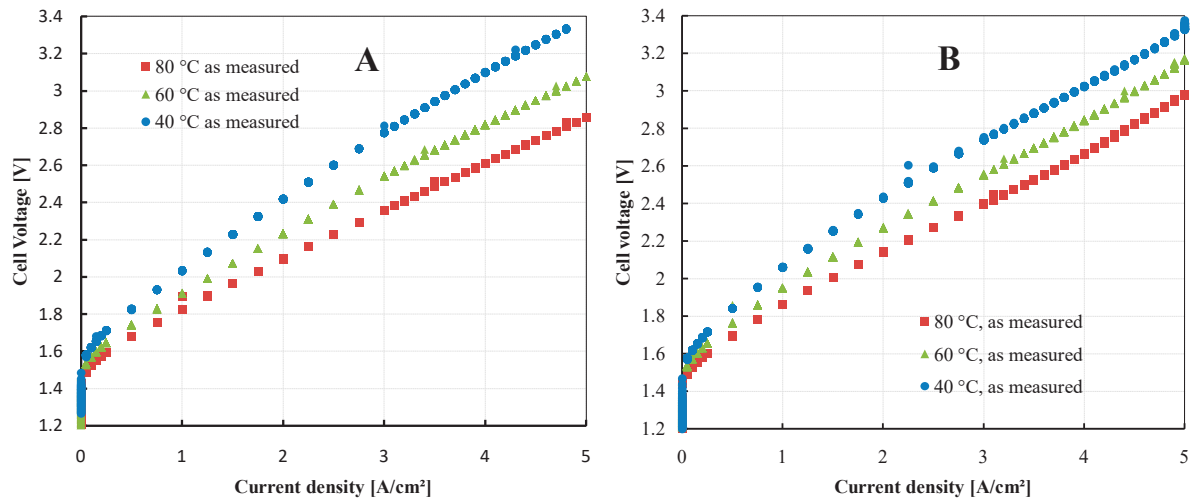


Figure 33: Temperature dependent polarization curves as measured with high interfacial contact resistance A) for the conventional design, B) for the advanced design without flow channels

6.3 Interfacial contact resistance correction

The measured high frequency impedance of the test cells, Table 11, is made up of the membrane ohmic resistance, the PTL and flow field plates, the electrodes and the interfacial contact resistance. As can be seen in Figure 34, the interfacial contact resistance and the membrane impedance increases sharply with operating current density which reflects the results of [139], while the impedance of the electrodes remain relatively constant beyond the activation region. This is due to the high electrical conductivity and the thin cross section of the electro-catalyst layer. The increase in the slope of the electrode impedance at current densities above 4 A/cm² could be as a result of the bubbles forming a kind of electrical double layer at the electrode interface. At such current densities (above 4 A/cm²), the contribution of the electrodes to the cell voltage is 23.3 %, while that of the membrane and other electron conducting internal cell components make up 48.6 %. The interfacial contact resistance make up 28.1 % of the total cell impedance.

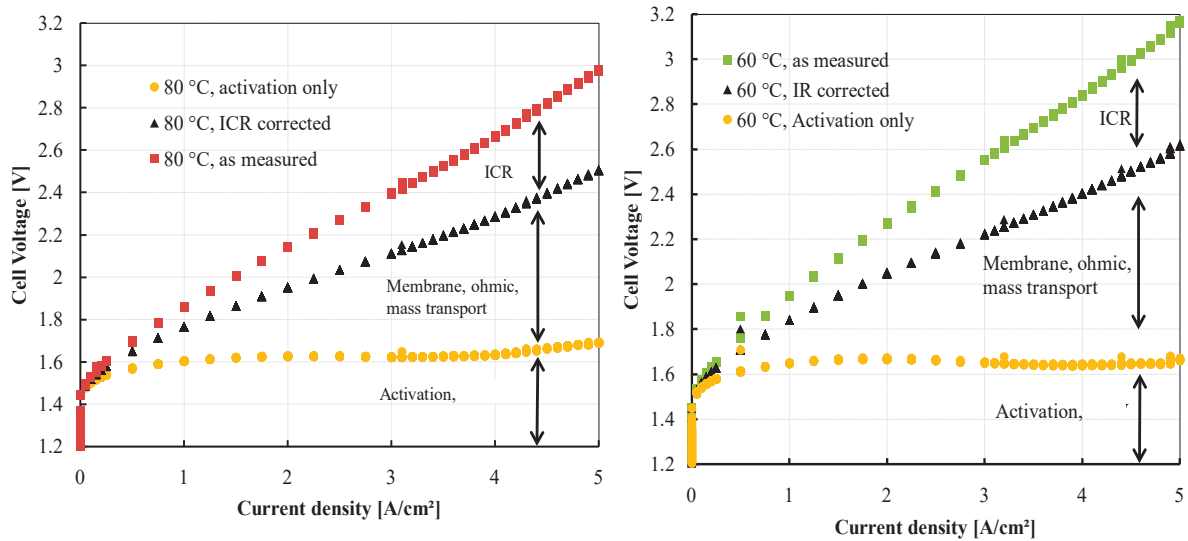


Figure 34: IR correction of temperature curves for design without channels. See Appendices B 1 and B 2 for further IR correction curves

Figure 35 compares the measured polarization curves with the ICR corrected polarization curves at three different temperatures. Performance of the test hardware is much closer to the baseline [136], after the ICR correction. Thus, all the experimental data collected were ICR-corrected in a similar manner prior to model validation.

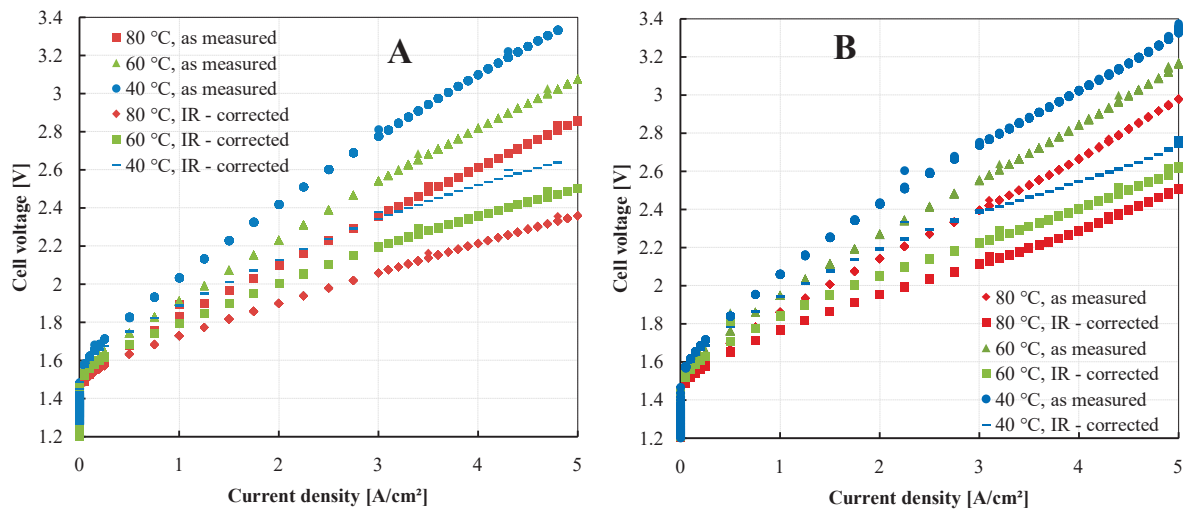


Figure 35: As measured and ICR corrected polarisation curves compared for A) the conventional cell design B) cell design with flow channels

The effects of operating current density, temperature and the cell design set-up on the voltage drop due to interfacial contact resistance is summarized in Table 12. An increase in the voltage drop due to the interfacial contact resistance with increasing current density could be observed

at all operating temperatures and cell set-up configurations. This is expected since the effect of the interfacial resistance is ohmic in nature and has a proportionality dependence on the current density as shown in Eq. 34. However, as the operating temperature is increased, the voltage drop due to the contact resistance is observed to decrease for both cell configurations and across all current densities. This result corroborates the findings of [140] and [141].

For all operating current densities and temperatures, it can be observed that the voltage loss due to the interfacial contact resistance is smaller for the design without flow channel than for the design with flow channel. As earlier mentioned in Chapter 0, one of the advantages of the cell design set-up without flow channels is its compactness. As a consequence of this compactness, the clamping pressure from the endplates is more effectively and evenly distributed all through the cell, resulting in lower contact resistance.

Table 12: Summary of the effects of current density, operating temperature and cell design on the voltage drop due to the interfacial contact resistance

$j \left[\frac{A}{cm^2} \right]$	$\Delta V_{ICR} [V]$ at 40 °C		$\Delta V_{ICR} [V]$ at 60 °C		$\Delta V_{ICR} [V]$ at 80 °C	
	With channels	Without channels	With channels	Without channels	With channels	Without channels
1	0.21	0.12	0.15	0.11	0.10	0.07
2	0.29	0.24	0.23	0.22	0.20	0.19
3	0.44	0.37	0.34	0.33	0.30	0.28
4	0.58	0.48	0.46	0.44	0.40	0.38
5	0.70	0.60	0.57	0.55	0.50	0.47

6.4 Validation of models

The experimental data were fitted with the model predictions, for different operating temperatures (40, 60, 80 °C), pressures (1, 5, 10, 30 bar) and water flowrates (0.2, 0.4, 0.6 l/min). The out-of-plane width (in the y-direction as shown in Figure 23 of the modelled geometry was 0.03 cm giving a modelled active area of 0.15 cm². The best fit with experimental data was achieved with a bubble density of 10,000 bubbles/cm².

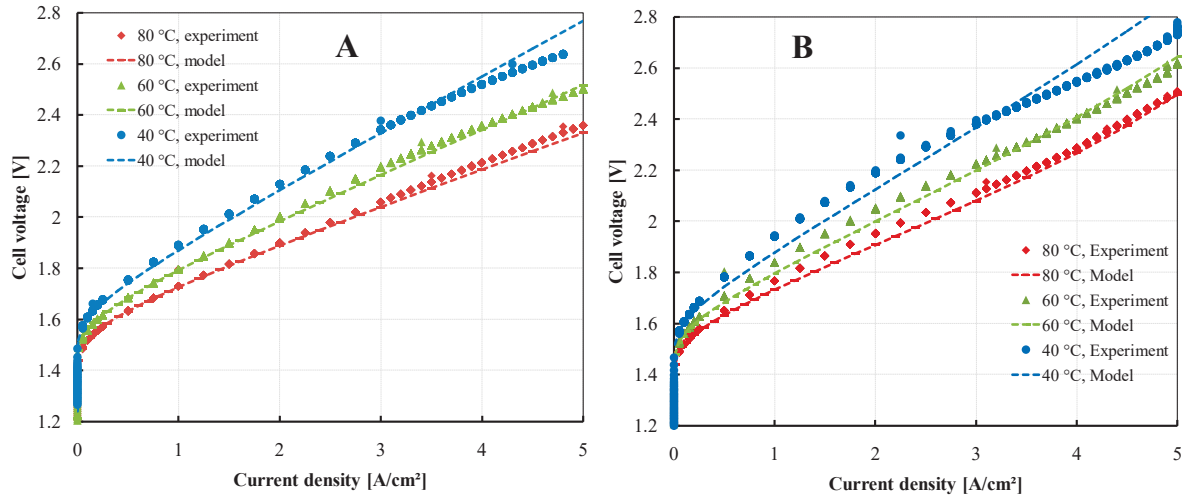


Figure 36: Comparison of the measured and predicted polarisation curves for A) the conventional cell design, B) the advanced design without flow channels

Figure 36 compares simulated and experimentally measured polarization curves at different operating temperatures for A) the conventional and B) the “advanced” cell design without flow channels. Modelled and experimental data agree well at all temperatures measured for the low current density region for both cell design concepts. For cell concept without flow channels, at mid current densities ($0.5 \text{ A/cm}^2 \leq j \leq 2 \text{ A/cm}^2$), where ohmic losses become dominant, a slight discrepancy between the experimental and the simulated data can be observed for the three different temperatures. This discrepancy is however, not seen in the conventional design set-up. It is speculated that the observed discrepancy is a result of interfacial contact resistance between the extra number of spacers included in the design without flow channels that increased the margin of error for in the ohmic correction. It should be noted that, the benchmark cell used for ohmic correction was of the conventional design concept, hence the ohmic correction accounted only for the number of spacers used in the conventional design cell. However, in the cell design concept without flow channels, many more layers of spacers were used to make up for the thickness of the flow channel plate, thereby, increasing the error margin of the ohmic correction for the design without channels.

At high current densities ($j \geq 3 \text{ A/cm}^2$), where mass transport and bubble effects are dominant, a good agreement between model and experimental results can be observed at $80 \text{ }^\circ\text{C}$ and $60 \text{ }^\circ\text{C}$ for both cell designs. However, at an operating temperature of $40 \text{ }^\circ\text{C}$, the predicted cell potential is much higher than the measurements for $j \geq 3 \text{ A/cm}^2$. Polarization measurements at $40 \text{ }^\circ\text{C}$ and current densities of up to 5 A/cm^2 have not been reported in the literature. Lewinsky [54] has reported measured polarization curves up to 16 A/cm^2 , but the polarization curves were measured at $80 \text{ }^\circ\text{C}$ and, such an effect seen here at $40 \text{ }^\circ\text{C}$ were not observed. Thus, a direct comparison with other work is not possible.

A possible explanation would be that; the improvement in performance is as a result of improvement in electrokinetics due to the higher temperature. As explained in Section 5.2.2, the cell temperatures were controlled at the inlet of the anode and cathode half cells thus self heating is more dominant at higher current densities and leads to a shift of the average cell temperature, see Figure 37 and Figure 38. However, running the simulation with the temperature variation measured in situ during the polarization curve measurement, Figure 37B and Figure 38B, it was still not possible to get the predict the experimentally measured performance.

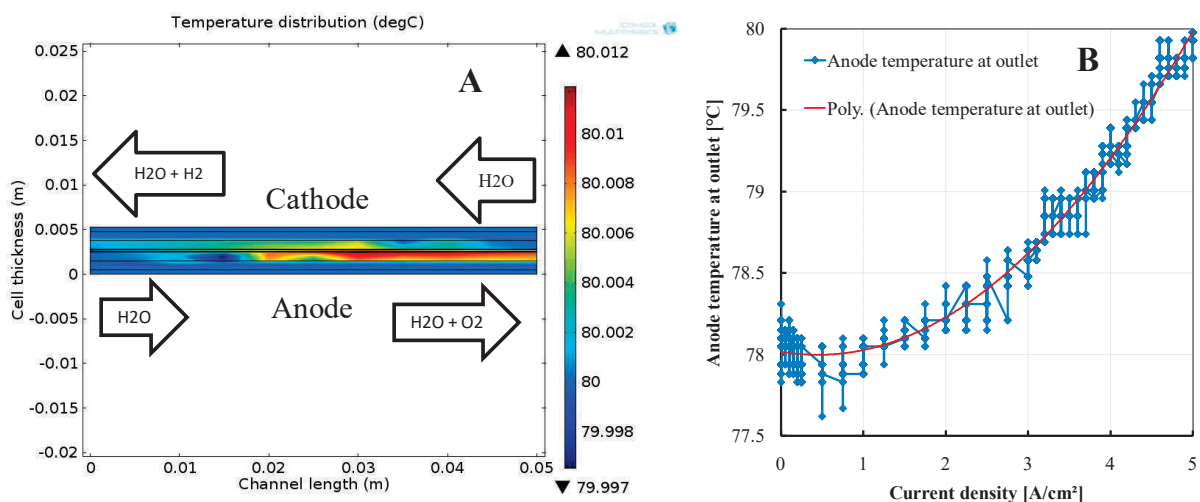


Figure 37: Cell temperature distribution in the conventional design A) modelled at $80 \text{ }^\circ\text{C}$, 1 bar and 5 A/cm^2 current density B) measured at the anode water outlet at operating water flowrate of 0.6 l/min and 1 bar . Data for 60 and $40 \text{ }^\circ\text{C}$ are shown in Appendix B 3

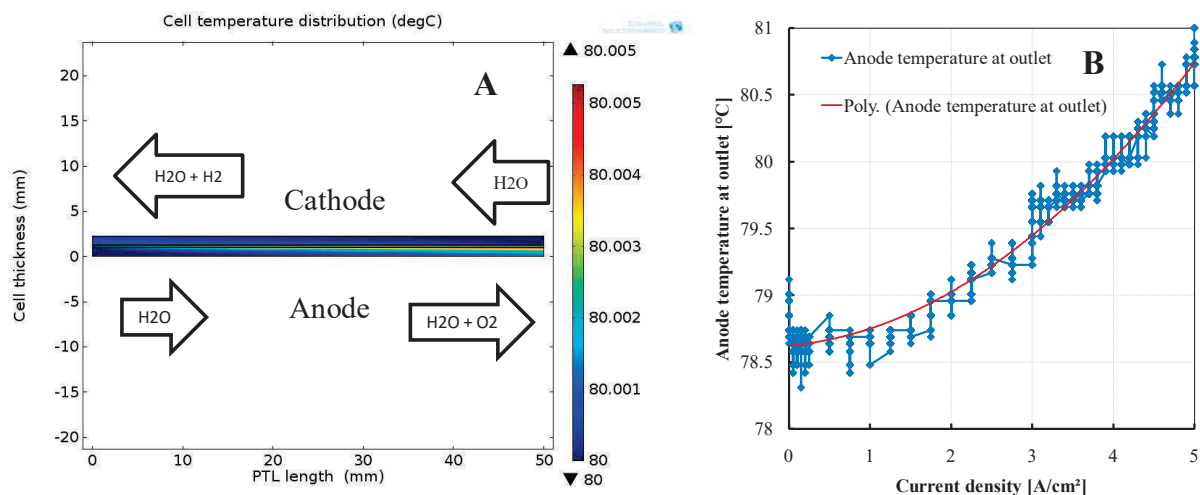


Figure 38: Cell temperature distribution in the design without flow channels A) modelled at 80 °C, 1 bar and 5 A/cm² current density B) measured at the anode water outlet at operating water flowrate of 0.6 l/min and 1 bar. 60 °C and 40 °C data are shown in Appendix B 4

Another possible explanation for the deviation of the predicted data from measured data at current densities above 3.5 A/cm² could be the possible depletion of TiO₂ passivation film on the spacers and the sintered PTL. According to the Pourbaix diagram of titanium Figure 39, above 2.0 v (vs. SHE) corrosion of titanium is thermodynamically favorable and the passivation film (TiO₂) starts to deplete. Thus it is likely that above 2.0 V, a more metallic titanium metal surface, which has a conductivity of one order of magnitude higher than TiO₂, will be exposed. This could reduce the ohmic overpotential and lead to an improved performance as seen observed. Such an effect will be expected to be more pronounced at low temperatures because the bubbles are smaller and mass transport limitation due to bubbles becomes docile. This hypothesis however, could not be conclusive since it could not be reproduced neither experimentally nor numerically and, such an effect has not been reported in the literature.

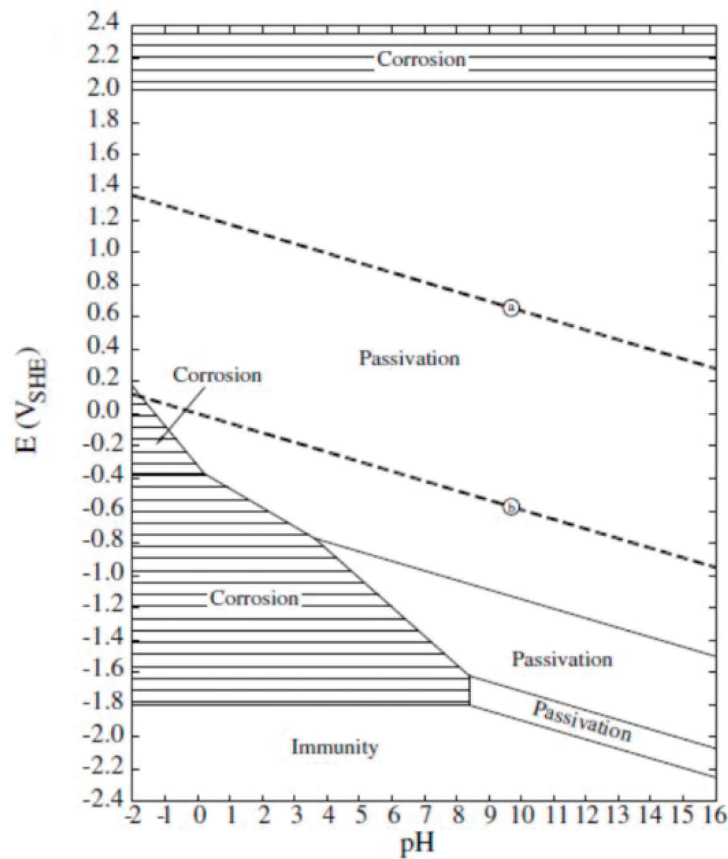


Figure 39: Pourbaix diagram of titanium in water at 25 °C [142]

Although the apparent reduction of the TiO_2 may lead to a performance gain, the long term durability of the titanium-based porous transport layers is not known at this stage. The breakdown of the TiO_2 film is a corrosion process and the heavy metal ions produced could take up active sites on the MEA and lead to the irreversible destruction of the MEA. Further work is required to elucidate the possible impacts of titanium corrosion on the overall performance and durability of the PEM electrolysis cell.

It can however, be observed that there is very good agreement between the predicted and experimentally measured polarization curves, Figure 36, at higher operating temperatures (60 and 80 °C) over the complete range of current densities studied. Therefore, the analysis of the temperature effects on the cell performance shall henceforth be based on the high temperature operating condition (60 and 80 °C).

Figure 40 compares the predicted and experimentally determined effects of the inlet water flowrate on the cell polarization curves at a cell temperature of 60 °C and at 1 bar operating pressure for A) the conventional cell design and B) the cell design without flow channels; at different operating water flowrates (0.6, 0.4 and 0.2 l/min).

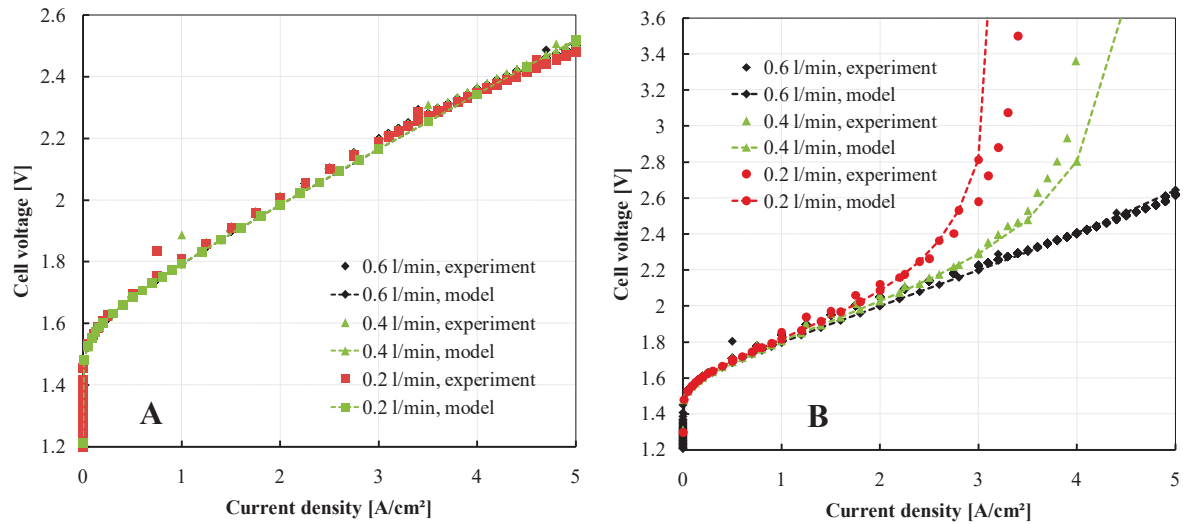


Figure 40: Comparison of measured and predicted polarisation curves for different water flowrates at 60 °C and 1 bar for A) the conventional cell setup and B) the cell setup without flow channels

There is very good agreement between the measured and predicted performance curves for all water flowrates considered for the conventional design. For the design without flow channels, for water flow rates of 0.2 and 0.4 l/min, mass transport effects become a strong limiting factor when $2 \text{ A/cm}^2 \leq j \leq 3 \text{ A/cm}^2$. The discrepancy in the cell potential between the predicted and measured performance at high current density ($j \geq 3 \text{ A/cm}^2$) at these low water flowrates is attributed to voltage fluctuations in the control set-up at high potentials ($\geq 3.5 \text{ V}$) close to the voltage threshold ($\sim 4 \text{ V}$) of the test rig. However, a very good qualitative agreement between the modelled and experimental data can be observed even at high current densities, which shows that the model is clearly capturing the effects of the mass transport limitation for both cell design set-ups.

The comparison of model prediction and experimental data for pressure dependency is shown in Figure 41 for A) the conventional cell design and B) the cell set-up without flow channels.

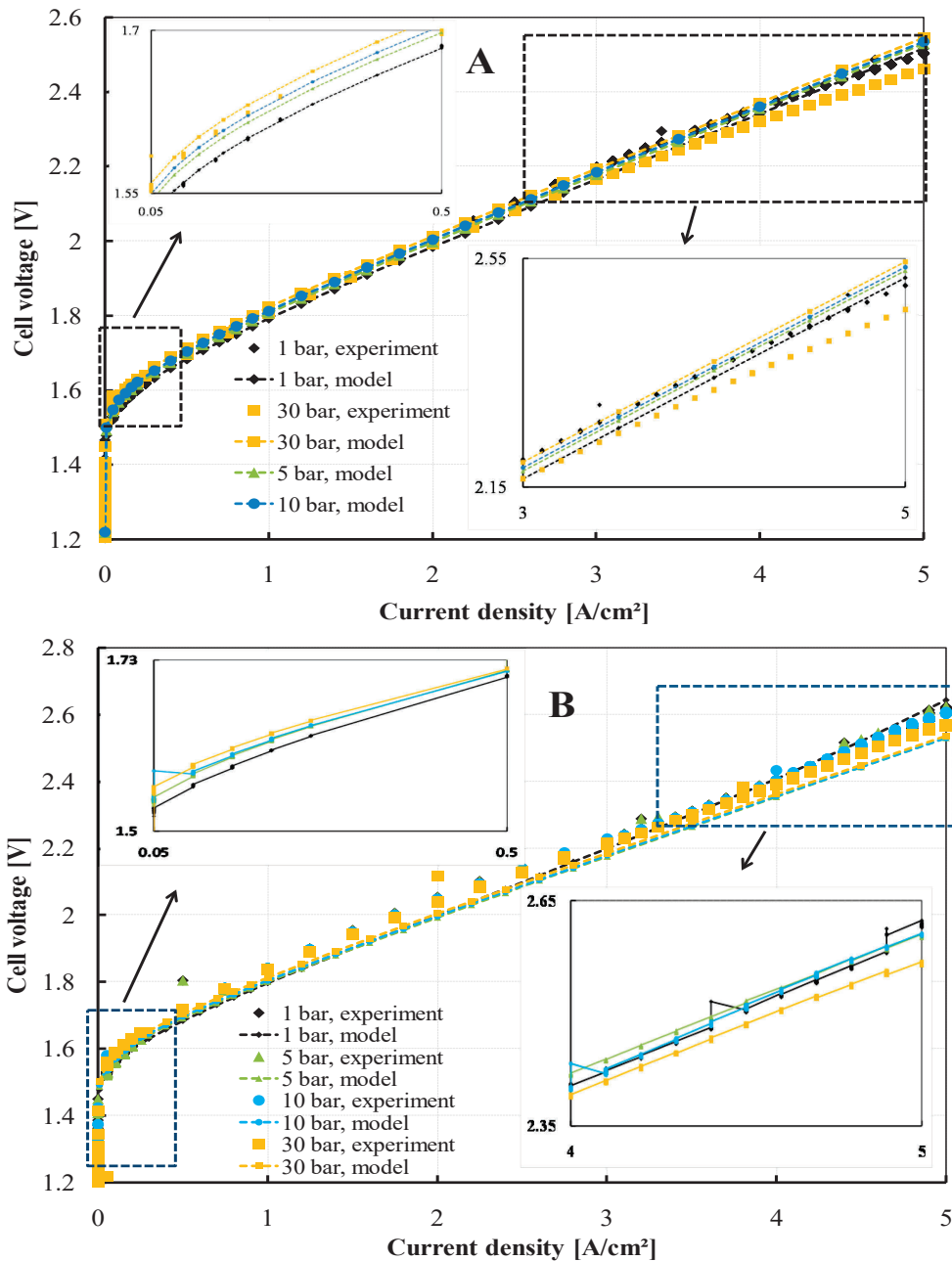


Figure 41: Comparison of measured and predicted polarisation curves for different operating pressures at 60 °C and 0.6 l/min water flowrate for A) the conventional cell setup and B) the cell setup without flow channels

A good agreement between experimental and predicted performance is observed at all operating pressures at the current density range studied for both the conventional cell set-up and the cell design without flow channels. This shows that the model is capturing the effects of the operating pressures and is thereby validated.

With the predictive performance of the models validated by fitting and comparison against real experimentally measured polarization curves, the models will henceforth be used to analyse

and to understand the effects of operating, micro-structural and design conditions on the performance of both cell designs, especially at high current densities where mass transport is dominant.

6.5 Effects of the operating parameters

In this section, the effects of operating conditions, such as temperature, pressure and the feed water flowrate on the PEM water electrolysis cell performance will be presented and discussed for both of the designs studied. The impact of the operating conditions on the three regions of the polarization curve (activation, ohmic and mass transport regions) will be analysed with focus on the high current density region where mass transport limitation due to bubble formation becomes limiting to the cell performance.

6.5.1 Cell operating temperature

The predicted effect of temperature on the cell polarization at 80, 60 and 40 °C is shown in Figure 42 for both cell design concepts. As is expected, the cell performance generally improves with increasing operating temperature. At low current densities, $j < 0.5 \text{ A/cm}^2$, the cell voltage is composed of the reversible cell voltage, Eq. 25 and the activation overpotential, Eq. 27.

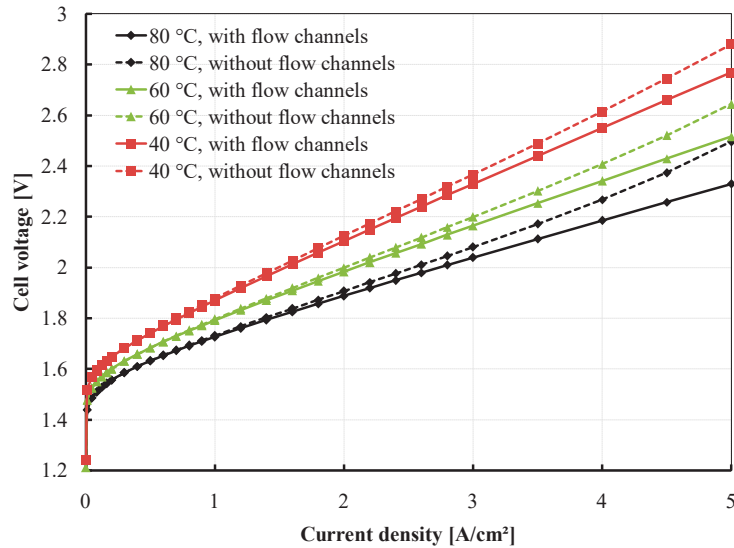


Figure 42: Comparison of the calculated temperature dependent polarisation curves for the conventional and advanced cell design concepts. Both models were simulated at 1 bar operating pressure and 0.6 l/min feed water flowrate

The decrease in the reversible cell voltage with increasing temperature coupled with the decrease in the activation overpotential with increasing temperature is generally responsible for the improvement of cell performance with increasing operating temperatures.

Although both cell set-ups perform the same for current densities up to about 1.5 A/cm², it is observed in Figure 42, that at high current density operations, the conventional cell design has a clear performance advantage over the design without flow channels. Above 1.5 A/cm², the effect of mass transport sets in, which is characterized by the diffusion overpotential (as described in Eq. 36 and Eq. 37) and the bubble overpotential from 3.5 A/cm² (Eq. 42). No significant mass transport effect could be observed for the conventional cell design at all temperatures. As can be seen in Figure 43A, changes in the cell operating temperature has an insignificant effect on the bubbles coverage and hence, the bubble overpotential in the conventional design cell. However, for the design without flow channels, the effect of mass transport can be seen from 1.5 A/cm² and it increases with current density.

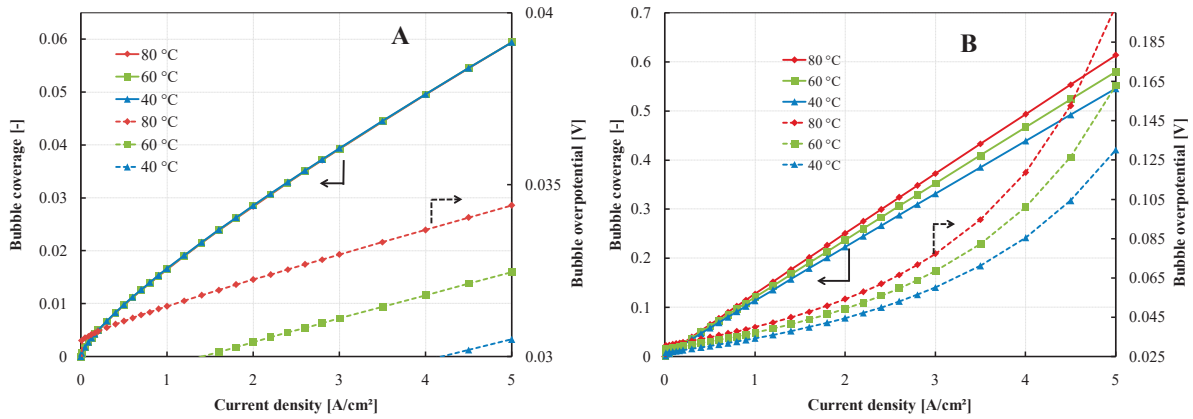


Figure 43: Effect of operating temperatures on the bubble coverage and mass transport A) Conventional design B) Alternative cell design without flow channels

For the design without flow channels, at different temperatures, the effects of mass transport become significant at $j \geq 3.5 \text{ A/cm}^2$ as it changes from diffusion overpotential which has a linear increment, to bubbles overpotential characterized by the exponential behaviour in the polarization curves. Decreasing the operating temperature reduces the mass transport losses, which is attributed to a reduced average size of the bubbles. Smaller bubbles in turn lead to a reduced surface coverage, and hence, reduced mass transport overpotentials due to bubble formation as shown Figure 43. The reduced mass transport losses at low operating temperatures could be one possible reason, apart from life-time issues, for why most commercial PEM electrolyzers operate between $50 \text{ }^\circ\text{C}$ and $60 \text{ }^\circ\text{C}$. Under similar operating conditions, Fritz [25] reported the onset of mass transport limitations to be at a current density of $j \sim 2.5 \text{ A/cm}^2$.

6.5.2 Feed water flowrate

The effect of feed water flowrate on the cell performance for both cell designs is compared in Figure 44A. It can be observed that varying the feed water flowrate in the range studied (0.6, 0.4 and 0.2 l/min) led to no changes in the performance of the conventional cell design. Meanwhile, strong mass transport limitation, due to bubbles coverage, can be observed in the cell without flow channels for 0.4 and 0.2 l/min feed water flowrates.

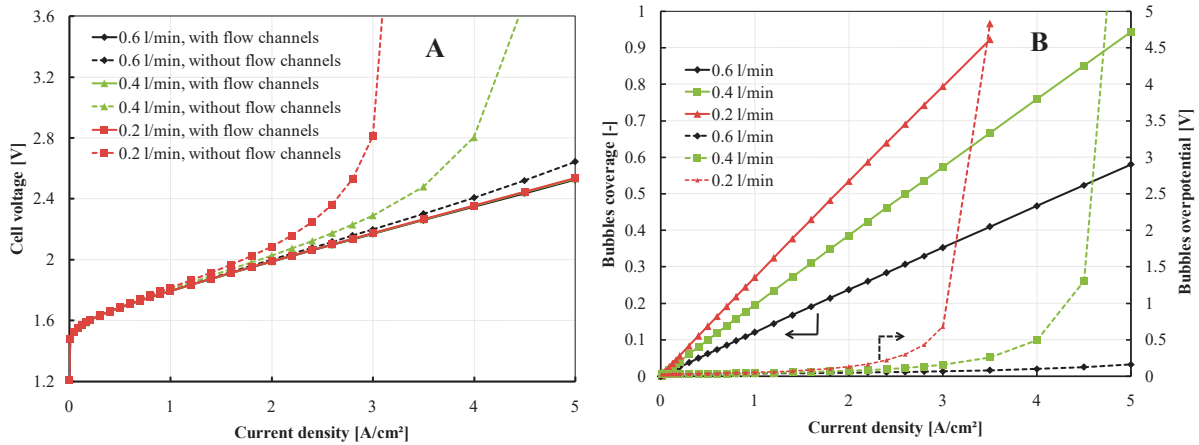


Figure 44: Effects of water flowrate A) Comparison of the calculated water flowrate dependent polarisation curves for the conventional and alternative cell design concepts. Both models were simulated at 1 bar operating pressure and at 80 °C, B) Calculated effect of the bubbles coverage on bubbles overpotential (for the alternative cell design only)

The water flowrate has a combined effect on water starvation and on the surface coverage. Figure 44B shows the calculated results of bubble coverage and the predicted bubble overpotentials due to this combined effect as a function of current density. The surface coverage of the bubbles increases significantly with decreasing feed water flowrate, resulting in high mass transport overpotentials at high current densities. It can therefore be seen that the bubble overpotential is directly related to the surface coverage.

The model was further simulated for feed water flowrates below 0.2 l/min, to predict the onset of mass transport limitation in the conventional cell design, and the result is shown in Figure 45A. It can be seen that, a significant mass transport effect starts to build up at 0.05 l/min feed water flowrate, although the mass transport loss is solely in the form of diffusion overpotentials, as can be deduced from the linearity of the 0.05 l/min polarization curve.

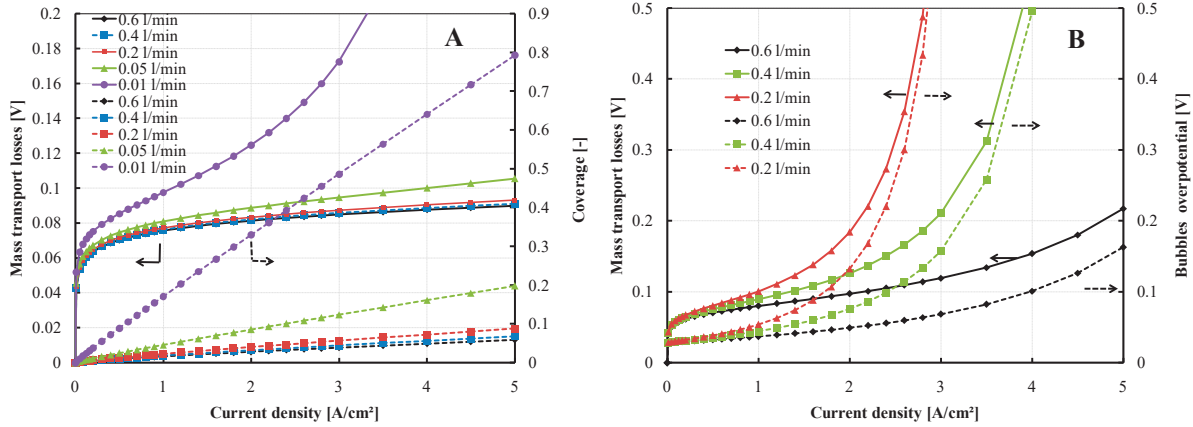


Figure 45: Effects of water flowrate on mass transport losses A) Conventional design B) Design without flow channels

However, further lowering the feed water flowrate in the conventional design to 0.01 l/min, a strong showing of mass transport is observed, mainly as a result of bubbles overpotential as deduced by the exponential nature of the characteristics curve for 0.01 l/min.

The mass transport loss is a sum of the diffusion overpotential and the bubble overpotential. In Figure 45B, the diffusion overpotential can therefore be seen as the gap (difference) between the mass transport losses and the bubble overpotential. It can also be read from the same figure that, at low water flowrates (e.g., 0.4 and 0.2 l/min, in the cell design without flow channels) and high current densities (above 2 A/cm²), the cell performance is completely mass transport, and especially, bubble overpotential controlled.

The water-to-gas ratio, ζ see Eq. 46, at the PTL|catalyst layer interface is also a critical aspect in the determination of the optimal operating conditions of a PEM water electrolysis cell. It is reported that a volumetric water-to-gas ratio of 1 can be sufficient for cell operation [48]. However, Dedigama [96] also reported that a water-to-gas ratio of 5 is necessary for optimal heat and water management, and the adequate humidification of the membrane. With the latter recommendation, the optimal operating current density can be predicted by the models for the different cell designs and water flowrates.

Figure 46 shows the predicted effect of the inlet water flowrate on the water-to-gas and the pore-to-bubble ratios.

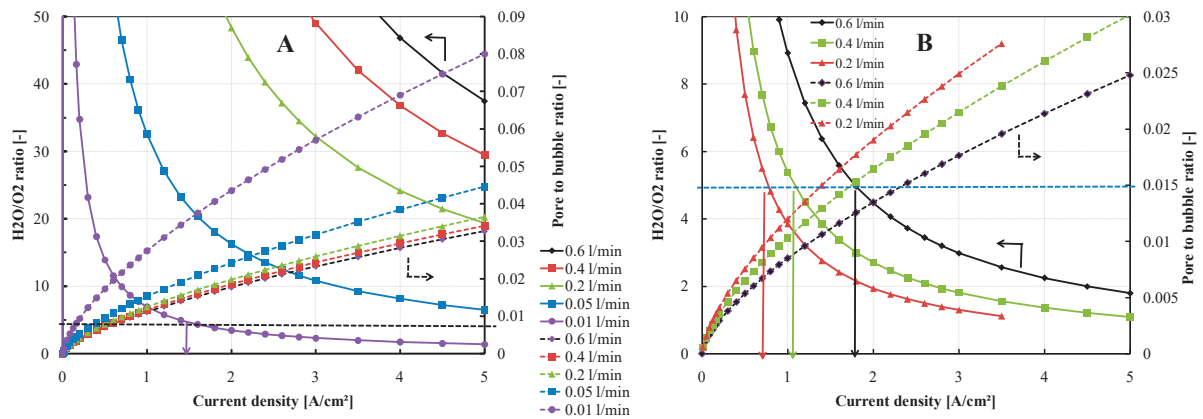


Figure 46: Effects of water flowrate on the water-to-gas ratio at the active surface and the pore-to-bubble ratio. Recommendation for the maximum operating current density at the defined flowrates A) Conventional design B) Design without flow channels

Based on these results, for a 25 cm² active area cell, the optimal operating current densities were determined to be: 0.75, 1.2 and 2 A/cm², corresponding to water flowrates of 0.2, 0.4 and 0.6 l/min, respectively, for the cell design without flow channels and the chosen cell components. However, for the conventional cell design, even water flowrate as low as 0.05 l/min is expected to be good enough for adequate heat and water management for operations at current densities up to 5 A/cm². But for a feed water flowrate of 0.01 l/min, the optimal operating current density for the conventional design will be limited at close to 1.5 A/cm². It can therefore be concluded that, the feed water flowrate is more critical to the operation of a PEM electrolysis cell without flow channels than the conventional cell design with flow channels.

Dedigama [96] used high speed photography technique in an optically transparent cell with flow channels to experimentally determine that the bubbles size and hence bubble coverage and even without quantifying the bubble overpotential, concluded qualitatively that it decreases significantly with increasing water flowrates, leading to increasing bubbles and mass transport overpotentials at low water flowrates. Using a bubble visualization technique, Tanaka [95] could also demonstrate that the bubbles size is inhibited by increased flow of the electrolyte by

preventing the coalescence of small micro bubbles. Those results corroborate these herein reported and the same trend but stronger effect is observed for the design without flow channels. This is because bubbles have much space for growth in the absence of a water stream.

In the literature, mass transport and bubbles overpotentials in the conventional cell design is usually attributed to the two-phase flow in the channels, i.e., the distortion of water flow and the flow pattern in the channels. This approach however, doesn't explain or account for the shielding of the electrodes surface by bubbles.

6.5.3 Cell operating pressure

The comparison of the calculated effect of pressure dependency on the conventional cell design and the design without flow channels is shown in Figure 47. The model predicts a decrease in performance with increasing pressure at low current densities, and an improvement in performance with increasing pressures at high current densities for the design concept without flow channels. These behaviours are consistent with experimental results, and with the results reported by [144] as shown in Figure 48. In the conventional design though, these differences kind of balance out and no significant difference in cell polarization is realized by either increasing or decreasing the cell operating pressure. That is because the increase of thermodynamic cell voltage with increasing operating pressures is compensated by mass transport losses improvement at high pressures due to the smaller nano-bubbles resulting in less bubbles shielding. This result predicted by the model is also corroborated by the published experimental findings of Suermann [145]. These results contradicts Han [139] whose performance model of a conventional designed cell showed a steady increase in cell voltage with operating pressures. Han reported at 1.5 A/cm² an increase in operating pressure from 1 bar to 5 bar corresponding to a 0.5 V increase. This is because Han modelled only the pressure effect on the open cell voltage and did not consider shielding and bubble effects. So his

conclusion that the cell performance would worsen with increasing operating pressures is only valid at very low current densities.

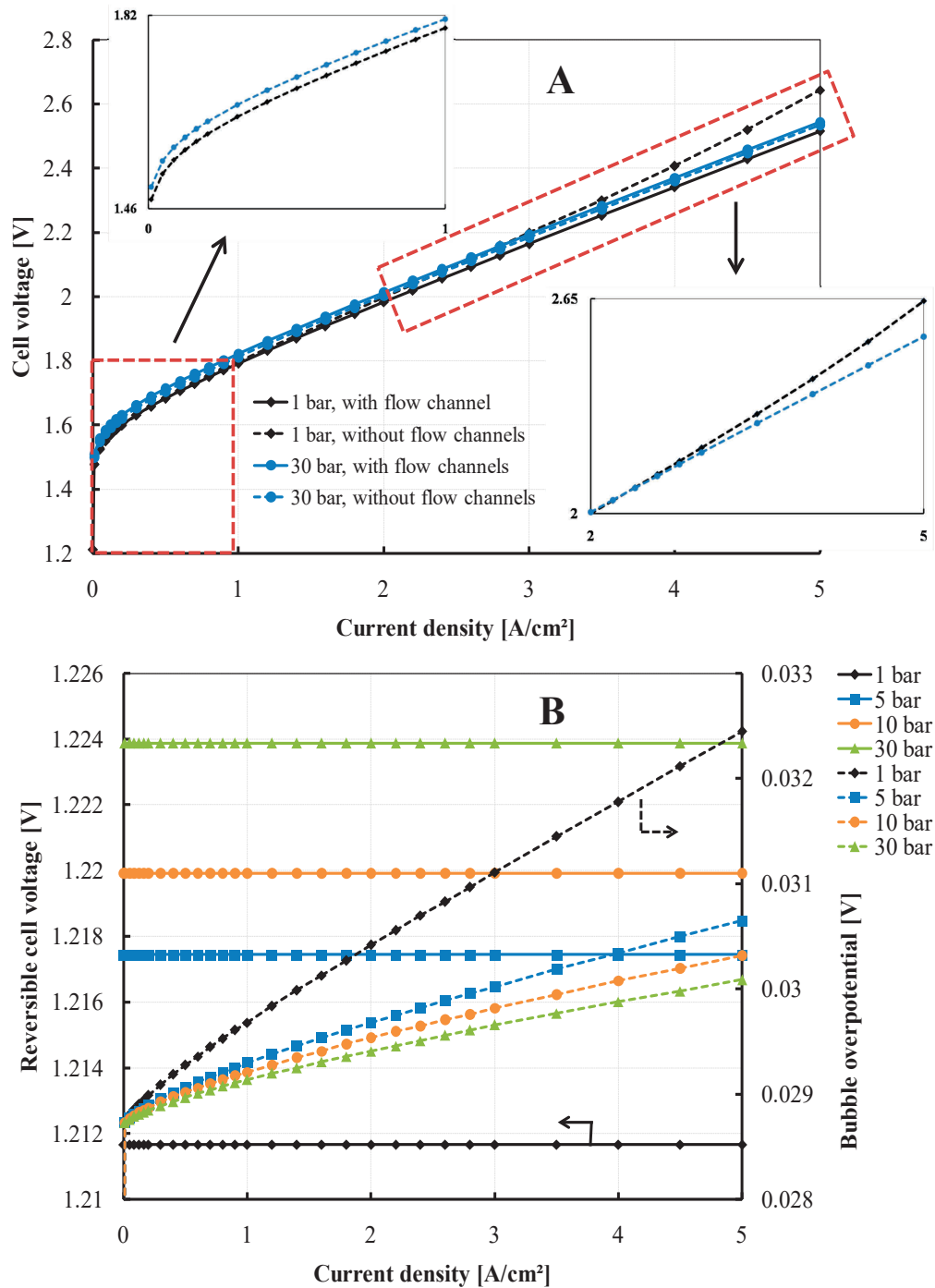


Figure 47: Effects of operating pressure A) On the performance of both design concepts B) On the reversible cell voltage and bubble overpotential

The increased cell potential at higher pressures in the kinetic region of the polarization curve ($0 \text{ A/cm}^2 \leq j \leq 0.3 \text{ A/cm}^2$) is a Nernstian effect whereby, the reversible cell potential increases

with increasing pressure, however, lower potentials, obtained for higher pressures at higher current densities, are related to mass transport effects and the bubble coverage, as shown in Figure 47B and Figure 48. At higher operating pressures, the sizes of bubbles are smaller and therefore the shielding effect reduces and the bubble overpotentials too. It can also be observed from Figure 47A, that the effect of pressure at 1 bar and at high current densities in the cell design without flow channels seems to have been overestimated by the model. A reason for this overestimation is not quite clear though.

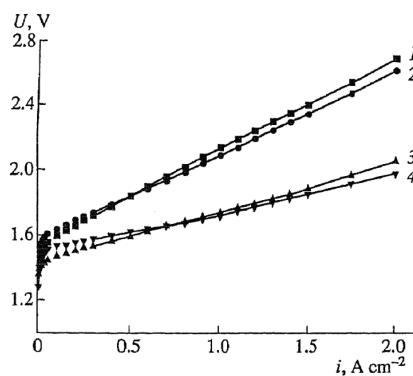


Figure 48: Effects of the operating temperature and pressure on the cell performance as reported by [144]. Polarisation curves are calculated at temperatures (1, 2) 30 °C and (3, 4) 90 °C and pressure (1, 3) 1 bar and (2, 4) 25 bar. For a conventional cell design

At high current densities ($j \geq 3$ A/cm²), the size of the bubbles decreases with increasing pressures leading to lower surface shielding and thus lower cell voltage. This means that the operation of a PEM water electrolysis cell at higher pressures is not only beneficial for lowering the cost of the balance of plant (BoP) (gas drying and subsequent compression), as has been widely reported in the literature [146–148], but also for the performance gain which can be realized at high current densities.

Another considerable effect of operating pressure on the performance of a PEM water electrolysis cell is the differential pressure across the MEA, which may lead to gas crossover (oxygen to the cathode side and hydrogen to the anode side). When this happens, a recombination reaction may be triggered, which can lead to a significant increase in the cell voltage [149]. This phenomenon has however, not been considered in this work.

6.6 Effects of the PTL microstructure

The developed coupled models were simulated to predict the effects of the titanium sintered PTL microstructure (porosity and mean pore size) on the performance of the two cell design set-ups. The findings will be presented in this section and discussed in terms mass transport limitation on the cell polarization. The cell design without flow channels and the conventional cell designs will be compared in terms of the PTL microstructure.

6.6.1 Porosity of the PTL

Models were simulated with varying PTL porosities of 20, 40 60 and 80 %. In terms of cell polarization, no significant effect on PTL porosity was observed for either the conventional cell or the cell design without flow channels.

The porosity of all the PTLs used in the experiments was 40 %. Figure 49A shows the effect of PTL porosity on the cell performance. It can be seen that, for a PTL with fixed pore diameter, the porosity of the PTL does not lead to any significant changes in the overall cell performance. Using a unitized reversible fuel cell (with flow fields), Hwang [150] also experimentally determined that the effect of porosity is not significant when the mean pore size of the PTL is smaller than 60 μm . The results of this work also corroborate the experimental findings of Ito [151].

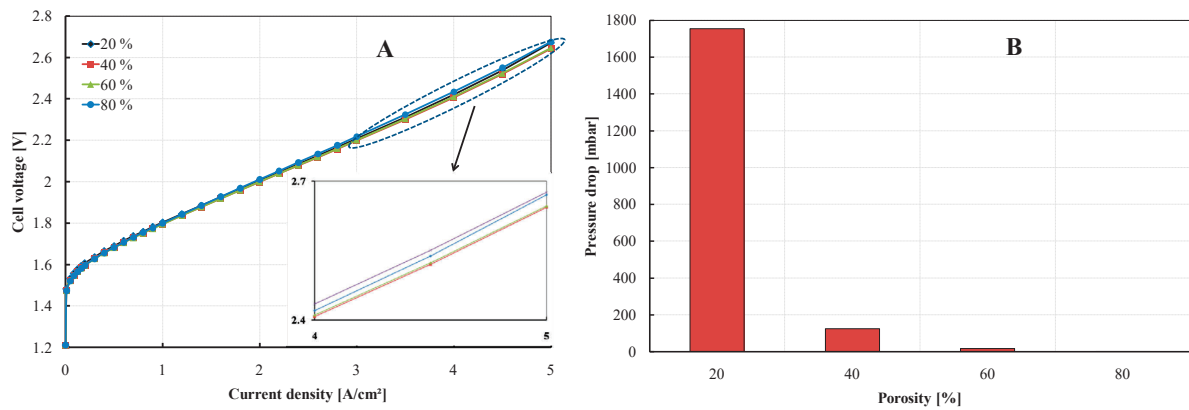


Figure 49: Predicted effect of porosity shown for the design without flow channels A) on the cell performance B) on the pressure drop across the cell calculated at 80 °C and 0.6 l/min water flowrate.

In the case of the design without flow channels, the porosity of the PTL, however, can be critical to the size of the pump and the amount of energy required in maintaining an adequately low pressure drop across the cell, while supplying the design feed water flowrate. The results of the simulated pressure drop for a cell without flow channels for different pore sizes are presented in Figure 49B. This is however not the case for the conventional design in which low pressure drop, less than 100 mbar was predicted for all PTL porosities simulated. This is because, for the conventional cell design, lateral flow through the cell from inlet to outlet is due to free flow through the machined channels. Meanwhile, for the design without flow channels, water flow through the cell from inlet to outlet is through the porous PTL. Therefore, in terms of pressure drop across the cell and the capacity of the peristaltic pump to maintain the water circulation in the cell, the PTL is more critical to the cell design without flow channels than in the conventional cell design.

Also, Figure 49A shows that the cell performance with 80 % porous PTL is slightly lower than the performance with 60 % porosity at high current densities. This is because the electrical conductivity of the PTL decreases with increasing porosity, Eq. 49, indicating higher ohmic losses due to more resistive transport of electrons. The optimal PTL porosity is about 60 %, which again corroborates with the findings of [151]. Increasing the porosity above 60 % may improve the pressure drop but will also greatly compromise the mechanical stability of the

PTL, especially for high pressure operations where the clamping torque is expected to be higher.

6.6.2 Mean pore size of the PTL

To predict the influence of the pore size on the cell performance, different PTL pore sizes from 5 to 30 μm were simulated as shown in Figure 50A for both cell designs. No significant effect of PTL pore size on the cell performance was predicted for the conventional cell design, for all pore sizes simulated. For the design without flow channels, a strong decrease in the cell performance in the mass transport region can be observed for a 5 μm mean pore size. However, no significant improvement in performance is seen with pore sizes ≥ 11 μm . Based on experimental findings, Grigoriev [71] reported the optimal pore size for sintered titanium PTL between 12 – 13 μm , although pore sizes below 10 μm were not tested. This can be explained in terms of the pore-to-bubble ratio and the bubbles overpotential, as shown in Figure 50B. Smaller pores of the PTL are easily covered and shielded by bubbles, therefore restricting the availability of reactant water for the electrolysis process.

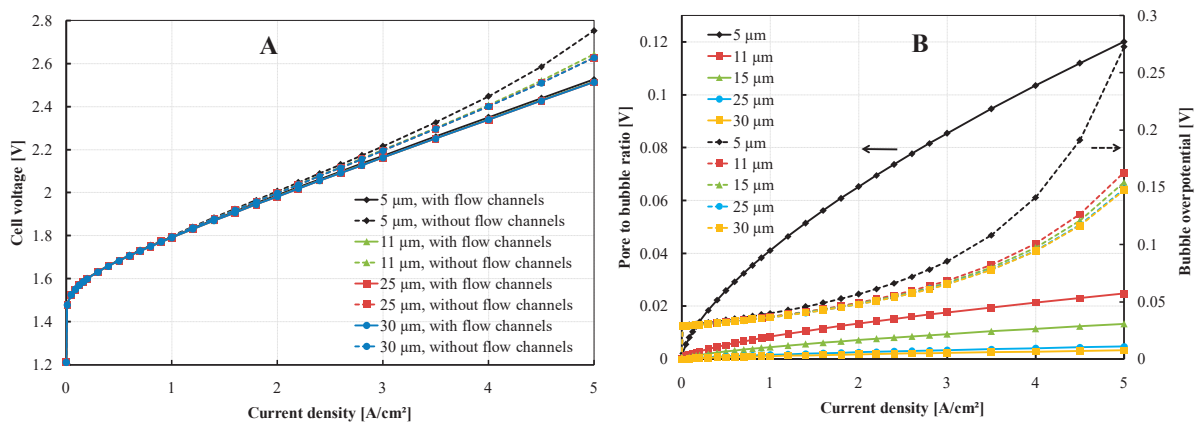


Figure 50: Effects of the PTL mean pore size (baseline PTL) A) Comparison of the calculated effect on the cell polarisation for both design setups. B) Effect on mass transport and bubbles overpotential (for design without flow channels only)

In the case of the conventional cell design with flow channels, where there is adequate water supply, the bubbles are much smaller and hence the pore to bubble ratio. This explains why there is no significant effect of pore size on the polarization of the conventional cell.

With regards to pore size dependency, [71] also suggested that, the contact pressure at the interface between the catalyst layer and the PTL can be affected by the PTL pore size and with it, the kinetics of the water splitting reaction. Very large pores may reduce the number and area of contact points between the PTL and the electrode, leading to slower kinetics and greater ohmic loss. However, [137] concluded that, the difference in the electrical resistance and contact due to changes in the pore size is negligibly small when the mean pore size is less than 50 μm , so that the ohmic and activation overpotentials due to the pore size variation become negligible. Also, for catalysts with high exchange current densities such as the one used in this work, the kinetics is so fast and dominated by the electrocatalysts, so that, the effects of pore sizes on the activation overpotential becomes minimal. Moreover, effect of the number of contact points and thus, the effective area of contact was not considered in the model, since the distribution of the clamping pressure over the active area was assumed to be optimal.

6.7 Effects of design parameters

Simulations were performed with the validated coupled models to study the effects of the cell's geometrical (design) parameters on the cell performance, for both the conventional and the cell design without flow channels. The design parameters investigated are; the PTL thickness (for both cell set-ups) and the flow channel width and height for the conventional design only. In this case, the channel geometry was not varied and only parallel channel was considered. The results are presented and discussed in this section.

6.7.1 Thickness of the PTL

The thickness of the porous transport layer is an important design parameter for an electrolysis cell because of potential manufacturing limitations and the associated costs. Figure 51A compares the effect of varying the PTL thickness (0.5, 1, 1.5 and 2 mm) on the cell polarization for both cell designs.

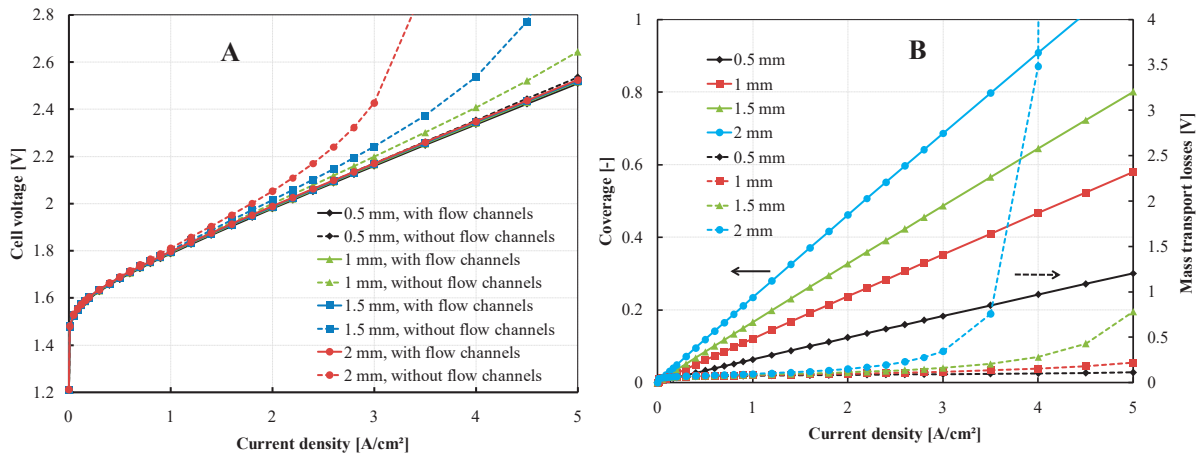


Figure 51: The calculated effect of PTL thickness on A) the cell performance, comparing both cell designs and B) on the surface coverage and mass transport losses (for the design without flow channels only)

It can be seen that, while there is no effect of PTL thickness on the performance of the conventional cell design, the cell performance decreases significantly with increasing PTL thickness for the design without flow channels. It can further be observed that, in the design without flow channels, the mass transport limitation is completely eliminated with a PTL thickness of 0.5 mm. This decrease in the performance with thicker PTL at a given PTL microstructure is attributed mainly to two factors: 1) the slower flow of water reaching the catalyst layer interface, which reduces the water-to-gas ratio, and 2) the longer diffusion pathway for the dissolved gasses, which facilitates the accumulation of gasses at the reaction interface and thus the size of the gas nano-bubbles, as shown in Figure 51B and Figure 52.

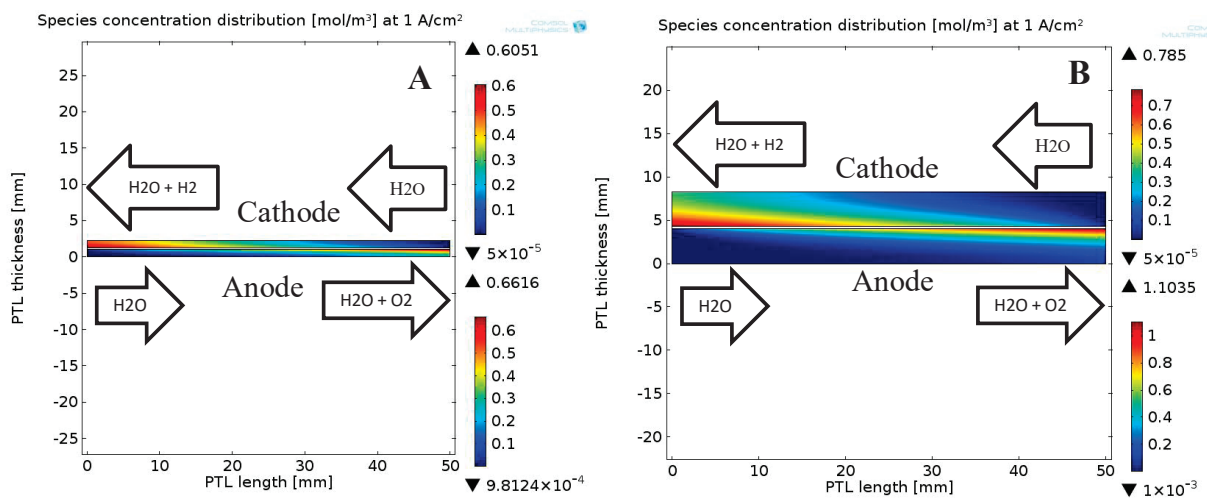


Figure 52: Concentration distribution of dissolved gasses in the PTL in the design without flow channels at 1 A/cm², 1 bar and 0.6 l/min water flowrate A) For a 1 mm thick PTL B) for a 4 mm thick PTL

Figure 52 shows a surface plot of the calculate distribution of species concentrations in the porous PTL of the cell design without flow channel. It can be seen that, for the thin PTL (1 mm), the maximum concentration of dissolved oxygen at the PTL|catalyst layer interface on the anode side is 0.6 mol/m^3 . While for the thicker (4 mm) PTL, the oxygen concentration at the PTL|catalyst layer interface is much higher at 1 mol/m^3 , due to the slower flow of water reaching the interface and the longer diffusion pathway for dissolved oxygen. The combination of these effects causes an increase in the surface coverage and decreased water access with increasing PTL thickness and with it an increase in the bubbles related mass transport overpotential.

The spatial distribution of dissolved gasses in 4 mm thick PTLs is compared for the conventional and the cell design without flow channels in Figure 53. It can be seen that the concentration of dissolved gasses at the PTL|catalyst interface is stronger in the cell without flow channels (3 mol/m^3 oxygen on the anode) than in the conventional cell design (2.5 mol/m^3 oxygen in the anode).

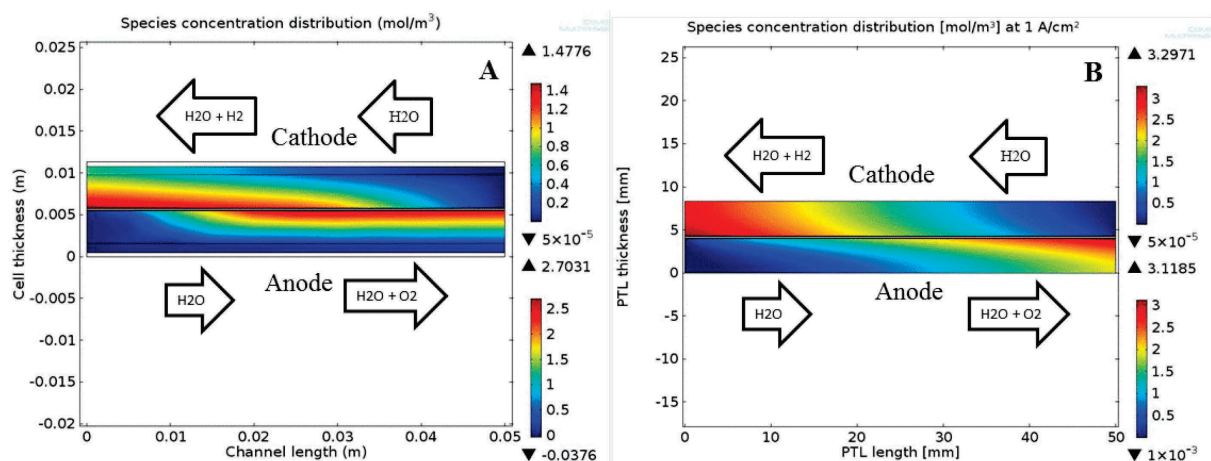


Figure 53: Calculated distribution of the dissolved gasses inside the cell, operating at 1 A/cm^2 with 4 mm thick PTL for A) the conventional design and B) the design without flow channels. Water flowrate of 0.01 l/min was used in both models to highlight the distribution.

This is as a result of the fast evacuation of gasses in the conventional cell design due to the fast stream of free flowing feed water through the channels although the diffusion pathway for

dissolved gasses is the same for both cell set-ups. Also, the water-to-gas ratio ζ is much higher in the conventional cell design. Therefore, at very low feed water flowrates, lower than 0.05 l/min, increasing the PTL thickness in the conventional cell design will start to have a negative effect on the cell performance.

The effect of varying the PTL thickness on the polarization of a PEM electrolysis cell has not been explored in the literature. Han [139] also numerically determined that the cell performance worsens by increasing the PTL thickness and attributed the findings to increase in diffusion and ohmic losses with increasing PTL thickness.

6.7.2 Channel dimensions

The channels dimensions studied are the channel width and height. Figure 54 shows a schematic of the assembling of the internal cell components, indicating the width and height of the channels. The baseline channel dimension for the test cell studied is 1 mm by 1 mm (width and height). To investigate the effects of the flow channels dimension on the cell performance, predictive polarizations were calculated by; 1) varying the channel width while keeping the height and the feed water flowrate constant, 2) varying the channel width while holding the width and the water flow rate constant.

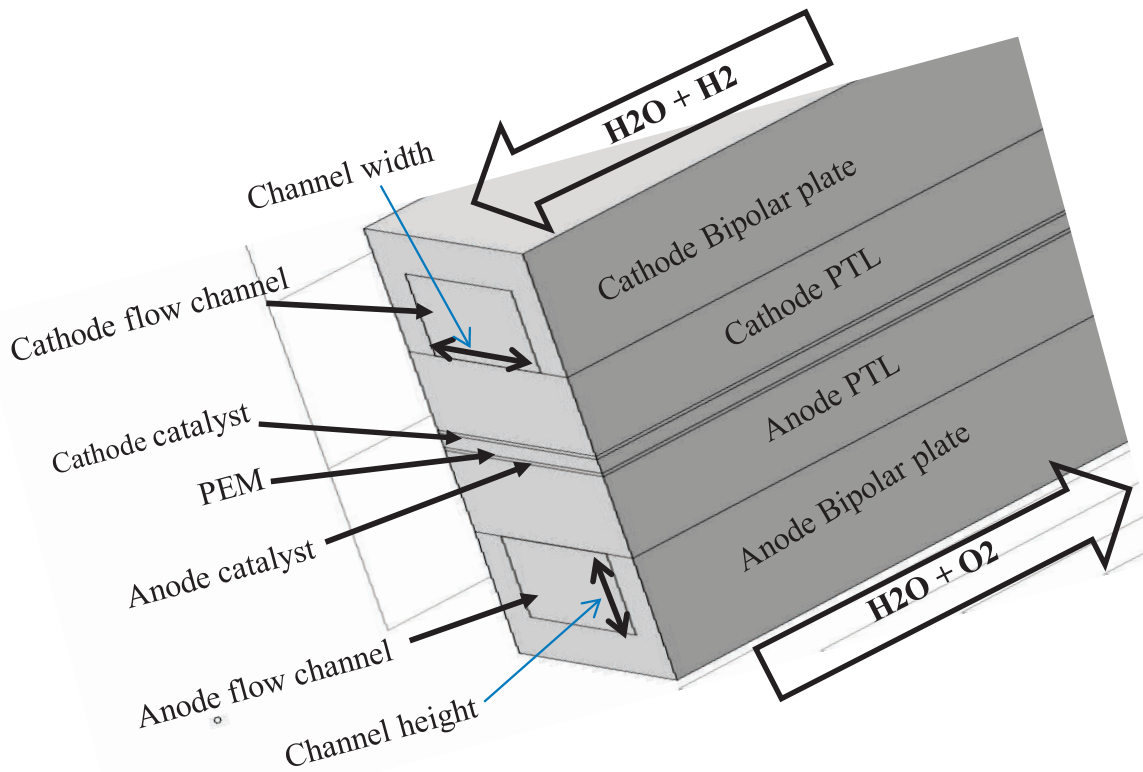


Figure 54: A 3-D cross section of cell showing the channel dimensions

As can be seen in Figure 55 and Figure 56, changing the width and the height of channels have exactly identical effect on the cell polarization. At optimal feed water flowrate of 0.6 l/min, no impact on the cell polarization is predicted by changing both the width and height of the channel (0.5, 1.5 and 2 mm).

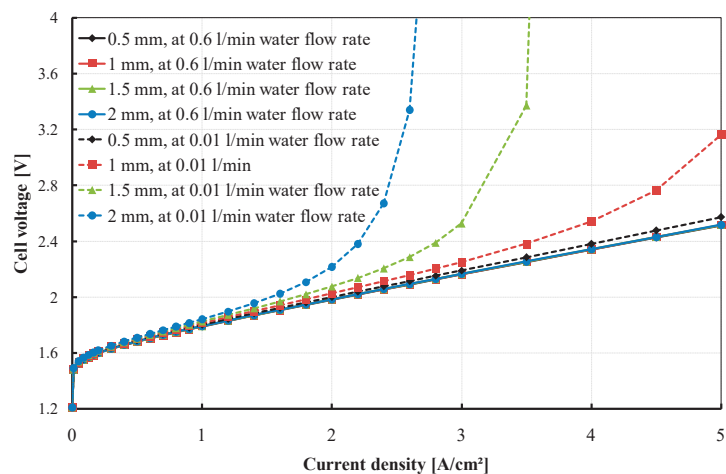


Figure 55: Effect of channel width on the performance of cell operating at 60 °C and 1 bar

However, the cell polarization becomes very sensitive to the channel dimension when the feed water flow rate is reduced to lower than 0.1 l/min. At less than optimal feed water flowrate, increasing either the channel width or height worsens the cell performance and vice versa. This is because, at low water flowrate, increasing the size of the channel decreases the velocity of water through the cell and therefore decreasing the rate of evacuation of produced gasses from the active surface. The increased build up of gas in the cell is the source of the mass transport overpotential. Also, with larger channels, the amount of reactant water reaching the active area reduces, leading to a low water-to-gas ratio ζ , which in turn, leads to an increase in the size of bubble, further increasing the mass transport impediment.

When the channel width and/or the height is reduced to 0.5 mm, even at very low feed water flowrate of 0.01 l/min, no mass transport limitation is seen, and the cell voltage is increased only by 55 mV even at the very high current density of 5 A/cm², compared to the baseline cell dimension and the optimal feed water flowrate of 0.6 l/min.

However, maintaining the feed water flowrate at 0.01 l/min while increasing the channel width and/or height reveals a strong reverse effect on the cell polarization due to bubble overpotential and mass transport. With a channel width or height of 1 mm, mass transport and bubble limitations is observed from 3.5 A/cm² operating current density and at 5 A/cm² a cell voltage increase of 0.6 V is predicted, compared to 0.5 mm channel dimensions.

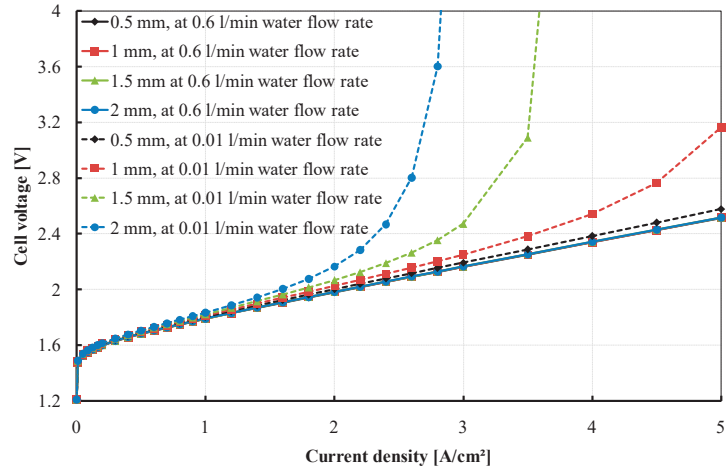


Figure 56: Effect of channel height on the performance of cell operating at 60 °C and 1 bar

When the channel width and/or height is further increased to 1.5 mm and 2 mm, the onset of mass transport and bubble overpotential is predicted at about 2 A/cm² and 1.5 A/cm² respectively. Consequently, the maximal operating point at these channel dimensions and water flowrate is predicted to be about 3.5 A/cm² and 2.7 A/cm² respectively.

The effects of channel dimension on the polarization of a PEM water electrolysis cell has not been covered in the literature. Nie [152] as well as Lee [149] have investigated on the 2-phase flow regime in different geometries (parallel, serpentine, pin hole channels) of the flow field plate of a PEM water electrolysis cell but were short of predicting the impact on cell performance. However, significant work has been reported on the effect of channel dimensions on the performance of PEM fuel cells, from which inferences can be drawn.

Guvelioglu [153] determined that the effect of channel dimension of a PEM fuel cell becomes important at high current densities and that; smaller channel width and height are required for generating high current densities and attributed these findings to reduced mass transport limitations. In an attempt to improve PEM fuel cell performance by optimizing the channel dimensions, Kumar [154] determined the optimal channel width and height to be both 1.5 mm each at optimal gas flowrate. While, Watkins [155] suggested that the channel width and height

should be about 1.14 mm and 1.02 mm respectively. However, all these studies are unanimous on the increase of mass transport limitation with increasing channel width and height.

Based on this work and results reported in the literature, it can be concluded that, mass transport limitation in a PEM water electrolysis cell can be avoided at a fixed feed water flowrate by reducing the flow channel width and height. However, manufacturing flow field plates with narrow channels by machining or casting can be very costly. Another disadvantage of a flow field plate with very narrow channels could be the possible presence of sharp contours that may compromise the mechanical stability or structure of the MEA when there is inhomogeneity of the clamping pressure, especially at high pressure operations when a large clamping torque is imperative for optimal contact and sealing.

6.8 Comparison of the performances of both cell designs

In this section, the performances of both cell designs will be compared; qualitatively with respect to the operating conditions, PTL microstructure and design parameter, and quantitatively in terms of the contribution of individual reversible and irreversible losses to the polarization of each cell.

Table 13 compares the performance of both cell designs studied as a qualitative summary of the results presented and discussed above.

Table 13: Qualitative comparison of the performance of both cell designs based on the operating conditions, PTL microstructure and design parameters.

	Conventional design	Design without flow channels
Operating temperature	<ul style="list-style-type: none"> - No mass transport limitation on performance for all temperatures investigated 	<ul style="list-style-type: none"> - Strong bubble overpotential related mass transport limitation at high current densities. - Bubble overpotential increases with increasing operating temperature
Feed water flowrate	<ul style="list-style-type: none"> - No significant effect on cell performance for water flowrates of 0.6, 0.4 and 0.2 l/h - Cell performance only becomes sensitive to water flowrates when the flowrate is below 0.01 l/min - Bubble overpotential becomes dominant at low water flowrates and decreasing water flowrate decreases cell performance. 	<ul style="list-style-type: none"> - Cell performance is more sensitive to water flowrates below 0.6 l/min. - Strong bubble over potential controlled mass transport limitation increases with lower feed water flowrates.
Operating pressure	<ul style="list-style-type: none"> - Increasing or reducing the operating pressure has little significance on the cell performance at high current densities. 	<ul style="list-style-type: none"> - Increasing the operating pressure improves the cell performance at high current densities due to smaller nano-bubbles which accounts for reduced surface coverage.

PTL porosity	<ul style="list-style-type: none"> - No significant effect on the cell performance - No significant effect on the pressure drop from the cell water inlet to outlet. 	<ul style="list-style-type: none"> - No significant effect on the cell performance - Pressure drop along the cell from inlet to outlet increases with decreasing PTL porosity
PTL pore size	<ul style="list-style-type: none"> - No significant effect on the cell performance 	<ul style="list-style-type: none"> - No significant effect on the cell performance when the mean pore size $\geq 11 \mu\text{m}$ - Strong bubble overpotential related mass transport limitation when the pore size $< 10 \mu\text{m}$. Cell performance reduces with reducing mean pore size
PTL thickness	<ul style="list-style-type: none"> - No effect on cell performance for all the PTL thicknesses studied 	<ul style="list-style-type: none"> - Increasing the PTL thickness decreases the cell performance at high current densities
Channel width	<ul style="list-style-type: none"> - Most sensitive at low feed water flowrate operation - Increasing the channel width decreases the cell performance 	<ul style="list-style-type: none"> - Not applicable
Channel height	<ul style="list-style-type: none"> - Same effect as channel width 	<ul style="list-style-type: none"> - Not applicable

6.9 Summary of all the reversible and irreversible losses

The contribution of the reversible cell voltage and each of the irreversible losses to the total cell polarization is summarized in Figure 57, Table 14 and Table 15. In both cell designs, it can

be observed that, the ohmic overpotential due to proton transport through the membrane accounts for the most significant source of voltage losses, followed by the OER activation losses at the anode. However, at high current densities ($\geq 3 \text{ A/cm}^2$), the effect of mass transport overpotentials (largely due to bubbles and water starvation) becomes a very significant source of performance loss, for the design without flow channels Figure 57B. The total mass transport losses arise from the sum of the diffusion and bubble overpotential.

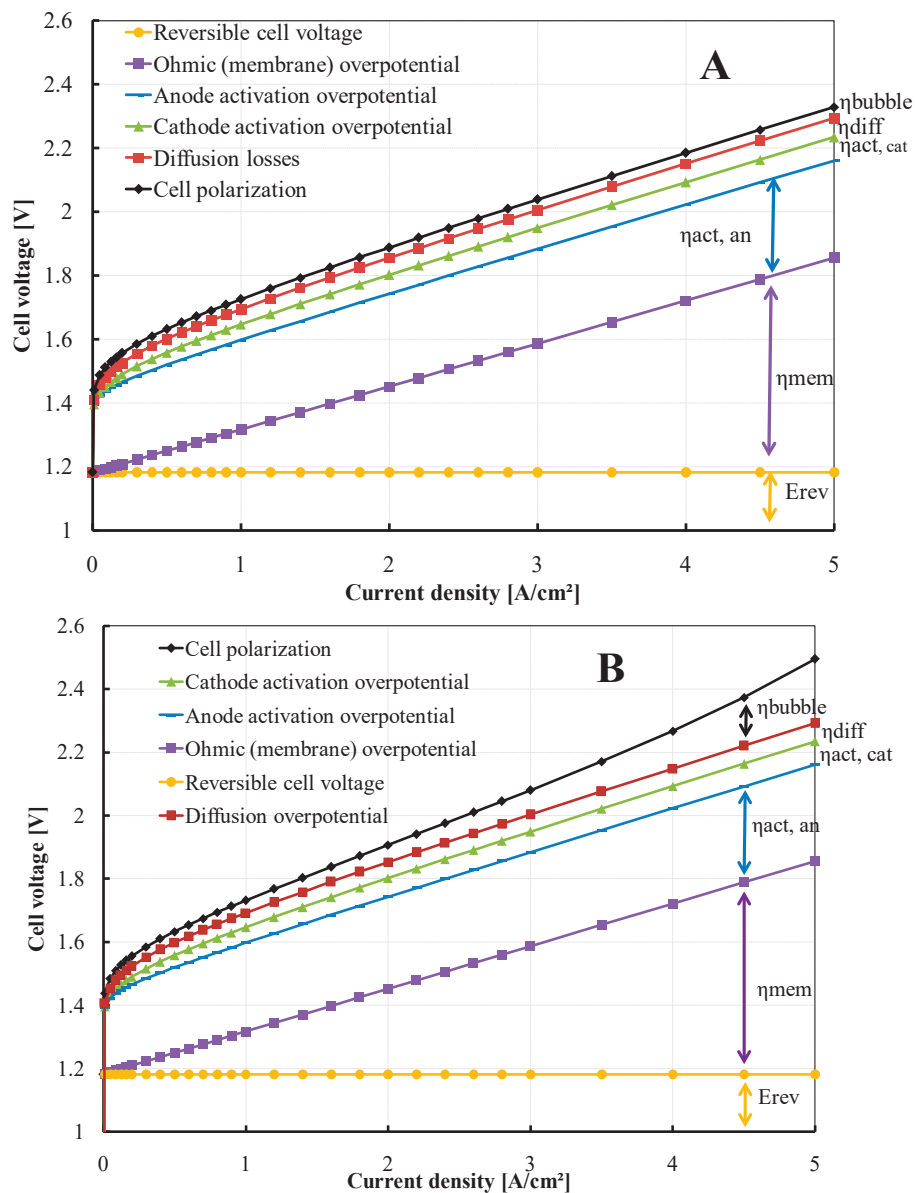


Figure 57: Summary of the predicted contribution of all irreversible losses to the cell polarization. Operating conditions for simulation: 80 °C, 1 bar and 0.6 l/min water flow rate. PTL properties are 1 mm thickness, 40 % porosity with 11 μm mean pore size A) Conventional design B) Design without flow channels

It can be concluded from Figure 57 that, the major advantage of the conventional cell design over its channel-less counterpart in terms of performance, lies in the high current density mass transport region. Otherwise, no significant difference in the cell performance in terms of ohmic or activation overpotentials can be predicted between both cell designs for operating current densities up to 5 A/cm².

While the percentage contribution of the anode overpotential to the cell voltage losses decreases with increasing current density (16.2, 14.4 and 12.1 % of total loss at 1, 3 and 5 A/cm², respectively, the contribution of the ohmic overpotential due to the membrane increases steadily with current density (7.7, 19.2 and 27.0 % of total loss at 1, 3 and 5 A/cm², respectively), and these effects are reflected the same for both cell concepts. Table 14 and Table 15 summarize all of the reversible and irreversible voltage losses as a percentage of the total cell voltage for the conventional cell design and for the cell without flow channels respectively.

Table 14: Summary of all reversible and irreversible losses as a percentage of the total cell voltage, at different current densities. Simulated at 80 °C, 1 bar and 0.6 l/min water flow rate, with the baseline PTL properties. For the conventional cell design.

	Current density 1 [A/cm ²]		Current density 3 [A/cm ²]		Current density 5 [A/cm ²]	
	Losses [V]	Losses [%]	Losses [V]	Losses [%]	Losses [V]	Losses [%]
E_{rev}	1.18	68.52	1.18	57.80	1.18	50.88
η_{mem}	0.13	7.77	0.40	19.76	0.67	28.97
$\eta_{act,an}$	0.28	16.23	0.30	14.67	0.30	13.09
$\eta_{act,cat}$	0.05	2.90	0.07	3.42	0.07	3.01
η_{diff}	0.05	2.78	0.06	2.74	0.06	2.58
$\eta_{bubbles}$	0.03	1.80	0.03	1.61	0.03	1.46
V_{cell}	1.73	100.00	2.05	100.00	2.32	100.00

Table 15: Summary of all reversible and irreversible losses as a percentage of the total cell voltage, at different current densities. Simulated at 80 °C, 1 bar and 0.6 l/min water flow rate, with the baseline PTL properties. For the design without flow channels.

	Current density 1 [A/cm ²]		Current density 3 [A/cm ²]		Current density 5 [A/cm ²]	
	Losses [V]	Losses [%]	Losses [V]	Losses [%]	Losses [V]	Losses [%]
E_{rev}	1.18	68.3	1.18	56.9	1.18	47.6
η_{mem}	0.13	7.7	0.40	19.3	0.67	26.9
$\eta_{act,an}$	0.28	16.2	0.30	14.4	0.30	12.1
$\eta_{act,cath}$	0.05	2.9	0.07	3.2	0.07	2.9
η_{diff}	0.05	2.6	0.05	2.4	0.06	2.3
$\eta_{bubbles}$	0.04	2.3	0.08	3.9	0.20	8.1
V_{cell}	1.73	100.00	2.08	100.00	2.48	100.00

For the design without flow channels, the percentage contribution of the bubbles overpotential to the overall overpotential also increases significantly with increasing current density (2.3, 3.9 and 8.1 % of total loss at 1, 3 and 5 A/cm², respectively). While for the conventional cell design set-up, the percentage contribution of the bubble overpotential to the cell polarization slightly decreases with increasing current densities, standing at 1.8, 1.6 and 1.5 % at 1, 3 and 5 A/cm² respectively. This means that, even at very high current densities, the ohmic overpotential due to resistance to proton flow through the MEA is still dominating over bubble overpotential and mass transport limitation at the design and operating conditions studied.

6.10 Recommendation for low cost design and high performance cell

A PEM electrolysis cell containing bipolar plates without machined flow channels can significantly simplify cell design and reduce the manufacturing cost but can also result in other issues, especially related to cell performance compared to the conventional cell design; for example, increased pressure drop across the cell, poor water management and reduced effectiveness of bubble removal in the mass transport region. Therefore, this type of cell design places even more emphasis on the PTL microstructure and the choice of the design and operating parameters.

Generally, in order to improve PEM electrolysis cell performance in the activation region, one of the major focuses should be on improving the activity of the OER reaction by increasing the catalyst utilization. However, at mid to high current densities, improving the proton conductivity of the membrane and reducing the mass transport losses is imperative.

From this work, it has been proven that, the bottleneck to achieving acceptable cell performance in the low cost cell design without machined flow channels lies in the mass transport dominated high current density region. To achieve performances comparable to that of the conventional cell design, the mass transport losses in the low cost cell design and operating conditions can be improved by:

1. Operating the cell at 60 °C or lower, thereby, reducing the average bubbles size and shielding effect
2. Operating the cell at elevated pressures (preferably 30 bar)
3. Operating the cell at a water flowrate of at least 0.6 l/min (for a 25 cm² cell) to mitigate water starvation
4. Reducing the thickness of the PTL to 0.5 (or less) mm to shorten the diffusion pathway of dissolved gasses thus reducing the surface shielding, and better water access to the surface.

The recommendations for the 25 cm² low cost cell design to achieve comparable performance vis-à-vis a conventional PEM water electrolysis cell of same active area, with both cells incorporating the same MEA and cell component materials as used in this work is summarized in Table 16 and Figure 58.

Table 16: Recommendations for a 25 cm² active area low cost cell design without flow channels to achieve comparable performance with a conventional cell design (25 cm²) operating at current densities of up to 5 A/cm².

Parameter		Conventional cell design	Low cost cell design
Operating temperature		60 °C	60 °C
Operating pressure		1 bar	≥ 5 bar
Feed water flowrate		≥ 0.2 l/min	≥ 0.6 l/min
PTL porosity		40 %	50 %
PTL mean pore diameter		11 μm	≥ 11 μm
PTL thickness		1 mm	0.5 mm
Channel width		1 mm	Not applicable
Channel height		1 mm	Not applicable
Predicted cell voltage	@ 1 A/cm ²	1.8 V	1.81 V
	@ 3 A/cm ²	2.16 V	2.17 V
	@ 5 A/cm ²	2.51 V	2.52 V

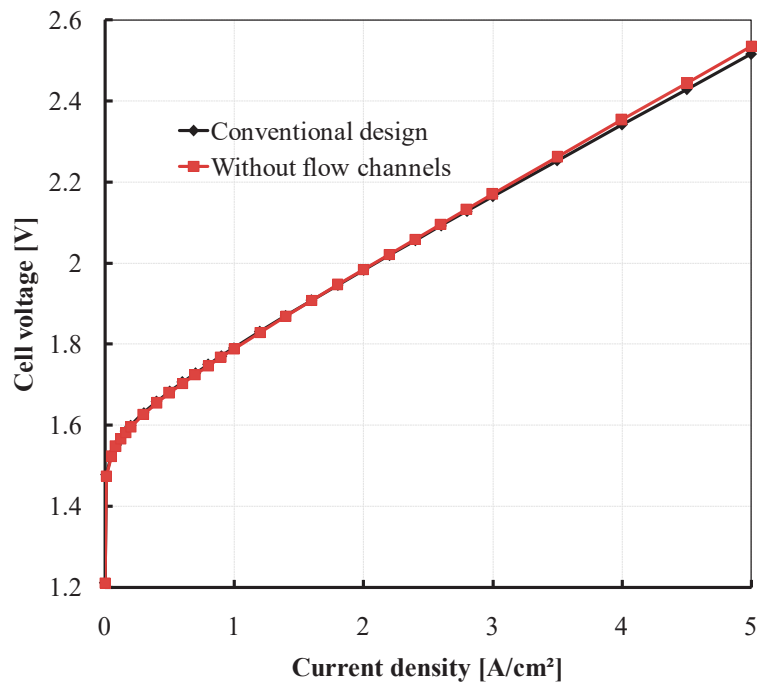


Figure 58: Comparison of the performance of the conventional cell design and the design without flow channels. Calculated based on the design, operating and PTL microstructure properties in Table 16

Chapter 7

Summary, conclusion and outlook

The production of hydrogen by PEM water electrolysis has been identified as one of the most efficient and clean form of energy storage, especially when coupled with renewable energy sources. As the outlook for hydrogen production by PEM electrolysis is geared towards costs reduction and increased production by high current density operation, so has the need for low cost and high performing materials and cell design concepts become imperative.

Extensive progress has been achieved in recent years, concurrent with the PEM fuel cell technology, on the development and manufacturing of cost effective and high performing electro-catalysts and proton exchange membranes which together form the MEA, since the same components can practically be employed (or with minor alterations) for both technologies. However, the PEM fuel cell and PEM water electrolysis cells do not have the same flow medium (air, hydrogen and water vapour in fuel cells; and water and dissolved gasses in PEM electrolysis), so the different two-phase flow regimes in the cells informs the need for differing materials of the internal cell components such as the current collectors (PTL) and the bipolar plates, as well as the cell design. Contrary to PEM fuel cells, research on cost effective and high performing cell materials such as the porous transport layers for the OER as well as cell design, especially for high current density operation (up to 5 A/cm²) is not well advanced.

The cost model reported in this work revealed that the costs of bipolar plates (materials and production costs) can constitute up to about 50 % of a conventional PEM water electrolysis stack, hence, suggesting that the bipolar plate could present high potentials for the stack costs

reduction. In an endeavour to reduce stack costs to meet the costs targets cited in this work, an alternative cell design concept has been proposed; one in which the expensive bipolar plates with machined flow field is replaced altogether, by a 3-D porous transport layer (PTL). The costs model reported in this work further revealed that, with the proposed alternative cell design with a 3-D PTL structure, the PEM water electrolysis stack costs could effectively be reduced by up to 25 %.

Experimental polarization curves measured in a prototype of the alternative cell design with a 3-D PTL structure was compared to those measured in a conventional cell design. It was observed that, while both cells performed comparably the same in the low (activation controlled) to mid (ohmic controlled) current density regions, the conventional cell design strongly outperformed the 3-D PTL cell in the high current density region with strong mass transport limitation. With this observation, it became clear that, while the 3-D PTL cell could answer the concern of cell costs reduction it could not possibly solve the issues of good polarization performance at high current density operations. Thus, the need for further research to understand the reasons for and to find corrective measures to get the 3-D PTL cell to perform at least as good as its conventional counterpart at high current density operations.

The underlying hypothesis of this research work was that, by optimizing the microstructure and size of the 3-D PTL, as well as the operating parameters, the mass transport regime in the 3-D PTL cell could be engineered to eliminate the mass transport limitation at high current densities to achieve comparable performance with the conventional cell design. This idea therefore, constitutes the motivation and objectives on which this work was hinged.

Both coupled physics modelling and experimental approaches were used to reach the objectives of this work. Two simple but robust semi-empirical, fully coupled electrochemistry, mass transport and heat transfer models were developed, one for each cell design concept, to

predict the cell performance. The calculated polarization curves from the models were validated against polarization curves measured in-situ in test cells (one for each design concept) designed and constructed for the sake of this work. All experimental polarization curves were measured in an in-house designed and constructed test station.

The uniqueness of this work lies especially on the development of semi-empirical equations for predicting the contribution of the bubble overpotential to the mass transport limitation and the overall cell polarization, Eq. 38 through to Eq. 47; and the experimental validation of predicted polarization curves at high current densities up to 5 A/cm², using a 3-D PTL structure. The validated models can also serve as useful tool for performance engineering and up-scaling of PEM electrolysis cells and stacks.

The results reveal that, for the alternative cell design without flow channels, the operating temperature and pressure, inlet water flowrate and thickness of the 3-D PTL are the critical parameters for mitigating mass transport limitation and improving cell performance at high current densities. Increasing operating temperature decreases cell performance at high current densities due to increase in the size of bubbles and surface coverage, while increasing the operating pressure will have a reverse effect as increasing the temperature. Decreasing the feed water flowrate below 0.5 l/min increases the mass transport limitation and impedes the cell performance at high current densities. Increasing the PTL thickness is found to be detrimental to cell performance at high current densities and the optimal thickness of the 3-D PTL for the cell studied was found to be 0.5 mm at optimal operating conditions. As for the conventional cell design, the channel dimensions are found to be critical for optimal mass transport and the enhancement of cell polarization at high current density operations. Increasing the channel width and height especially above 1 mm each was found to pose a hindrance on the cell performance at high current densities.

It was further determined that, a 25 cm² active area cell without flow channels could perform as good as a conventional cell design of the same active area, with both operating at 60 °C when; the feed water flowrate is at least 0.6 l/min, the cell is operated at a pressure ≥ 5 bar, and the 3-D PTL is 0.5 mm thick with 50 % porosity and 11 μm mean pore size.

In spite of its obvious strengths and success, the scope of the models herein developed and this work in general can be expanded and improved by:

- Incorporating an ohmic resistance sub-model as described by [112]. This approach will make the model more adapted to a wide range of materials for use as bipolar plates and PTL structures, especially composite materials whose electrical conductivity is not as good as titanium. When the flow of electrons through the cell components is not infinitely fast like in titanium, the contribution of the ohmic drop due to electron flow could be significant. This approach was not considered in this work because the focus was on the mass transport limitation and the PTL and bipolar plates of the cells used were made from titanium.
- Modelling the effects of gas crossover by adopting one of the methods described in the literature, e.g., Weber [156], Thampan [157] and Schalenbach [158]. This approach will account for gas purity concerns and performance losses from parasitic currents due to recombination reactions. This was not considered in this work because gas purity was not of concern and the cells were operated at balanced pressure, thereby, reducing the likelihood of gas crossover concerns.
- Replacing the 2-D PTL model schema with a real 3-D tomographic image of the PTL. This will improve accuracy of the flow regime in the porous PTL and will take into consideration other porous structure properties such as tortuosity and powder particle

size, which were not considered in this work. However, this step will require huge computational resources, which was beyond the scope and need of this work.

- Improving the accuracy of the experimentally measured polarization curves by gold coating the surface of the bipolar plates, PTL and spacers. Additionally, the atomic layer deposition method could be used for coating the pores of the PTL. This way, the interfacial contact resistance issues will be greatly improved and the need for extra ohmic correction experiments and the little inaccuracies that may come with it will be rendered redundant.
- Further experimentally validating the model by validating the bubbles size using a high speed camera and visualization test set-up similar to those reported by Selamet [97] and others.
- Scaling up to larger cell area and stack

The state-of-the-art PTL for PEM water electrolysis and those used in this work are generally homogeneous in microstructure and pore distribution. A good idea of an optimized porous PTL to be considered could be one with different layers of microstructures and porosity gradients, with decreasing porosity from the PTL|bipolar plate interface to the PTL|catalyst layer interface. That way, the bigger pores at the PTL|bipolar plate interface will facilitate the evacuation of larger bubbles away from the cell, thus improving water flow and mass transport; while smaller pores at the PTL|catalyst layer interface will improve contact between both layers, thereby leading to improved electro-kinetics. Such a porous flow structure can be produced for example, by stacking up layers of expanded metal meshes. The use of such PTL with optimized porosity and microstructure gradient could prove the ground breaker for a cost effective cell design with acceptable performance at high current density.

References

- [1] T.N. Veziroglu, F. Barbir, Solar–Hydrogen Energy System: The Choice of the Future, *Envir. Conserv.* 18 (04) (1991) 304.
- [2] F. Barbir, PEM Electrolysis for Production of Hydrogen from Renewable Energy Sources, *Solar Energy* 78 (5) (2005) 661–669.
- [3] Y.V. Sinyak, Prospects for hydrogen use in decentralized power and heat supply systems, *Stud. Russ. Econ. Dev.* 18 (3) (2007) 264–275.
- [4] R.J. Friedland, T.M. Maloney, F. Mitlitsky, Hydrogen Fuel through PEM Electrolysis, SAE International 400 Commonwealth Drive, Warrendale, PA, United States, 2001.
- [5] J. Wright, Towards an Australian hydrogen economy, *International Journal of Environmental Studies* 63 (6) (2006) 837–843.
- [6] J.A. Turner, Sustainable hydrogen production, *Science (New York, N.Y.)* 305 (5686) (2004) 972–974.
- [7] R. de Levie, The electrolysis of water, *Journal of Electroanalytical Chemistry* 476 (1) (1999) 92–93.
- [8] M. Balat, M. Balat, Political, economic and environmental impacts of biomass-based hydrogen, *International Journal of Hydrogen Energy* 34 (9) (2009) 3589–3603.
- [9] A. KONIECZNY, K. MONDAL, T. WILTOWSKI, P. DYDO, Catalyst development for thermocatalytic decomposition of methane to hydrogen, *International Journal of Hydrogen Energy* 33 (1) (2008) 264–272.
- [10] D.M.F. Santos, C.A.C. Sequeira, J.L. Figueiredo, Hydrogen production by alkaline water electrolysis, *Quím. Nova* 36 (8) (2013) 1176–1193.
- [11] L. Barreto, A. Makihira, K. Riahi, The hydrogen economy in the 21st century: a sustainable development scenario, *International Journal of Hydrogen Energy* 28 (3) (2003) 267–284.
- [12] L.M. Gandía, G. Arzamendi, P.M. Diéguez, Renewable Hydrogen Energy, in: *Renewable Hydrogen Technologies*, Elsevier, 2013, pp. 1–17.
- [13] A.K. Colling, R.J. Roy (Eds.), High Differential Pressure, Solid Polymer Electrolysis, 1997.
- [14] J.F. McElroy, SPE regenerative hydrogen/oxygen fuel cells for extraterrestrial surface applications, in: *Proceedings of the 24th Intersociety Energy Conversion Engineering Conference*, Washington, DC, USA, IEEE, 1989, pp. 1631–1636.
- [15] H.A. Carlson, J.E. Genovese, M.H.B. Lunn, S. Cassidy, Shelf Life Experience with Solid Polymer Electrolyte Cell Stacks, 2000.
- [16] T. G. Coker, A. B. Laconti, L. J. Nuttal, Industrial and Government Applications of SPE Fuel Cells and Electrolyzers, in: *The case Western Symposium on Membranes and Ionic and Electronic Conducting Polymers*, Cleveland, Ohio, 1982.
- [17] T. Smolinka, E.T. Ojong, T. Lickert, Fundamentals of PEM Water Electrolysis, in: D. Bessarabov, H. Wang, H. Li, N. Zhao (Eds.), *PEM Electrolysis for Hydrogen*

- Production. Principles and Applications, Taylor & Francis Group, Boca Raton, USA, 2016.
- [18] J. Mergel, Hydrogen Production by Water Electrolysis: Current Status and Future Trends, Stuttgart, Germany, 2013.
- [19] K. Zeng, D. Zhang, Recent progress in alkaline water electrolysis for hydrogen production and applications, *Progress in Energy and Combustion Science* 36 (3) (2010) 307–326.
- [20] M. Wang, Z. Wang, X. Gong, Z. Guo, The Intensification Technologies to Water Electrolysis for Hydrogen Production – A Review, *Renewable and Sustainable Energy Reviews* 29 (2013) 573–588.
- [21] D.W. Green, R.H. Perry, PROPERTY CALCULATIONS FOR GASES AND VAPORS, in: *Perry's Chemical Engineers' Handbook*, Eighth Edition, McGraw Hill Professional, Access Engineering, 1934.
- [22] J. Ahn, R. Holze, Bifunctional electrodes for an integrated water-electrolysis and hydrogen-oxygen fuel cell with a solid polymer electrolyte, *Journal of Applied Electrochemistry* 22 (1992) 1167–1174.
- [23] J. Durst, A. Siebel, C. Simon, F. Hasché, J. Herranz, H.A. Gasteiger, New insights into the electrochemical hydrogen oxidation and evolution reaction mechanism, *Energy Environ. Sci.* 7 (7) (2014) 2255.
- [24] N. Perez, *Electrochemistry and corrosion science*, Kluwer Academic, Boston, London, 2004.
- [25] D.L. Fritz, J. Mergel, D. Stolten, PEM electrolysis simulation and validation, *ECS Transactions* 58 (19) (2014) 1–9.
- [26] J. Pettersson, B. Ramsey, D. Harrison, A review of the latest developments in electrodes for unitised regenerative polymer electrolyte fuel cells, *Journal of Power Sources* 157 (1) (2006) 28–34.
- [27] A. URSUA, L.M. Gandia, P. SANCHIS, Hydrogen Production From Water Electrolysis: Current Status and Future Trends, *Proc. IEEE* 100 (2) (2012) 410–426.
- [28] T. Smolinka, E.T. Ojong, J. Garche, Hydrogen Production from Renewable Energies - Electrolyzer Technologies, in: *Electrochemical Energy Storage for Renewable Sources and Grid Balancing*, Elsevier, 2015, pp. 103–128.
- [29] R. Phillips, C.W. Dunnill, Zero gap alkaline electrolysis cell design for renewable energy storage as hydrogen gas, *RSC Adv* 6 (102) (2016) 100643–100651.
- [30] D.L. Stojić, T.D. Grozdić, B. Umićević, A.D. Maksić, A comparison of alkaline and proton exchange membrane electrolyzers, *Russ. J. Phys. Chem. A* 82 (11) (2008) 1958–1960.
- [31] W. DONITZ, High-temperature electrolysis of water vapor?: Status of development and perspectives for application, *International Journal of Hydrogen Energy* 10 (5) (1985) 291–295.
- [32] M.A. Laguna-Bercero, Recent advances in high temperature electrolysis using solid oxide fuel cells: A review, *Journal of Power Sources* 203 (2012) 4–16.
- [33] M. Carmo, D. Fritz, J. Margel, D. Stolten, A Comprehensive Review on PEM Water Electrolysis, *International Journal of Hydrogen Energy* 38 (2013) 4901–4934.

- [34] N. Briguglio, V. Antonucci, Overview of PEM Electrolysis for Hydrogen Production, in: D. Bessarabov, H. Wang, H. Li, N. Zhao (Eds.), *PEM Electrolysis for Hydrogen Production. Principles and Applications*, Taylor & Francis Group, Boca Raton, USA, 2016, pp. 1–8.
- [35] Proton Energy Systems, PEM electrolysis efficiency takes a leap forward, *Membrane Technology* 2009 (5) (2009) 3.
- [36] T. Smolinka, Water Electrolysis, in: J. Garche (Ed.), *Encyclopedia of Electrochemical Power Sources*, Elsevier, Amsterdam, 2009, pp. 394–413.
- [37] S. Asghari, M.H. Shahsamandi, M.R. Ashraf Khorasani, Design and manufacturing of end plates of a 5kW PEM fuel cell, *International Journal of Hydrogen Energy* 35 (17) (2010) 9291–9297.
- [38] US Department of Energy, DOE Technical Targets for Hydrogen Production from Electrolysis, available at <https://energy.gov/eere/fuelcells/doe-technical-targets-hydrogen-production-electrolysis> (accessed on March 5, 2017).
- [39] S.A. Grigoriev, P. Millet, S.V. Korobtsev, V.I. Porembskiy, M. Pepic, Etievant. C., C. Puyenchet, V. Fateev, Hydrogen safety aspects related to high-pressure polymer electrolyte membrane water electrolysis, *International Journal of Hydrogen Energy* 34 (2009) 5986–5991.
- [40] S.A. Grigoriev, K.A. Dzhus, D.G. Bessarabov, P. Millet, Failure of PEM water electrolysis cells: Case study involving anode dissolution and membrane thinning, *International Journal of Hydrogen Energy* 39 (35) (2014) 20440–20446.
- [41] D. Bromley, Hydrogen Embrittlement Testing of Austenitic Stainless Steels Sus 316 and 316L. Master, British Columbia, Canada, 2008.
- [42] E. Tal-Gutelmacher, D. Eliezer, The hydrogen embrittlement of titanium-based alloys, *Journal of Materials Science* (2005).
- [43] H. Barthélémy, Effects of pressure and purity on the hydrogen embrittlement of steels, *International Journal of Hydrogen Energy* 36 (2011) 2750–2758.
- [44] W. Kreuer, H. Hofmann, Electrolysis: The important energy transformer in a world of sustainable energy, *International Journal of Hydrogen Energy* 23 (8) (1998) 661–666.
- [45] E.I. Zoulias, R. GLOCKNER, N. Lymberopoulos, T. Tsoutsos, I. Vosseler, O. Gavalda, H.J. Mydske, P. TAYLOR, Integration of hydrogen energy technologies in stand-alone power systems analysis of the current potential for applications, *Renewable and Sustainable Energy Reviews* 10 (5) (2006) 432–462.
- [46] M. Momirlan, T. Veziroglu, Current status of hydrogen energy, *Renewable and Sustainable Energy Reviews* 6 (1–2) (2002) 141–179.
- [47] L. Degiorgis, M. Santarelli, M. Cali, Hydrogen from renewable energy: A pilot plant for thermal production and mobility, *Scientific Advances in Fuel Cell Systems*, Turin, Italy, 13-14 September 2006 171 (1) (2007) 237–246.
- [48] H. Ito, T. Maeda, A. Nakano, Y. Hasegawa, N. Yokoi, C.M. Hwang, M. Ishida, A. Kato, T. Yoshida, Effect of flow regime of circulating water on a proton exchange membrane electrolyzer, *International Journal of Hydrogen Energy* 35 (18) (2010) 9550–9560.
- [49] J. Nie, Y. Chen, S. Cohen, B.D. Carter, R. Boehm, Numerical and experimental study of three-dimensional fluid flow in the bipolar plate of a PEM electrolysis cell, *International Journal of Thermal Sciences* 48 (10) (2009) 1914–1922.

- [50] E.T. Ojong, E. Mayousse, N. Guillet, D. Vannucci, F. Beille, T. Smolinka, Design, construction and performance of PEM electrolysis stack operating at high pressures, in: 5th International Conference on Fundamentals and Development of Fuel Cells, Karlsruhe, 2013.
- [51] S. Cohen, S. Porter, O. Chow, D. Henderson, Hydrogen Generation From Electrolysis: Final Report for DOE Award DE-FC36-04GO13030, Wallington CT, USA, February 28 / 2009.
- [52] Selamet. A.M., F. Becerikli, M.D. Mat, Y. Kaplan, Development and testing of a highly efficient proton exchange membrane (PEM) electrolyzer stack, *International Journal of Hydrogen Energy* 26 (2011) 11480–11487.
- [53] E. T. Ojong, E. Mayousse, T. Smolinka, N. Guillet, Advanced Bipolar Plates without flow channels, for PEM electrolyzers operating at high pressure, in: TECHNOPORT 2012, Trondheim, Norway, 2012.
- [54] K. Lewinski, 3M NSTF for PEM Water Electrolysis, in: D. Bessarabov, H. WANG, H. Li, N. Zhao (Eds.), *PEM Electrolysis for Hydrogen production. Principles and Applications*, CRC Press, Boca Raton, USA, 2016.
- [55] A.B. LaConti, L.L. Swette, *Special Applications using PEM Technology*, 2003.
- [56] J.H. Russell, P.J. Chludzinski, D.K. Gupta, G.A. Smarz, J.M. Sedlak, Solid polymer electrolyte water electrolysis technology development for large-scale hydrogen production (design phase). Final report March 1979-December 1980, 1981.
- [57] B. V. Tilak, P. W. T. Lu, J. E. Colman, S. Srinivasan, Solid Polymer Electrolyte (SPE) Water Electrolyzers, in: J. M. Bockris (Ed.), *Comprehensive Treatise of Electrochemistry, Electrochemical Processing*, Plenum Press, New York City, 1981, pp. 61–102.
- [58] C. Copley, T. Norman, A Low Cost High Pressure Hydrogen Generator: DOE Final Report. DEFG36-04GO13029, 2008.
- [59] E.B. Anderson, R.J. Frieland, M.S. Schiller, K.W. Dreier, Large-Scale PEM Electrolysis for Hydrogen Fueling, Essen, Germany, 18 May, 2010.
- [60] K. Ayers, High Performance, Low Cost Hydrogen Generation from Renewable Energy, 2010.
- [61] P. Millet, R. Ngameni, S.A. Grigoriev, N. Mbemba, F. Brisset, A. Ranjbari, C. Etiévant, PEM Water Electrolyzers: From Electrocatalysis to Stack Development, *International Journal of Hydrogen Energy* 35 (2010) 5043–5052.
- [62] H. Butsch, C. Roth, D. Ritzinger, G. Hoogers, A. Bock, Spatially Resolved Contact Pressure and Contact Resistance Measurements at the Gas Diffusion Layer: A Tool for PEM Fuel Cell Development, *J. Electrochem. Soc.* 159 (6) (2012) B709.
- [63] T. Swamy, E.C. Kumbur, M.M. Mench, Investigation of bipolar plate and diffusion media interfacial structure in PEFCs: A fractal geometry approach, *Electrochimica Acta* 56 (8) (2011) 3060–3070.
- [64] Y. Hung, K.M. EL-Khatib, H. Tawfik, Corrosion-resistant lightweight metallic bipolar plates for PEM fuel cells, *J Appl Electrochem* 35 (5) (2005) 445–447.
- [65] A. B. Laconti, A. R. Fragala, J. R. Boyack, Solid polymer electrolyte electrochemical cells - Electrode and other materials considerations, in: *Symposium on Electrode*

- Materials and Processes for Energy Conversion and Storage, Philadelphia, Pa, Electrochemical Society, Inc, Princeton, N.J, 1977, pp. 354–374.
- [66] H.Y. Jung, S.Y. Huang, P. Ganesan, B.N. Popov, Performance of Gold-Coated Titanium Bipolar Plates in Unitized Regenerative Fuel Cell Operation, *Journal of Power Sources* 194 (2009) 972–975.
- [67] H. Ito, Current Collectors (GDLs) and Materials, in: D. Bessarabov, H. Wang, H. Li, N. Zhao (Eds.), *PEM Electrolysis for Hydrogen Production. Principles and Applications*, Taylor & Francis Group, Boca Raton, USA, 2016, pp. 147–155.
- [68] Y. Tanaka, K. Kikuchi, Y. Saihara, Z. Ogumi, Investigation of current feeders for SPE cell, *Electrochimica Acta* 50 (22) (2005) 4344–4349.
- [69] M. Thieme, K.-P. Wieters, F. Bergner, D. Scharnweber, H. Worch, J. Ndop, T.J. Kim, W. Grill, Titanium powder sintering for preparation of a porous functionally graded material destined for orthopaedic implants, *Journal of Materials Science: Materials in Medicine* 12 (3) (2001) 225–231.
- [70] I.-H. Oh, N. Nomura, N. Masahashi, S. Hanada, Mechanical properties of porous titanium compacts prepared by powder sintering, *Scripta Materialia* 49 (12) (2003) 1197–1202.
- [71] S.A. Grigoriev, P. Millet, S.A. Volobuev, V.N. Fateev, Optimization of porous current collectors for PEM water electrolyzers, *International Journal of Hydrogen Energy* 34 (11) (2009) 4968–4973.
- [72] S. Siracusano, V. Baglio, A. Di Blasi, N. Briguglio, A. Stassi, R. Ornelas, E. Trifoni, V. Antonucci, A.S. Aricò, Electrochemical characterization of single cell and short stack PEM electrolyzers based on a nanosized IrO₂ anode electrocatalyst, *International Journal of Hydrogen Energy* 35 (11) (2010) 5558–5568.
- [73] S. Adler, B.T. Henderson, M.A. Wilson, D.M. Taylor, R. Richards, Reference electrode placement and seals in electrochemical oxygen generators, *Solid State Ionics* 134 (1-2) (2000) 35–42.
- [74] W. He, T.V. Nguyen, Edge Effects on Reference Electrode Measurements in PEM Fuel Cells, *Journal of the Electrochemical Society* 151 (2) (2004) A185-A195.
- [75] Z. Liu, J.S. Wainright, W. Wuang, R.F. Savinell, Positioning the Reference Electrode in Proton Exchange membrane fuel cells: calculations of Primary and Secondary Current Distribution, *Electrochimica Acta* 49 (923-935) (2004).
- [76] M. NAGATA, Y. ITOH, H. IWAHARA, Dependence of observed overvoltages on the positioning of the reference electrode on the solid electrolyte, *Solid State Ionics* 67 (3-4) (1994) 215–224.
- [77] Z. Siroma, R. Kakitsubo, N. Fujiwara, T. Ioroi, S.I. Yamazaki, K. Yasuda, Compact Dynamic Hydrogen Electrode Unit as a Reference Electrode for PEMFCs, *Journal of Power Sources* 156 (2006) 284–287.
- [78] K. Petrov, K. Xiao, E.R. Gonzalez, S. Srinivasan, A.J. Appleby, O.J. Murphy, An advanced proton exchange membrane electrolyzer with an improved three dimensional reaction zone, *International Journal of Hydrogen Energy* 18 (11) (1993) 907–913.
- [79] P. Aldebert, F. Novel-Cattin, M. Pineri, P. Millet, C. Doumain, R. Durand, Preparation and Characterization of SPE Composites for Electrolyzers and Fuel Cells, *Solid State Ionics* 35 (3-9) (1989).

- [80] F. Andolfatto, R. Durand, A. Michas, P. Millet, P. Stevens, Solid polymer electrolyte water electrolysis: electrocatalysis and longterm Stability, *International Journal of Hydrogen Energy* 19 (5) (1994) 421–427.
- [81] P. Millet, Water electrolysis using eme technology: electric potential distribution inside a nafion membrane during electrolysis, *Electrochimica Acta* 39 (17) (1994) 2501–2506.
- [82] D. Gerteisen, Realising a reference electrode in a polymer electrolyte fuel cell by laser ablation, *Journal of Applied Electrochemistry* 37 (12) (2007) 1447–1454.
- [83] S. Trasatti, O.A. Petrii, Real surface area measurements in electrochemistry, *Journal of Electroanalytical Chemistry* 327 (1-2) (1992) 353–376.
- [84] R.F. Savinell, Electrochemically Active Surface Area, *J. Electrochem. Soc.* 137 (2) (1990) 489.
- [85] A. Marshall, S. Sunde, M. Tsytkin, R. Tunold, Performance of a PEM Water Electrolysis Cell using IrxRuyTazO2IrxRuyTazO2 Electrocatalysts for the Oxygen Evolution Electrode, *International Journal of Hydrogen Energy* 32 (13) (2007) 2320–2324.
- [86] C. Rozain, E. Mayousse, N. Guillet, P. Millet, Influence of iridium oxide loadings on the performance of PEM water electrolysis cells: Part I–Pure IrO₂-based anodes, *Applied Catalysis B: Environmental* 182 (2016) 153–160.
- [87] E. Rasten, G. Hagen, R. Tunold, Electrocatalysis In Water Electrolysis With Solid Polymer Electrolyte, *Electrochimica Acta* 48 (2003) 3945–3952.
- [88] C. Rozain, E. Mayousse, N. Guillet, P. Millet, Influence of iridium oxide loadings on the performance of PEM water electrolysis cells: Part II – Advanced oxygen electrodes, *Applied Catalysis B: Environmental* 182 (2016) 123–131.
- [89] I. Dedigama, P. Angeli, K. Ayers, J.B. Robinson, P.R. Shearing, D. Tsaoulidis, D. Brett, In situ diagnostic techniques for characterisation of polymer electrolyte membrane water electrolyzers - Flow visualisation and electrochemical impedance spectroscopy, *International Journal of Hydrogen Energy* 39 (2014) 4468–4482.
- [90] T. Ous, C. Arcoumanis, Visualisation of water accumulation in the flow channels of PEMFC under various operating conditions, *Journal of Power Sources* 187 (1) (2009) 182–189.
- [91] Z. Zhan, C. Wang, W. Fu, M. Pan, Visualization of water transport in a transparent PEMFC, *11th China Hydrogen Energy Conference* 37 (1) (2012) 1094–1105.
- [92] K. Tüber, D. Póca, C. Hebling, Visualization of water buildup in the cathode of a transparent PEM fuel cell, *Journal of Power Sources* 124 (2) (2003) 403–414.
- [93] I.S. Hussaini, C.-Y. Wang, Visualization and quantification of cathode channel flooding in PEM fuel cells, *Journal of Power Sources* 187 (2) (2009) 444–451.
- [94] A. Bazylak, Liquid water visualization in PEM fuel cells: A review, *International Journal of Hydrogen Energy* 34 (9) (2009) 3845–3857.
- [95] Y. Tanaka, K. Kikuchi, Y. Saihara, Z. Ogumi, Bubble Visualization and Electrolyte Dependency of Dissolving Hydrogen in Electrolyzed Water Using Solid-Polymer-Electrolyte, *Electrochimica Acta* 50 (2005) 5229–5236.
- [96] I. Dedigama, K. Ayers, P.R. Shearing, D. Brett, An Experimentally Validated Steady State Polymer Electrolyte Membrane Water Electrolyser Model, *International Journal of Electrochemical Science* 9 (2014) 2662–2681.

- [97] O. Selamet, U. Pasaogullari, D. Spornjak, Hussey, D.S., Jacobsen, D.L., M.D. Mat, Two-phase flow in a proton exchange membrane electrolyzer visualized in situ by simultaneous neutron radiography and optical imaging, *International Journal of Hydrogen Energy* 38 (2013) 5823–5835.
- [98] M. Secanell, J. Wishart, P. Dobson, Computational design and optimization of fuel cells and fuel cell systems: A review, *Journal of Power Sources* 196 (8) (2011) 3690–3704.
- [99] C. Siegel, Review of computational heat and mass transfer modeling in polymer-electrolyte-membrane (PEM) fuel cells, *Energy* 33 (9) (2008) 1331–1352.
- [100] A.Z. Weber, J. Newman, Modeling Transport in Polymer-Electrolyte Fuel Cells, *Chem. Rev.* 104 (10) (2004) 4679–4726.
- [101] K.Z. Yao, K. Karan, K.B. McAuley, P. Oosthuizen, B. Peppley, T. Xie, A Review of Mathematical Models for Hydrogen and Direct Methanol Polymer Electrolyte Membrane Fuel Cells, *Fuel Cells* 4 (12) (2004) 3–29.
- [102] S.A. Vilekar, R. Datta, The effect of hydrogen crossover on open-circuit voltage in polymer electrolyte membrane fuel cells, *Journal of Power Sources* 195 (8) (2010) 2241–2247.
- [103] N.S. Rosenthal, S.A. Vilekar, R. Datta, A comprehensive yet comprehensible analytical model for the direct methanol fuel cell, *Journal of Power Sources* 206 (2012) 129–143.
- [104] A. Bergmann, D. Gerteisen, T. Kurz, Modelling of CO Poisoning and its Dynamics in HTPEM Fuel Cells, *Fuel Cells* 10 (2) (2010) 278–287.
- [105] K. Steinkamp, J.O. Schumacher, F. Goldsmith, M. Ohlberger, C. Ziegler, A Nonisothermal PEM Fuel Cell Model Including Two Water Transport Mechanisms in the Membrane, *J. Fuel Cell Sci. Technol.* 5 (1) (2008) 11007.
- [106] K. Onda, T. Murakami, H. Takeshi, M. Kobayashi, R. Notu, K. Ito, Performance Analysis of Polymer Electrolyte Water Electrolysis Cell at a Small Unit Test Cell and Performance Prediction of Large Stacked Cell, *Journal of Electrochemical Society* 149 (2002) 1078.
- [107] P. CHOI, D. Bessarabov, R. Datta, A simple model for solid polymer electrolyte (SPE) water electrolysis, *Solid State Ionics* 175 (2004) 535–539.
- [108] R. García-Valverde, N. Espinosa, A. URBINA, Simple PEM water electrolyser model and experimental validation, *International Journal of Hydrogen Energy* 37 (2) (2012) 1927–1938.
- [109] M. Ni, M. Leung, D. Leung, Electrochemistry Modeling of Proton Exchange Membrane (PEM) Water Electrolysis for Hydrogen Production, in: *Conference Proceedings, Lyon, France, Curran Associates, Inc., 2006, pp. 33–39.*
- [110] B. Laouni, M. Belhamel, W. Naceur, L. Serir, Electrochemical Aided Model to Study Solid Polymer Electrolyte Water Electrolysis, *Revue des Energies Renouvelables* 11 (2) (2008) 267–276.
- [111] M. Shen, N. Bennett, Y. Ding, K. Scott, A concise model for evaluating water electrolysis, *International Journal of Hydrogen Energy* 36 (22) (2011) 14335–14341.
- [112] F. Marangio, M. Santarelli, M. CALI, Theoretical model and experimental analysis of a high pressure PEM water electrolyser for hydrogen production, *International Journal of Hydrogen Energy* 34 (2009) 1143–1158.

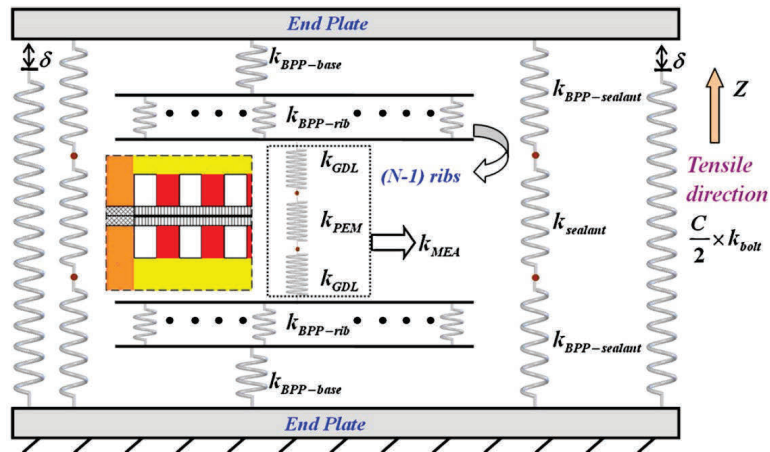
- [113] D.M. Bernardi, A Mathematical Model of the Solid-Polymer-Electrolyte Fuel Cell, *J. Electrochem. Soc.* 139 (9) (1992) 2477.
- [114] L. You, H. Liu, A two-phase flow and transport model for PEM fuel cells, *Journal of Power Sources* 155 (2) (2006) 219–230.
- [115] R.L. LeRoy, C. Bowen, D.J. LeRoy, The Thermodynamics of Aqueous Water Electrolysis, *Journal of Electrochemical Society* (1980).
- [116] B.J. McBride, J. Zehe, S. Gordon, NASA Glenn Coefficients for Calculating Thermodynamic Properties of Individual Species, Cleveland, Ohio, 2002.
- [117] F. Babir, *PEM Fuel Cells: Theory and Practice*, 2nd ed., Elsevier Inc., USA, 2013.
- [118] G. Prentice, *Electrochemical engineering principles*, Prentice Hall, Englewood Cliffs, N.J., Great Britain, 1991.
- [119] C.M.A. Brett, A.M.O. Brett, *Electrochemistry: Principles, methods, and applications /* Christopher M.A. Brett and Ana Maria Oliveira Brett, Oxford University Press, Oxford, 1993.
- [120] T.E. Springer, T.A. Zawodzinski, S. Gottesfeld, Polymer Electrolyte Fuel Cell Model, *Journal of Electrochemical Society* (1991).
- [121] C.T. Choy, *Effective Medium Theory: Principles and Applications*, 1st ed., Oxford University Press, Oxford, 1999.
- [122] M. Chandesris, V. Médeau, N. Guillet, S. Chelghoum, D. Thoby, F. Fouda-Onana, Membrane degradation in PEM water electrolyzer: Numerical modeling and experimental evidence of the influence of temperature and current density, *International Journal of Hydrogen Energy* 40 (3) (2015) 1353–1366.
- [123] Z. Derhoumi, P. Mandin, R. Wuthrich, H. Roustan, Experimental and Numerical Investigations of Two-Phase Electrolysis Processes - Electrical Energy Conversion in Hydrogen Production, *Journal of Applied Fluid Mechanics* 4 (2) (2011) 1735–3645.
- [124] COMSOL Multiphysics, COMSOL Inc., COMSOL Inc., Burlington, MA, USA, 2011.
- [125] R. Makharia, M.F. Mathias, D.R. Baker, Measurement of Catalyst Layer Electrolyte Resistance in PEFCs Using Electrochemical Impedance Spectroscopy, *J. Electrochem. Soc.* 152 (5) (2005) A970.
- [126] R. Datta, D. J. Martino, Y. Dong, P. Choi, Modeling of PEM Water Electrolyzer, in: D. Bessarabov, H. Wang, H. Li, N. Zhao (Eds.), *PEM Electrolysis for Hydrogen Production. Principles and Applications*, Taylor & Francis Group, Boca Raton, USA, 2016, pp. 243–265.
- [127] S.A. Grigoriev, V.I. Poremsky, S.V. Korobtsev, V.N. Fateev, F. Aupretre, P. Millet, High-pressure PEM water electrolysis and corresponding safety issues, *International Journal of Hydrogen Energy* 36 (2011) 2721–2728.
- [128] D. Bessarabov, A. Kruger, S.M. Luopa, J. Park, A.A. Molnar, K.A. Lewinski, Gas Crossover Mitigation in PEM Water Electrolysis: Hydrogen Cross-over Benchmark Study of 3M's Ir-NSTF Based Electrolysis Catalyst-Coated Membranes, *ECS Transactions* 75 (14) (2016) 1165–1173.
- [129] ASTM, Standard Test Method for Pore Size Characteristics of Membrane Filters Using Automated Liquid Porosimeter (Withdrawn 2008), ASTM International, West Conshohocken, PA, 1999.

- [130] T. Reier, M. Oezaslan, P. Strasser, Electrocatalytic Oxygen Evolution Reaction (OER) on Ru, Ir, and Pt Catalysts: A Comparative Study of Nanoparticles and Bulk Materials, *ACS Catal.* 2 (8) (2012) 1765–1772.
- [131] P. Schott, Determination of thermodynamic and electrochemical properties of PEM water electrolysis electrode, within the ANR Project CHAMEAU, 2010.
- [132] A. Awasthi, S. Keith, S. Basu, Dynamic modeling and simulation of a proton exchange membrane electrolyzer for hydrogen production, *International Journal of Hydrogen Energy* 36 (2011) 14779–14786.
- [133] P. Lin, P. Zhou, C.W. Wu, A high efficient assembly technique for large PEMFC stacks, *Journal of Power Sources* 194 (1) (2009) 381–390.
- [134] K.R. Cooper, M. Smith, Electrical test methods for on-line fuel cell ohmic resistance measurement, *Journal of Power Sources* 160 (2006) 1088–1095.
- [135] van der Merwe, Jan, K. Uren, G. van Schoor, D. Bessarabov, Characterisation tools development for PEM electrolyzers, *International Journal of Hydrogen Energy* (26) (2014) 14212–14221.
- [136] R.E. Fuentes, S. Rau, T. Smolinka, J. Weidner, (Invited) Ir-Ru-Ti Metal Oxides and Ir-Ru Metals Supported on TiO₂ Electrocatalysts for PEM Water Electrolysis, *Meet. Abstr. MA2011-02* (18) (2011) 1521.
- [137] H. Ito, T. Maeda, A. Nakano, A. Kato, T. Yoshida, Influence of pore structural properties of current collectors on the performance of proton exchange membrane electrolyzer, *Electrochimica Acta* 100 (2013) 242–248.
- [138] S. Rau, S. Vierrath, J. Ohlmann, A. Fallisch, D. Lackner, F. Dimroth, T. Smolinka, Highly Efficient Solar Hydrogen Generation-An Integrated Concept Joining III-V Solar Cells with PEM Electrolysis Cells, *Energy Technology* 2 (1) (2014) 43–53.
- [139] B. Han, S.M. Steen III, J. Mo, F. Zhang, Electrochemical performance modeling of a proton exchange membrane electrolyzer cell for hydrogen energy, *International Journal of Hydrogen Energy* 40 (22) (2015) 7006–7016.
- [140] K.-H. Oh, J.-H. Chun, K. Banerjee, C. Duvvury, R.W. Dutton, Modeling of temperature dependent contact resistance for analysis of ESD reliability, in: *2003 IEEE International Reliability Physics Symposium: Proceedings 41st annual Dallas, Texas, March 30-April 4, 2003, Dallas, TX, USA, IEEE, Piscataway N.J., 2003*, pp. 249–255.
- [141] K. Banerjee, A. Amerasekera, G. Dixit, C. Hu, Temperature and current effects on small-geometry-contact resistance, in: *International Electron Devices Meeting. IEDM Technical Digest, Washington, DC, USA, IEEE, 1997*, pp. 115–118.
- [142] M. Muñoz Portero, J. García Antón, J. Guiñón Segura, R. Leiva García, Pourbaix diagrams for titanium in concentrated aqueous lithium bromide solutions at 25 °C, *Corrosion Science* 53 (4) (2011) 1440–1450.
- [143] T. Hibiki, M. Ishii, Active nucleation site density in boiling systems 46 (14) (2003) 2587–2601.
- [144] S.A. Grigoriev, M.M. Khaliullin, N.V. Kuleshov, V.N. Fateev, Electrolysis of Water in a System with a Solid Polymer Electrolyte at Elevated Pressure, *Russian Journal of Electrochemistry* 37 (2001) 953–957.
- [145] M. Suermann, T.J. Schmidt, F.N. Büchi, Investigation of Mass Transport Losses in Polymer Electrolyte Electrolysis Cells, *ECS Transactions* 69 (17) (2015) 1141–1148.

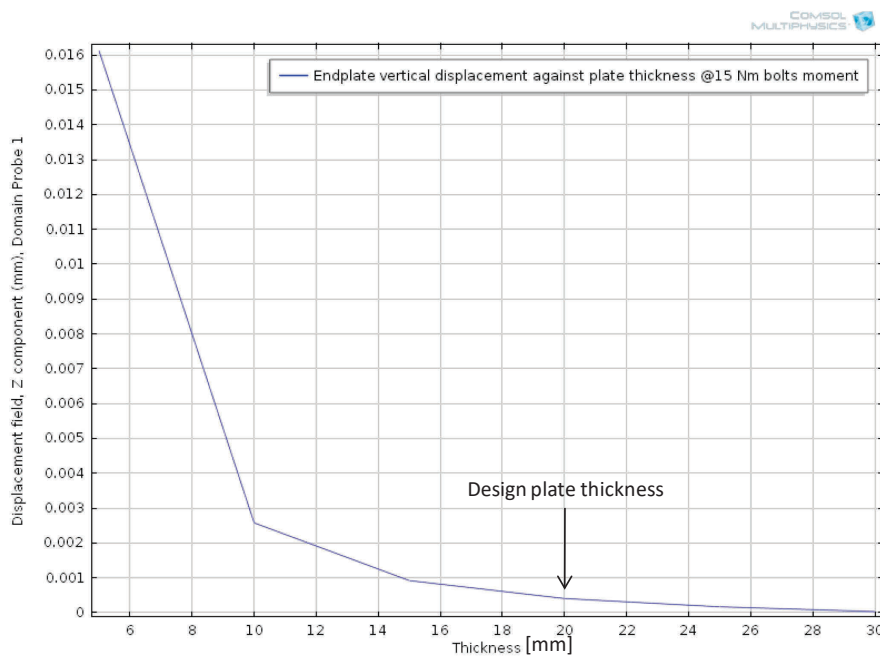
- [146] A. ROY, S. Watson, D. Infield, Comparison of Electrical Energy efficiency of atmospheric and high-pressure electrolysers, *International Journal of Hydrogen Energy* 31 (2006) 1964–1979.
- [147] S.A. Grigoriev, I.G. Shtatniy, P. Millet, V.I. Poremsky, V.N. Fateev, Description and characterization of an electrochemical hydrogen compressor/concentrator based on solid polymer electrolyte technology, *International Journal of Hydrogen Energy* 36 (6) (2011) 4148–4155.
- [148] K. Onda, T. Kyakuno, K. Hattori, K. Ito, Prediction of production power for high-pressure hydrogen by high-pressure water electrolysis, *Journal of Power Sources* 132 (1-2) (2004) 64–70.
- [149] B. Lee, K. Park, H. Kim, Dynamic Simulation of PEM Water Electrolysis and Comparison with Experiments, *International Journal of Electrochemical Science* 8 (2013) 235–248.
- [150] C.M. Hwang, M. Ishida, H. Ito, T. Maeda, A. Nakano, Y. Hasegawa, N. Yokoi, A. Kato, T. Yoshida, Influence of properties of gas diffusion layers on the performance of polymer electrolyte-based unitized reversible fuel cells, *International Journal of Hydrogen Energy* 36 (2011) 1740–1753.
- [151] H. Ito, T. Maeda, A. Nakano, C.M. Hwang, M. Ishida, A. Kato, T. Yoshida, Experimental study on porous current collectors of PEM electrolysers, *International Journal of Hydrogen Energy* 37 (9) (2012) 7418–7428.
- [152] J. Nie, Y. Chen, Numerical modeling of three-dimensional two-phase gas-liquid flow in the flow field plate of a PEM electrolysis cell, *International Journal of Hydrogen Energy* 35 (2010) 3183–3197.
- [153] G.H. Guvelioglu, H.G. Stenger, Computational fluid dynamics modeling of polymer electrolyte membrane fuel cells, *Journal of Power Sources* 147 (1–2) (2005) 95–106.
- [154] A. Kumar, R. G. Reddy, Modeling of Polymer Electrolyte Membrane Fuel Cell With Metal Foam In the Flow-Field of the Bipolar/End Plates, *Journal of Power Sources* 114 (2003) 54–62.
- [155] D. S. Watkins, K. W. Dircks, D. G. Epp Patent 5, 108,849, 1992.
- [156] A.Z. Weber, J. Newman, Chapter Two - Macroscopic Modeling of Polymer-Electrolyte Membranes, in: T.S. Zhao, K.-D. Kreuer and Trung Van Nguyen (Ed.), *Advances in Fuel Cells Advances in Fuel Cell*, Elsevier Science, 2007, pp. 47–117.
- [157] T. Thampan, S. Malhotra, H. Tang, R. Datta, Modeling of Conductive Transport in Proton-Exchange Membranes for Fuel Cells, *J. Electrochem. Soc.* 147 (9) (2000) 3242.
- [158] M. Schalenbach, M. Carmo, D.L. Fritz, J. Mergel, D. Stolten, Pressurized PEM water electrolysis: Efficiency and gas crossover, *International Journal of Hydrogen Energy* 38 (35) (2013) 14921–14933.

Appendices

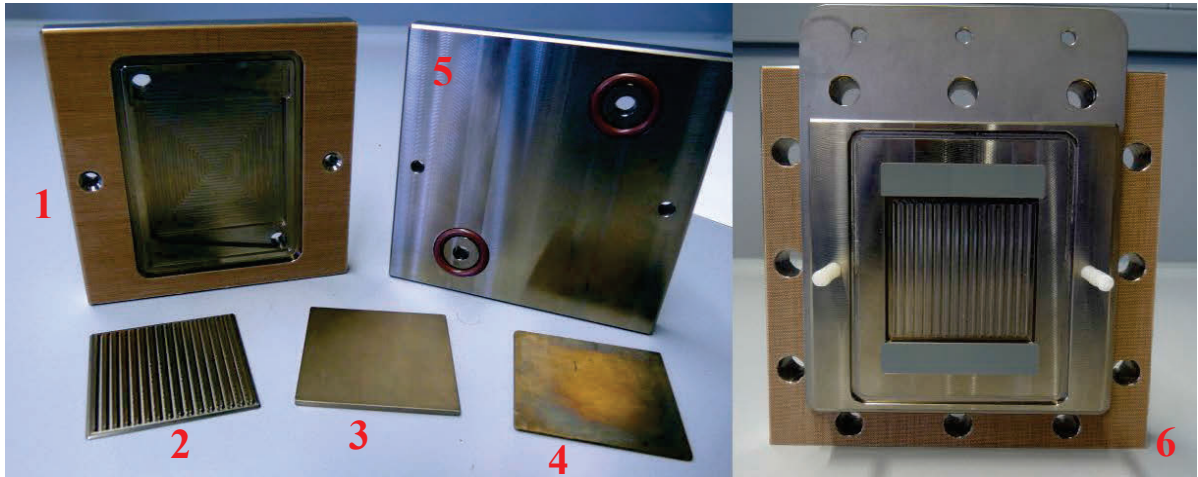
Appendix A: Cell design and components



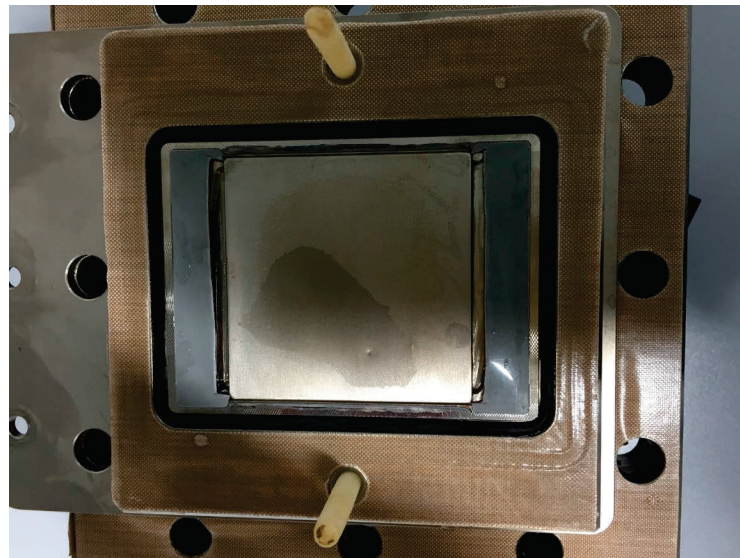
A 1: Equivalent stiffness model, with the cell and stack components as springs connected in series and/or parallel [133]



A 2: Parameter sweep on the pressure plate thickness, showing deformation against plate thickness for the design clamping load. Design thickness of cell endplates was 20 mm

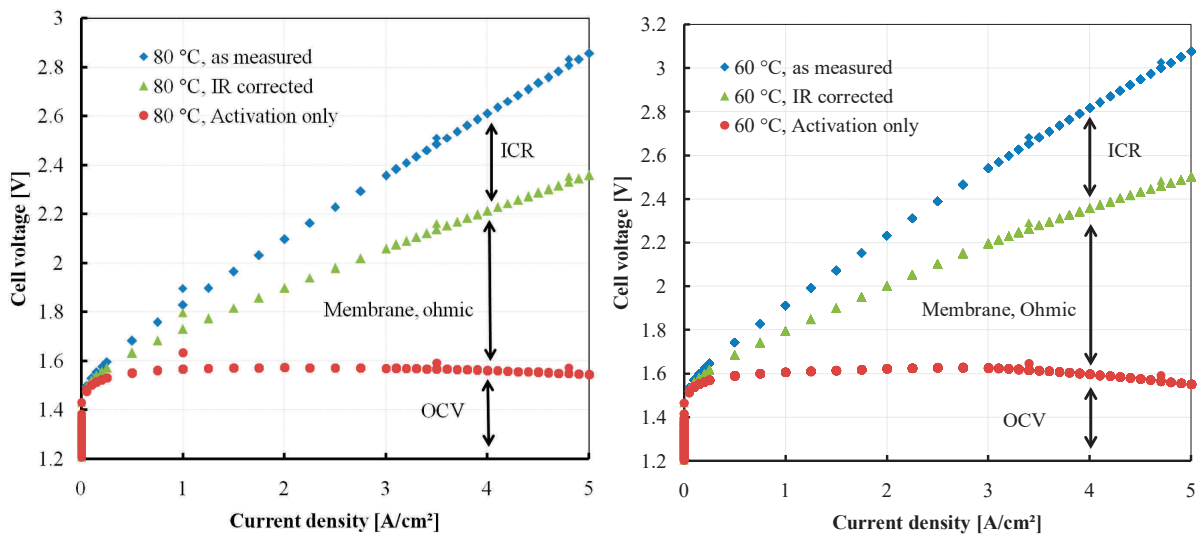


A 3: Cell components: 1) Bipolar plate with pocket for internal cell components 2) Flow field plate 3) Sintered titanium 3-D PTL 4) Titanium space sheet (used) 5) Endplate with O-ring on the manifold 6) Half cell assembly for the conventional design

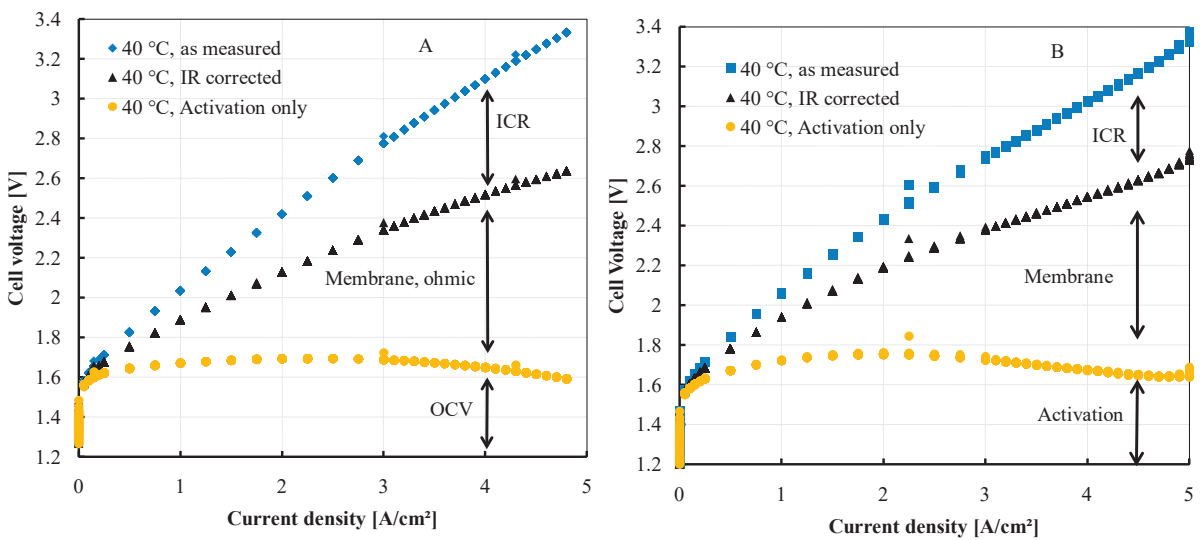


A 4: Assembled half cell of the design without flow channels, showing the sealing concept

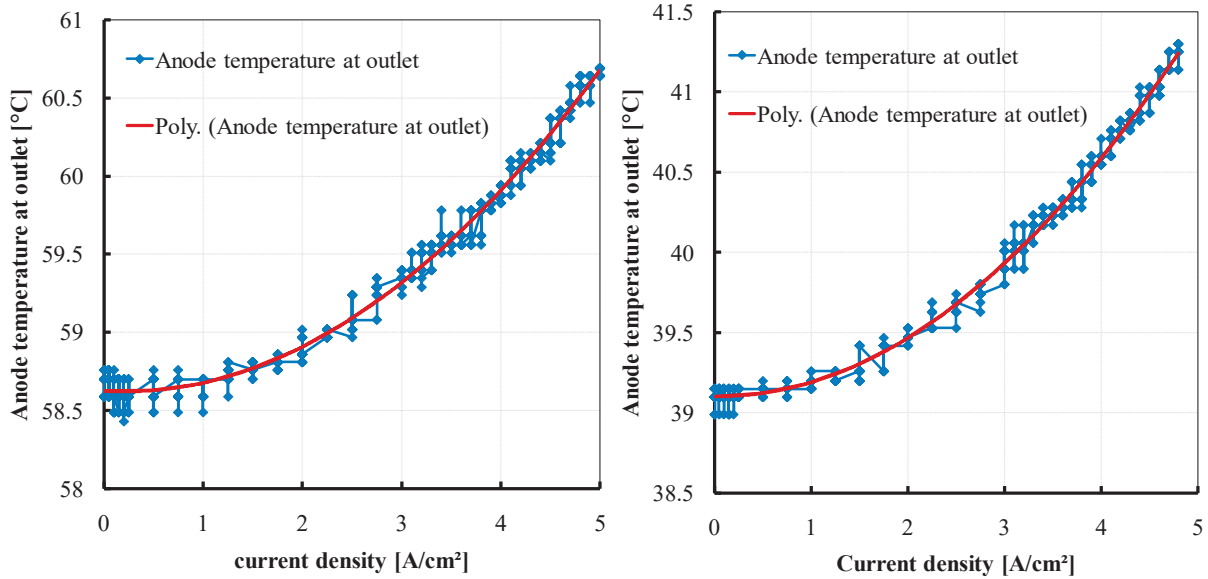
Appendix B: Results and Discussion



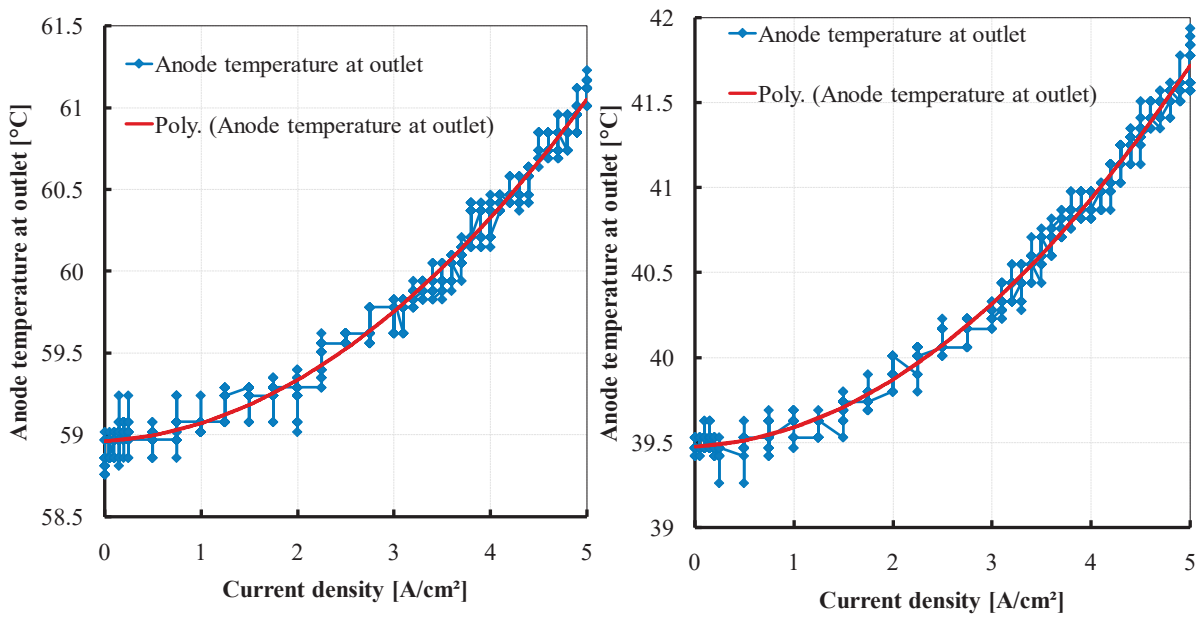
B 1: IR correction of temperature curves for the conventional design at 80 and 60 °C



B 2: IR correction of temperature curves of temperature measurements for A) the conventional design and B) the cell design without flow channels



B 3: Temperature distribution in the conventional design, measured at the anode water outlet at operating flowrate of 0.6 l/min, at 1 bar and operating temperature of 60 °C, left and 40 °C, right.



B 4: Temperature distribution in the design without flow channels, measured at the anode water outlet at operating flowrate of 0.6 l/min, at 1 bar and operating temperature of 60 °C, left and 40 °C, right.

